WL-EMP-IN-143

Interaction Notes

Note 143

September 19, 1972

Some Computational Aspects of Transient Electromagnetics

E. K. Miller

Lawrence Livermore Laboratory

ABSTRACT

Transient electromagnetic computational techniques are critically examined in this paper. In particular, the time-domain magnetic field integral equation applied to surfaces and the time-domain electric field integral equation specialized to thin wires are considered. Except for the natural advantage provided by the time-domain for non-linear analysis, the time and frequency-domains may be viewed as offering alternative and complimentary routes for obtaining and representing electromagnetic phenomena. In general, the time-domain offers a more dependable medium for shortening the calculation time of transient electromagnetic phenomena without loss of significant information. Some representative numerical results and experimental verification are presented. Finally, brief consideration is devoted to various nonintegral equation transient computational techniques.

transient radiation, calculations

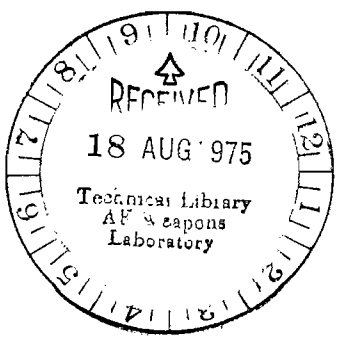

CONTENTS

FOREWORD

This report expands upon the material presented in an invited paper of the same name by C. L. Bennett and the author at the 1972 Spring URSI meeting. Washington, D. C. An attempt has been made to present the state-of-the-art in transient calculations. Because of continued advances which are being made in this area, the material included here can only be considered current through September, 1972. The survey of work in this area is, furthermore, not exhaustive but only representative of the subject matter, with incomplete reference to some special applications such as EMP. Nevertheless, the account of transient electromagnetics given here should provide the reader with the basic developments to date in the area.

I. INTRODUCTION

Determining the transient properties of physical systems has long been a legitimate and worthwhile pursuit in various scientific and engineering studies. A common feature of most transient problems analyzed to date is their susceptibility to description via linear differential equations. This allows treatment of such problems using standard methods like the Laplace transform. Transient circuit analysis is one example of the success of this approach, heat flow problems another.

Transient electromagnetic problems have, by comparison, yielded less readily to classical mathematical treatment. The usual rigorous approach to this subject, until recently, followed standard frequency-domain techniques with a subsequent Fourier transformation to obtain the corresponding time-domain solution. Even this method could not be guaranteed to succeed, until the development of the Fast Fourier Transform (FFT) algorithm and sufficient computing power to make it practicable. Various approximations based on physical optics and employed directly in the time-domain, thus avoiding the Fourier transform, have also been used with some success.

The increased computer capability that has become available in the past few years has opened up new possibilities for the direct time-domain solution of electromagnetic problems. At the same time, advances in short pulse generation and instrumentation technology have promoted interest in the transient behavior of antennas, scatterers and other microwave components. These two developments have had the effect of stimulating further theoretical efforts toward transient electromagnetic analysis.

This report discusses techniques currently being employed for the solution of transient electromagnetic problems. A brief survey of the field and its historical development is included. The principle concern of this presentation, however, is an assessment of integral equation methods which have been developed for studies of transient properties. We will consider formulations applicable to three dimensional structures which can be classified as wires, surfaces, or hydrid geometries. Essential features, capabilities, and limitations of integral equation formulations for the direct

time-domain solution of such geometries will be compared with the corresponding properties of their frequency-domain counterparts. We will in particular be concerned with computer time and storage requirements, accuracies attainable, and the relative flexibility and convenience of use of the time-domain versus frequency-domain approaches. Also to be considered are methods for extending the capabilities of such time-domain techniques to higher frequencies or more complex structures. Typical computed results will be presented to demonstrate the numerical state-of-the-art in direct time-domain methods. It is hoped that this presentation will reach beyond the unique and novel surface features of transient techniques to place their relative position to more conventional methods in proper perspective.

The report is organized into sections which deal with the historical development of transient electromagnetics; integral equation techniques; the comparison of time- and frequency-domain solutions with emphasis on relative computational advantages; and the extension and application of time-domain methods. A summary is contained at the end.

II. SURVEY AND HISTORICAL DEVELOPMENT

Apparently, the first efforts to determine the transient properties of electromagnetic scatterers from time-domain analysis were due to Kennaugh and Cosgriff,[1] who employed a physical optics approximation to calculate the approximate backscatter impulse response of a flat plate and spheroid. Kennaugh and Moffatt[2] have summarized the subsequent work which was devoted to extending the application of physical and geometrical optics to transient response calculations. The alternative approach of Fourier transforming the classical Mie series frequency-domain solution for the sphere to obtain its short pulse response was presented by Rheinstein.[3]

Methods such as these can be extremely useful in estimating the impulse response of various target shapes. They can be, however, severely restricted as to limitations on the body geometry for which they can be successfully used. The physical optics-based approach requires that certain conditions relating to the geometry be satisfied (e.g., the body characteristic dimension R must be large compared with the wavelength). The classical series solutions can be obtained for only the relatively few geometries separable for Maxwell's

Equations. An integral equation approach, on the other hand, offers the possibility of extending direct time-domain solutions to more general, though not necessarily arbitrary, geometries.

Integral equation techniques for frequency-domain application have been extensively developed and applied during recent years, with the earliest work on three-dimensional scatterers being reported in 1965 by Andreason,[4] Oshiro,[5] and Richmond.[6] These techniques have been found useful for a wide variety of radiation and scattering problems, with particular success having been enjoyed by those especially developed for wire geometries. A survey of frequency-domain integral equation methods has been given by Poggio and Miller.[7]

The development of the corresponding integral equation methods for time-domain solutions was first reported in 1968 by Bennett and Weeks,[8] who also summarized previous time-domain work, including related developments in acoustic problems. They obtained the transient response of two-and three-dimensional, perfectly conducting bodies (surface structures) using a time dependent integral equation based upon the magnetic field. An interesting and significant difference between the two methods is that in the time-domain approach the matrix inversion necessary for the frequency-domain solution can be avoided. Instead, a time stepping process allows the complete time-domain solution to be obtained as an initial value problem.

A similar approach for finding the transient response of wire structures was also developed about the same time by Sayre and Harrington.[9] Their technique was based upon the thin-wire approximation to the electric field integral equation. While naturally differing in numerical details from the extended-surface structure solution technique developed by Bennett and Weeks, Sayre and Harrington also obtained transient solutions via an initial value time-stepping procedure, without matrix inversion.

These initial time-domain calculations were performed for relatively simple surface geometries such as the sphere and sphere-capped cylinder and straight and circular wire structures. Subsequent extensions have been incorporated for surface structures by Bennett *et al.*[10] in order to handle bodies with edges and wire appendages, and to exploit plane and rotational symmetry. Miller *et al.*[11] and Poggio *et al.*[12] have presented a more general solution for wire structures, to allow essentially arbitrary temporal and

spatial sampling densities by using quadratic space-time current and charge interpolation. This procedure removes a causality-implied restriction on the time-step interval explicitly included in Bennett's work, while also yielding a smoother current distribution in space-time than that obtainable from the impulse current expansion employed by Sayre.

Other treatments of the time-domain problem which do not involve an integral-equation formulation have also been given. A finite difference solution was worked out by Merewether[13] for determining the transient response of thin bodies of revolution. Merewether used the radiation condition to limit the volume of the linearly expanding region containing the non-zero fields around the structure to that permitted by available computer storage. A time-domain solution for the currents induced on a multiconductor cable in free space [14] or above a ground plane,[15] was given by Bechtold and Kozakoff. Transient calculations based upon Fourier transformed frequency-domain solutions have also been presented by Harrison and King[16] for the infinite cylindrical antenna, by Ormsby and Weiss[17] for the radiation field of linear arrays, by Haynes and Wilkerson[18] for transient-currents on long wires, by Chang and Harrison[19] for the annular slot antenna, by Hodge[20] for scattering from a circular disk, and by Bates and Hawley[21] for current excitation on a long cable located near a dielectric free-space interface.

Although this list is not all inclusive, it may be seen that more effort appears to have been devoted to obtaining transient results from frequency-domain solutions than from a direct time-domain analysis, at least where numerically rigorous, or non-approximate solution methods are employed. In the discussion which follows, we hope to more clearly define the potential advantages of obtaining the transient response from a time-domain viewpoint, as well as for obtaining monochromatic information.

III. INTEGRAL EQUATION TECHNIQUES

The derivation of an integral equation for a given electromagnetic (EM) problem can be accomplished in various ways. What is basically involved, whatever the specific approach, is the expression of Maxwell's Equations in an integral form such that the scattered or radiated (secondary) fields are given as integrals of their sources. By allowing the locus of field observation points to be located where the total field (primary plus secondary) is

known from continuity or boundary conditions, an integral equation can be obtained for the unknown sources in terms of the known primary field distribution.

This procedure holds whether Maxwell's Equations are dealt with in the time-domain or frequency-domain. Furthermore, because of the Fourier transform, it is possible to transform integral equations as well as their numerical solutions from one domain to the other. Thus, we can derive the time-domain solution by beginning with the time-dependent Maxwell Equations. Alternatively, we could first obtain a frequency-domain integral equation whose Fourier transform yields the time-domain equation sought. Or we could follow a combined approach which contains elements of each. We adopt the first course for our discussion here, and refer the reader to Poggio[22] for an example of the second.

The analytical developments which follow are necessarily sketchy. A more detailed account is contained in the references. We begin by presenting the magnetic and electric field integral equations for perfect conductors. These are then applied to surface and wire structures in subsequent sections. A concluding section deals with the numerical analysis. Where appropriate, sample results will be given.

The Magnetic and Electric Field Integral Equations for Perfect Conductors

Maxwell's equations can be written in time-dependent differential form[23] as

$$\nabla \times \overline{H}(\overline{r}, t) = \frac{\partial}{\partial t} \epsilon_0 \overline{E}(\overline{r}, t) + \overline{J}(\overline{r}, t) \tag{1a}$$

$$\nabla \times \overline{E}(\overline{r}, t) = - \frac{\partial}{\partial t} \mu_0 \overline{H}(\overline{r}, t) \tag{1b}$$

$$\nabla \cdot \overline{H}(\overline{r}, t) = 0 \tag{1c}$$

$$\nabla \cdot \overline{E}(\overline{r}, t) = \rho(r, t)/\epsilon_0 \tag{1d}$$

with

$$\nabla \cdot \overline{J}(\overline{r}, t) + \frac{\partial}{\partial t} \rho(\overline{r}, t) = 0 \tag{1e}$$

where μ_0 and ϵ_0 are the permeability and permittivity of free space.

The scalar potential $\phi(\overline{r},t)$ and vector potential $A(\overline{r},t)$, are defined by

$$\overline{H}(\overline{r}, t) = \frac{1}{\mu_0} \nabla \times \overline{A}(\overline{r}, t) \tag{2a}$$

and

$$\overline{E}(\overline{r}, t) = - \nabla \phi(\overline{r}, t) - \frac{\partial}{\partial t} \overline{A}(\overline{r}, t) . \tag{2b}$$

Upon applying the Lorentz gauge condition

$$\nabla \cdot \overline{A}(\overline{r}, t) + \mu_0 \epsilon_0 \frac{\partial}{\partial t} \phi(\overline{r}, t) = 0$$

we obtain for the potentials, the following wave equations:

$$\nabla^2 \overline{A}(\overline{r}, t) - \mu_0 \epsilon_0 \frac{\partial^2}{\partial t^2} \overline{A}(\overline{r}, t) = -\mu_0 \overline{J}(\overline{r}, t) \tag{3a}$$

$$\nabla^2 \phi(\overline{r}, t) - \mu_0 \epsilon_0 \frac{\partial^2}{\partial t^2} \phi(\overline{r}, t) = -\rho(\overline{r}, t)/\epsilon_0 . \tag{3b}$$

But the equations (3a) and (3b) have the Green's function[24]

$$g(\overline{r}, t; \overline{r}', t') = - \frac{1}{4\pi R} \delta(t - R/c, t')$$

where

$$R = |\overline{R}| = |\overline{r} - \overline{r}'|,$$

$$c = 1/\sqrt{\mu_0 \epsilon_0}$$

and $\delta(x,y)$ is the Dirac delta function. Thus

$$\phi(\bar{r}, t) = \frac{1}{4\pi\epsilon_0} \int_V \frac{\rho(\bar{r}', t - R/c)}{R} \, dv' \tag{4a}$$

$$A(\bar{r}, t) = \frac{\mu_0}{4\pi} \int_V \frac{\bar{J}(\bar{r}', t - R/c)}{R} \, dv' \, . \tag{4b}$$

The time-dependent electric and magnetic fields due to $\bar{J}$ and ρ are thus given by

$$\bar{E}(\bar{r},t) = -\frac{1}{4\pi} \left[\frac{1}{\epsilon_0} \int_V \frac{1}{R^2} \nabla R \rho(\bar{r}', \tau) \, dv' \right.$$

$$+ \frac{1}{\epsilon_0} \int_V \frac{1}{R} \nabla R \, \frac{\partial}{\partial \tau} \rho(\bar{r}', \tau) \, dv'$$

$$\left. + \mu_0 \int_V \frac{1}{R} \frac{\partial}{\partial \tau} \bar{J}(\bar{r}', \tau) \, dv' \right] \tag{5}$$

$$\bar{H}(\bar{r}, t) = \frac{1}{4\pi} \int_V \left[\frac{1}{R^2} \bar{J}(\bar{r}', \tau) \right.$$

$$\left. + \frac{1}{Rc} \frac{\partial}{\partial \tau} \bar{J}(\bar{r}, \tau) \right] \frac{\bar{R}}{R} \, dv' \tag{6}$$

with

$$\tau = t - R/c$$

and

$$\frac{\partial}{\partial \tau} f(\tau) \equiv \frac{\partial}{\partial t} f(t) \Big|_{t=\tau} \, .$$

Equations (5) and (6) represent the secondary fields radiated by the volume distributions of current and charge $\bar{J}(\bar{r},t)$ and $\rho(\bar{r},t)$. The problems for which we require such expressions will involve surface current and charge distributions on perfectly conducting bodies. The appropriate equations for this latter case can be obtained from Eqs. (5) and (6) in the usual wasy, to get, with $\bar{K}$ and σ the surface current and charge densities,

$$\overline{E}(\overline{r},t) = -\frac{1}{4\pi}\int_S \left[\frac{1}{\epsilon_0 R}\nabla R\sigma(r',\tau) + \frac{1}{\epsilon_0}\frac{\partial}{\partial\tau}\sigma(r',\tau)\nabla R + \mu_0\frac{\partial}{\partial\tau}\overline{K}(\overline{r}',\tau)\right]\frac{ds'}{R} \quad (7)$$

and

$$\overline{H}(\overline{r},t) = \frac{1}{4\pi}\int_S \left[\frac{\overline{K}(\overline{r}',\tau)}{R} + \frac{1}{c}\frac{\partial}{\partial\tau}\overline{K}(\overline{r},\tau)\right]\times\frac{\overline{R}}{R}\,ds'. \quad (8)$$

The far-field forms of Eqs. (7) and (8) can be obtained from the limit $R \to \infty$, and become

$$\overline{E}(\overline{r},t) = -\frac{1}{4\pi rc}\int_S \left[\sqrt{\frac{\mu_0}{\epsilon_0}}\frac{\partial}{\partial\tau}\overline{K}(\overline{r}',\tau) - \frac{\overline{r}}{\epsilon_0 r}\frac{\partial}{\partial\tau}\sigma(\overline{r}',\tau)\right]ds'$$

$$\overline{H}(\overline{r},t) = \frac{1}{4\pi cr}\int_S \frac{\partial}{\partial\tau}\overline{K}(\overline{r}',\tau)\times\frac{\overline{r}}{r}\,ds'$$

Now the frequency-domain radar cross section can be defined as

$$\frac{\sigma}{\lambda^2} = \frac{\omega^2}{\pi c^2}\frac{|\overline{E}(\omega)|^2}{|\overline{E}^{inc}(\omega)|^2} = \frac{\omega^2}{\pi c^2}\frac{|\overline{H}(\omega)|^2}{|\overline{H}^{inc}(\omega)|^2},$$

with the dependence of σ/λ^2 on the incidence angle, observation angle, and polarization all suppressed. It is computed from the quotient of the spectra of the radiated field and the incident field. These in turn are determined by taking the Fourier transforms of the radiated field and the incident field.

The sought-for integral equations are finally derivable from Eqs. (7) and (8) by allowing $\bar{r} \to S$ and introducing the primary or incident field while imposing the boundary conditions.

$$\hat{n} \times \bar{E}^{\text{total}} = 0 = \hat{n} \times (\bar{E} + \bar{E}^{\text{inc}})$$

$$\hat{n} \cdot \bar{H}^{\text{total}} = 0 = \hat{n} \cdot (\bar{H} + \bar{H}^{\text{inc}})$$

applicable at the surface of a perfect conductor, to obtain

$$\hat{n} \times \bar{E}^{\text{inc}} = \frac{\hat{n}}{2\pi} \times \oint_S \left[\frac{\mu_0}{R} \frac{\partial}{\partial \tau} \bar{K}(r', \tau) - \frac{\sigma(r', \tau)}{\epsilon_0} \frac{\bar{R}}{R^3} - \frac{\partial}{\partial \tau} \sigma(r', \tau) \frac{1}{\epsilon_0} \frac{\bar{R}}{cR^2} \right] ds', \tag{9}$$

$$\bar{K}(\bar{r}, t) = 2\hat{n} \times \bar{H}^{\text{inc}}(\bar{r}, t) + \frac{1}{2\pi} \hat{n} \times \oint_S \left[\frac{1}{c} \frac{\partial}{\partial \tau} \bar{K}(\bar{r}', \tau) + \bar{K}(\bar{r}', \tau) \frac{1}{R} \right] \times \frac{\bar{R}}{R^2} ds' \tag{10}$$

where $\oint_S$ denotes a principle value integral about R = 0 defined by

$$\oint_S = \lim_{\Delta S \to 0} \int_{S - \Delta S}$$

Details of treating integrable singularities of the type found in Eqs. (9) and (10) are given by Kellog[25] and may be found for this specific problem in Refs. 7 and 8.

It is worthwhile to also present the frequency-domain versions of Egs. (9) and (10). They are

$$\hat{n} \times \bar{E}^{inc}(\bar{r}) = \frac{1}{2\pi i\omega\epsilon_0}\hat{n} \times \int_S \left\{-\omega^2\mu_0\epsilon_0\bar{K}(r')\phi + [\nabla' \cdot \bar{K}(\bar{r}')]\nabla'\phi\right\} ds', \tag{11}$$

and

$$\bar{K}(\bar{r}) = \frac{1}{2\pi}\hat{n} \times \int_S \bar{K}(\bar{r}') \times \nabla'\phi \, ds' + 2\hat{n} \times \bar{H}^{inc}(\bar{r}) \tag{12}$$

with

$$\phi = \exp(-ikR)/R$$

and

$$k = \omega\sqrt{\mu_0\epsilon_0}.$$

Equations (11) and (12) can be derived from a Fourier transform of their respective time-domain versions, as discussed by Poggio and Miller,[7] or directly in the frequency domain as presented by Andreason,[4] O'Shiro,[5] and others.

A numerical solution of Eqs. (9) and (10) can be formally developed using techniques similar to those already found successful for frequency-domain application. This involves approximating the unknown surface current in terms of some suitable basis function expansion, and then satisfying the integral equation in some prescribed fashion by using an appropriate set of weight functions as a function of space and time. For surface structure analysis this might be accomplished, for example, by dividing the surface into patches or segments of small enough size relative to the shortest wavelength of interest so that the current on each can be regarded as a constant. The integral equation could be "point-matched" at the center of each patch by using delta function weights. This would result in an

overall process known as subsectional collocation and would yield a linear system of equations for the unknown. Since the time-domain formulation further involves the time dependence of the fields and sources, the solution process must also include time as an additional variable. This might be accommodated by dividing time into increments small enough, relative to the highest frequency of interest, that the various quantities could be regarded as constants over each time increment. A histogram or pulse-like current approximation in space-time would then result.

While the time- and frequency-domain solutions are achieved using similar concepts for approximating the functional behavior of the fields and sources involved, they differ greatly in the actual process of obtaining numerical results. The frequency-domain current solution is commonly obtained via matrix inversion (iteration can also be used) and is consequently source independent, but valid only at the freqency for which the inverse or admittance matrix has been calculated. In the time-domain on the other hand, due to the retarded time relation between the current and its propagating field, the current may be found as the solution to an initial value problem. While not requiring matrix inversion, or being restricted to only a single frequency, it is, however, source dependent. These observations indicate the underlying and fundamental differences which characterize the two formulations.

The derivation of Eqs. (9) and (10) is useful for illustrative purposes. In actual application only Eq. (10) is used as it is shown, it being applied to the analysis of three dimensional surface structures. Various special forms of these equations are found to be better suited for the treatment of wires, infinite cylinders, or hybrid structures. The applicable equations for these special cases will be presented in the following sections together with sample numerical results obtained from their solution, as well as from the solution of Eq. (10). Brief descriptions of the solution procedure will also be included as appropriate, but a detailed account of the numerical methods will be deferred to the concluding section of this chapter.

Analysis of Surface Structures

The two integral equations developed above are suitable for the time-domain analysis of perfectly conducting bodies. While in principle

either one might be used for a given problem, experience gained from frequency-domain applications indicates that the electric-field integral equation (EFIE), Eq. (9), is more suitable for the treatment of wire-type structures, and the magnetic-field integral equation (MFIE), Eq. (10), is more appropriate for handling extended surface objects. The reasons for this are twofold: 1) the EFIE contains a higher order singularity which numerically, at least, is more amenable to handling via the thin-wire approximation than for surface geometries, and 2) the MFIE contains a $\bar{K} \times \nabla R$ term, which is not as numerically tractable for application to wire structures as it is to surface geometries. Examples to the contrary can be found. Lin and Mei[26] used the MFIE for wire antenna analysis and Harrington and Mautz[27] applied the EFIE to bodies of revolution. These examples are more the exception than the general rule.

Application of the magnetic field integral equation to two-dimensional and three-dimensional surface structures is considered below.

a. Two-Dimensional Surface Structures

An integral equation for structures having only a two-dimensional variation and extending to infinity in the third (z) direction can be formally obtained from Eqs. (9) and (10). It may be simpler however, to follow Bennett and Weeks,[8] who derive the two-dimensional vector potential for the normal incidence case as

$$\bar{A}(\bar{\rho}, t) = \frac{1}{4\pi\mu_0} \int dc' \int d\tau \bar{J}(\rho', \tau)$$

$$\times \int_{-\infty}^{\infty} dz' \frac{\delta(t - R/c, \tau)}{R}$$

for a z-directed cylinder. Upon integration over z', there results

$$\bar{A}(\bar{\rho}, t) = \frac{c}{2\pi\mu_0} \int_S ds' \int_{-\infty}^{t-P/c}$$

$$\times \frac{\bar{K}(\bar{\rho}', \tau)}{\sqrt{c^2(t - \tau)^2 - P^2}} d\tau,$$

where $P = \rho - \rho'$ and S is the structural contour.

After evaluating $\nabla \times \overline{A}$ and decomposing the magnetic field into the usual transverse electric (TE) and transverse magnetic (TM) components, the following integral equation is obtained:

$$\hat{n} \times \overline{H}(\rho, t) = 2\hat{n} \times \overline{H}^{inc}(\rho, t) + \frac{c}{\pi} \hat{n} \times \int_S ds' (\hat{n} \cdot \hat{n}') \int_{\tau=-\infty}^{t-P/c} \frac{d\tau}{\sqrt{c^2(t-\tau)^2 - P^2}} \cdot \left[\frac{\overline{H}(\rho', \tau)}{c(t-\tau) + P} + \frac{1}{c} \frac{\partial}{\partial \tau} \overline{H}(\rho', \tau) \right]. \quad (13)$$

This equation results because of the orthogonality of the TE and TM fields. It can be written as two independent equations for the longitudinal (H_z or TE) and azimuthal (H_ϕ or TM) fields respectively. The corresponding far-field expression for the scattered field can be written as

$$\overline{H}(\rho, t) = \frac{1}{2\pi\sqrt{2\rho}} \left[\hat{z} \int_S ds' (\hat{n}' \cdot \hat{\rho}) \times \int_{-\infty}^{t-P/c} \frac{d\tau}{\sqrt{c(t-\tau) - P}} \frac{\partial}{\partial \tau} H_z(\rho', \tau) + \hat{\phi} \int_{S'} ds' \int_{-\infty}^{t-p/c} \frac{d\tau}{\sqrt{c(t-\tau) - P}} \frac{\partial}{\partial \tau} H_\phi(\rho', \tau) \right].$$

Bennett and Weeks[8,28] have evidently obtained the only time-domain results to date for the cylindrical geometry. Some typical examples of their calculations follow below.

Results pertaining to scattering from a cylinder of 1 m radius (a) are shown in Figs. 1-6. A Gaussian pulse of the form $H^{inc} \propto \exp[-A^2(t - x/c)^2]$ having a width of approximately the cylinder diameter was used for the normal incidence field. Sample points spaced at 15 deg intervals were used for the current and field match points on the cylinder. A time increment of $c\Delta t = 0.1$ light meter was initially used, and subsequently increased

to 0.2 light meter after the incident field had passed the scatterer.

A comparison of the time-dependent backscatter from the cylinder for the TE and TM components computed from the time dependent integral equation is shown in Figs. 1 and 2. The Fourier transformed frequency-domain solution and the physical optics approximation are also shown. The corresponding bistatic scattering patterns for the two polarizations are shown in Figs. 3 and 4, where the incident and scattered pulses, shown to scale in space, may be viewed as snapshots of the pulses in space, at a given time. The semi-circle represents the locus of points in space to which the peak of the incident pulse would have propagated had it reflected from the coordinate system origin. Clear evidence for the creeping wave return is provided by the second positive pulse in the late-time TE backscatter waveform, but is lacking in the TM return, suggesting that the latter will exhibit no periodicity in its frequency response. This conclusion is confirmed by results shown in Figs. 5 and 6, where the frequency responses calculated from the time-domain backscattered fields are compared with the classical frequency-domain solutions. The upper frequency cut off in the time-domain results occurs primarily because of the spatial sampling limitation on the smallest resolvable wavelength and is discussed further below.

A second shape considered by Bennett and Weeks[8,28] is a strip 3 m long capped by 1-m-radius (a) hemi-cylinders. A total of 48 equally spaced points approximately 0.25 m apart were used for the space samples, while the incident field and time increments were identical to those employed for the circular cylinder. Both broadside and end-on incidence of the TM and TE fields was considered; results for both cases are shown in the time-domain in Figs. 7 through 10 and in the frequency-domain in Figs. 11 and 12. As expected, the initial end-on backscatter returns closely resemble those already obtained for the circular cylinder. The differentiating effects of the edges are exhibited in the backscatter return for both polarizations. The frequency response obtained for broadside incidence (Fig. 11) is seen to increase in a nearly monotonic fashion with increasing frequency, an expected result, while the end-on incidence backscatter curves approach a constant value

identical to that of the circular cylinder with increasing frequency. The latter is reasonable, since the side return and creeping wave effect diminish in importance as the wavelength decreases.

The final shape treated by Bennett and Weeks consists of a corner reflector, the geometry of which is illustrated in Fig. 13. Calculations were performed for both polarizations and for plane-wave incidence on both the concave and convex surfaces of the reflector, as shown in Figs. 14 through 17. The time-domain waveforms of the scattered fields are seen to be much more complex than for the two geometries thus far examined. This is evidently due to multiple scattering effects. Of particular interest is the reciprocity of the forward scattered fields (Figs. 14 and 15; 16 and 17), a necessary (though not sufficient) condition for solution validity. As expected, the frequency-domain backscatter responses as plotted in Figs. 18 and 19 are more oscillatory than were the corresponding curves for the two previous geometries. The concave incidence backscatter curves reveal the TE and TM frequency responses to be out of phase. Bennett and Weeks explain this by noting that the time-domain returns from the interior corner are of opposite signs for the TE and TM cases, but of the same sign for the edge return. The convex backscatter is seen to be initally quite oscillatory, but to approach a more-or-less constant level with increasing frequency due to the circular geometry of the exterior corner.

The results above are representative of what can be accomplished with the two-dimensional time-domain integral equation. A considerable degree of physical insight, which in many respects is not as readily obainable from the more common frequency-domain representation, can be gained from the time-domain waveforms. The time-domain consequently provides an alternative and complementary viewpoint from which to study electro-magnetic scattering. Although the two-dimensional analysis above is obviously limited in application, it possesses a degree of efficiency not attainable in three dimensions, and so may be useful for obtaining, in a limited way, an underlying understanding of some three-dimensional problems (i.e., multiple scattering effects or the behavior of bodies large in one dimension).

b. Three-Dimensional Surface Structures

It was mentioned above that although either the EFIE or MFIE could be employed for surface-structure analysis, the latter is more attractive from a numerical viewpoint. Bennett and Weeks,[8] employing the MFIE given by Eq. (10), have developed the only three dimensional time-domain analysis of surface structures. Some results obtained from their numerical method are given below.

It is convenient to begin the three-dimensional numerical study with the sphere, since rigorous results are readily available to serve as a check on the time-domain derived data. This was done with the circular cylinder in the two-dimensional case. A sphere 1 m in radius (a) was subjected to a field of approximately the sphere's diameter incident along the positive z-axis of a coordinate system centered in the sphere, $\left(\text{i.e., } H^{inc} \propto \exp[-A^2(t - z/c)^2]\right)$. The surface sample points were selected to maintain a nearly uniform separation between them of approximately 0.25 m. This was accomplished by dividing the sphere into 12 bands of 15 deg width in elevation angle, and spacing the azimuth samples within each band in multiples of 4 to obtain quadrant symmetry. A sequence of 4, 8, 12, 16, 20, 24, 24, 20, 16, 12, 8, 4 patches per band was obtained for a total of 168. A constant time increment of 0.2 light meters was employed throughout the calculation.

The approximate impulse response of the sphere in the backscatter direction is shown in Fig. 20, where the classical Fourier transformed frequency-domain results are also presented for comparison. Transient bistatic E- and H-plane scattering patterns (using the same format as for the cylindrical case) are presented as Figs. 21 and 22, with the time-domain derived frequency response shown in Fig. 23. The sphere exhibits the expected creeping wave response in the backscatter direction in the time response (Figs. 21 and 22), and may be seen to agree well with the frequency-domain data of Fig. 23 up to a ka value of approximately 2π. At this point, the surface sample points are approximately $(2\pi/24)\lambda \sim \lambda/4$ apart, a number previously established as the maximum patch size for which frequency-domain results can be expected to be valid. Further verification of the time-domain calcu-

lation is provided in Figs. 24 and 25, where the bistatic scattering pattern of the sphere is compared with the corresponding frequency-domain result for the two cases ka = 1.1 and 2.9.

A more interesting case to consider is the bistatic approximate E- and H-plane impulse response of a sphere-capped cylinder (Figs. 26 and 27 respectively), for axial incidence. This structure, 1 m in diam and 3 m in overall length (L), was sampled every 30 deg in azimuth and every 0.25 m along the cylindrical axis of the cylinder proper. In addition, there were three 30-deg-wide bands on each end having 4, 8 and 12 samples in azimuth proceeding from the sphere tip towards the cylindrical section, making a total of 144 patches in all. Strong evidence for the creeping wave return is again demonstrated by the second pulse in the backscatter waveform, although little back-scatter evidently occurs from the cylinder sides. The widely separated backscatter returns due to the direct-scatter and creeping wave mechanisms produce the expected oscillatory frequency response seen in Fig. 28. A comparison of the calculated frequency response with experimental results obtained on a rail-line scattering range[29;30] shows good agreement (Fig. 29).

An interesting example of applying the time-domain surface structure analysis to a radiation problem is demonstrated by the results of Figs. 30 through 32. The sphere-capped cylinder just considered from a scattering viewpoint can be treated as an antenna. In this case the incident field is a Gaussian pulse of azimuthally directed magnetic field applied across the center two bands of the cylinder. The bistatic time response is shown in Fig. 30, where because of the azimuthally uniform excitation there is no axially radiated field. A plot of the frequency response in the broadside direction is shown in Fig. 31. The radiation patterns of the sphere-capped cylinder are shown for several values of L/λ in Fig. 32, and seem compatible with well known properties of linear dipole antennas.

As a last example for simple surface structures, we present some time-domain scattering results for a 15-deg half-angle cone-sphere (Figs. 33-38). The segmentation of this structure was also quadrature symmetric following the guidelines previously mentioned, i.e., ~ 0.25 m

separation of the sample points along the surface and a time increment of 0.2 light meters. Note, however, that the samples nearest the tip result in $c\Delta t > \Delta R$ and can produce an unstable solution which diverges with increasing time. When the interaction of such samples was omitted from the calculation, however, a stable, apparently valid, solution was obtained as demonstrated by the computed results. The tip-end and sphere-end incidence E- and H-plane scattering patterns are shown in Figs. 33 and 34, while Fig. 35 depicts the E-plane scattering pattern for broadside incidence. Note the reciprocity checks provided by the 90-deg and 270-deg waveforms of Fig. 35 with the 90-deg E-plane patterns of Figs. 33 and 34. Good agreement of the tip-end incidence Fourier-transformed time-domain data with experimental results is shown in Fig. 36. A final check of the time-domain results is presented in Fig. 37, where the bistatic scattering patterns for several values of (sphere) ka are found to compare well with independent results obtained from a frequency-domain solution.

A different data format is illustrated in Fig. 38 where the H-plane surface current-density on the cone sphere is shown at successive instants of time (illustrated by the relative positions of the incidence pulse) for tip-end incidence of the exciting pulse. The propagation of the surface current pulse from the tip to the sphere-end of the cone-sphere is clearly demonstrated. Such information can be particularly illuminating as to the physical basis of the scattering process.

The treatment of more complex surface structure geometries is illustrated in Figs. 39 through 44. These graphs show the computed bistatic scattering patterns of three satellite models; the advanced defense communications (ADC) (Fig. 39), the university explorer (UES) (Fig. 41), and the gravity gradient test number 2 (GGTS-2) (Fig. 43). Comparison of the backscatter waveform with experimental data is shown in Figs. 40, 42 and 44.

All of these results are due to Bennett et al.,[10] who developed a surface structure time-domain program which exploits rotational symmetry to reduce computer time and storage. The surface distribution of unknown current is thus reduced to a linear variation of current along a line on the surface parallel to the body axis.

The computed backscatter waveforms are seen to agree quite well with the measured results. This agreement serves not only as a corroboration of the numerical solution, but indicates the accuracy of the unique short pulse measurement capability provided by the experimental transient range.[31]

Wire and Hybrid Structures

Wire structures, i.e., objects whose geometrical cross sections are small in comparison to both the shortest wavelength of interest and their own physical length, are most conveniently analyzed using the thin-wire approximation to the EFIE. However, when the structure has the characteristics of both the wire and surface geometries, a hybrid integral equation which incorporates both the EFIE or MFIE may be found most efficient from a numerical viewpoint. These problems are considered in turn in the following sections.

a. Wire Structure Analysis

When the conditions necessary for application of the thin-wire approximation are satisfied, Eq. (9) can be reduced to

$$\hat{s} \cdot \bar{E}^{inc}(\bar{r}, t) = \frac{\mu_0}{4\pi} \int_C \left[\frac{\hat{s} \cdot \hat{s}'}{R} \frac{\partial}{\partial \tau} I(s', \tau) + c \frac{\hat{s} \cdot \bar{R}}{R^2} \frac{\partial}{\partial s'} I(s', \tau) - c^2 \frac{\hat{s} \cdot \bar{R}}{R^3} q(s', \tau) \right] ds' ; \ \bar{r} \epsilon C + a \qquad (14)$$

where

$$q(s', \tau) = - \int_{-\infty}^{\tau} \frac{\partial}{\partial s'} I(s', t') \, dt',$$

$\hat{s}, \hat{s}'$ are the tangent vectors to the wire at $\bar{r}$ and $\bar{r}'$ respectively, C is the wire contour, a is the wire radius, and $(\bar{r} \epsilon C + a)$ denotes that the field is to be evaluated on the wire surface. The corre-

sponding far-field expression similarly reduces to

$$\overline{E}(\overline{r}, t) = -\frac{\mu_0}{4\pi R} \int_C \left[\hat{s}' \frac{\partial}{\partial \tau} I(s', \tau) + \frac{\overline{R}}{R} \frac{\partial}{\partial s'} I(s', \tau) \right] ds'. \qquad (15)$$

A numerical solution of Eq. (14) can be attempted using essentially the same approach as that already discussed for the surface MFIE. However, it is numerically expedient to incorporate a quadratic space-time current and charge interpolation for much the same reason that spatial current interpolation has been found to improve the solution accuracy of the frequency-domain thin-wire EFIE. Interpolation provides a significant reduction in the number of current samples required for a given accuracy in the frequency-domain solution of the EFIE. This is because of the higher order spatial derivative, relative to that associated with the surface MFIE, contained in its kernel. This also appears to apply to the time-domain case. In addition, time interpolation allows more flexibility as to the space and time sample intervals which can be used for a given problem. A detailed discussion of the numerical solution used for Eq. (14) is provided in a subsequent section (page 37). Here we confine ourselves to presenting some sample results obtained for various thin-wire structures.

b. Antenna Structures

The first antenna to be discussed is the center-fed linear dipole. The length of this antenna (L) is 1 m, and its radius-to-length ratio is 0.00674 (i.e., $\Omega \equiv 2 \ln L/a = 150$). The temporal behavior of the source voltage impressed over a region $\Delta = L/11$ around the center of the antenna, in volts, is

$$V_s(t) = \exp\left[-A^2(t - t_{max})^2\right],$$

with $A = 1.5 \times 10^9$ sec^{-1} and $t_{max} = 1.43 \times 10^{-9}$ sec. The impressed electric field, in V/m, is then

$$|E^A(t)| = V_s(t)/\Delta = (11/L) \times \exp\left[-A^2(t - t_{max})^2\right].$$

The antenna is subdivided into 22 spatial segments, the center two of which serve as the source region. The temporal step size (Δt) is set equal to $\Delta z/c = L/22c$, with Δz the spatial segment length. In this case, $\Delta t = 1.515 \times 10^{-10}$ sec. Because the Gaussian pulse has infinite support in the time domain, the starting point ($t = 0$) is defined, for practical reasons, at some reasonable level not equal to zero. Hence, $t = 0$ is generally chosen to correspond to the point on the leading edge of the Gaussian pulse which is 1% of its maximum value.

Figure 45 typifies the results obtained from the calculation. In the upper part of the figure, the source current is plotted against normalized time and the horizontal axis is subdivided into length units normalized to the propagation velocity in free space. If one were to superimpose the input Gaussian pulse, the voltage and current would be seen to behave identically up to the first peak ($L/c - 0.5$). Thereafter, the source current decays more rapidly than the input pulse. This behavior in the region $0.5 \leq L/c \leq 1.0$ can only be explained by electromagnetic coupling between the source region and other portions of the structure. It cannot be due to the reflected current pulse because the transit time from source to end and return is approximately L/c sec.

The second major peak ($L/c \approx 1.5$) represents the arrival of the peak of the reflected current pulse at the source. Subsequent peaks occur at approximately odd integer multiples of $L/2c$. The slight discrepancies in current variation from these integer multiples can be attributed to the fact that the propagation velocity on the structure is somewhat less than that of free space.

The bottom part of Fig. 45 presents the input conductance and susceptance G_0 and B_0 vs the normalized length (L/λ), computed from the ratio of Fourier transforms of the source current and source voltage. For comparison, values from the King-Middleton theory[32] are

included. The frequency-domain results are taken from time-domain data by use of the FFT. The data records for that operation have involved 512 time steps, of which 240 have been taken from the calculated time history. The balance has come from extrapolation of the results.[12] Since the time-domain data usually have indicated a late time ringing at a single frequency with exponential damping, the technique has been to use the late samples in the calculated records to determine λ and ω in $e^{-\lambda t} \sin \omega t$. This has then allowed completion of the record. In all cases λ has been large enough for the record to include sufficient samples for late times (essentially equal to zero) to minimize the aliasing problems in the Fourier transform. The discrepancy between the transformed and King-Middleton results for $L/\lambda > 3.5$ was evident and is not included in the figures but is consistent with the six samples/λ criterion[33] developed in the frequency domain.

Figure 46 is a computed time history of the antenna current over half the symmetrical, center-fed structure. It is not the current for the case shown in Fig. 45, but rather that for an identical dipole excited by a pulse with a spread half that shown in Fig. 45. This history is included for illustrative purposes. The dark horizontal lines represent the extent of the antenna, while the numbers identify the instant of time for which the current is plotted. Each integer refers to a multiple of $\Delta t = 0.152 \times 10^{-9}$ sec so that $L/c = 3.33 \times 10^{-9}$ sec $\approx 22\Delta t$. The pulse's progression along the structure is followed from the time of its first appearance at the source through its first reflection at the end and subsequent second appearance at the source. It is from data like these, which are a direct result of the solution of the integral equation in space-time, that plots of the type shown in the upper half of Fig. 45 derived.

Figure 47 plots the broadside radiated field for the center-fed linear dipole. The temporal response, from the computed time history of the current is shown in the upper half; the frequency-domain response is shown in the lower half. The time scale in units of dipole length divided by the free-space velocity starts at $L/c = 0$, which is the instant the radiated field arrives at the observation point. The radiated field is caused by the temporal derivative of the antenna

current, as one would expect from inspection of Eq. (15). The predominant radiation comes from the source region (when the pulse first appears) and from the ensuing reflections which take place at the antenna ends.

We will discuss this phenomenon in more detail when we consider off-broadside radiation (i.e., in directions other than along a line perpendicular to the wire). At this point, it is sufficient to point out that the field prior to arrival of the radiation due to end reflection is proportional to the negative of the source-region current.

In the bottom half of Fig. 47, the Fourier transform of the broadside radiated field is used for comparison with independently calculated results. The independent results in this particular case were obained by a collocation solution of the thin-wire electric field integral equation at the indicated frequencies.

Figure 48 is a temporal display of the radiated field at an angle 40 deg from broadside. It is included to illustrate the effective active regions of the antenna and to point up the influence of this rather simple radiating system on the radiation of a Gaussian pulse. These data are not unlike the results presented earlier for radiation from a sphere-capped cylinder (Figs. 30-32). The effect of the thicker cylinder has been to considerably reduce its "Q" compared with that of the wire.

As previously mentioned, the radiated field is a result of the temporal variation of the antenna current and is computed by a spatial integration over retarded values of the temporal-current derivative. If we envision the antenna current distribution to be a traveling wave with a Gaussian shape like that in Fig. 46 then the required time derivative is obtained from the Gaussian which, in the limit of narrow spread, becomes a doublet (the derivative of the Dirac delta function). Although for the case shown the Gaussian derivative is not very narrow relative to the antenna length, the use of the doublet representation points out the salient features of the phenomenon.

Figure 49 is included to illustrate further the effects seen in Fig. 48. As the wave first appears on the structure $t = 0+$, it

causes the radiation seen at early times in Fig. 48. We refer to this first appearance of the wave at the observation point as the reference time, t_0. Once the peak of the Gaussian is passed, the derivative changes sign and this source of radiation is quenched. We refer to the arrival of this peak as t_1.

To account for the next peak in the radiated field, at $t - t_1 \approx L/2c \sin\theta$ where $\sin\theta$ accounts for observing at an off-broadside position, let us first consider the boundary condition at the end of the antenna. Because the current is zero, the reflected wave must be of opposite polarity to the incident wave. As a result, the Gaussian suffers a continuous sign reversal at the end as evidenced in Fig. 46. The time derivative of the current for the Gaussian traveling wave along the structure is similar to a doublet. Therefore, it causes a negligible radiation field and reaches a point in time near the end of the antenna where its shape, instead of approximating a doublet, approximates the absolute value of the doublet ($t - t_1 \approx L/2c \sin\theta$). This causes significant radiation from the region near the antenna end and results in the second peak. The third peak is due to radiation from the other end of the antenna, while all subsequent peaks are due to reflections from alternating ends of the antenna as the wave travels back and forth.

In general, the time of arrival of the peaks is given approximately by

$$t_n = t_1 + (L/2c)(n - 1 - \sin\theta);\ n, \quad \text{even}$$

$$t_n = t_1 + (L/2c)(n - 2 + \sin\theta);\ n > 1, \quad \text{odd.}$$

The result of a wider bandwidth calculation is shown in Figs. 50-54, where a 1-m dipole, 0.00674 m in radius and modeled by 48 segments by a Gaussian pulse whose "A" value is 3.25×10^9. A total of 1024 time samples were used for the Fourier transform, of which 480 were computed from the integral equation. We see that the admittance values exhibit the expected resonance behavior to approximately 10 λ, beyond which the characteristic numerical noise dominates the results.

The time-dependent behavior of the loop antenna is considered in Fig. 55. For this particular case, the excitation voltage is assumed

to have a temporal variation described by the time derivative of the Gaussian pulse. This particular excitation is chosen because it does not have a zero-frequency component and therefore does not excite the circulating current that would exist on the closed-circuit structure. The loop is modeled by 22 straight-line segments.

The upper part of Fig. 55 shows the source current as a function of time. The current shape here is very similar to that of the exciting voltage for $P/c < 0.5$; all perturbations to this close tracking are due to electromagnetic coupling effects and not to the arrival of the portions of the pulse which have circulated around the loop.

The input admittance of the loop antenna, plotted in the lower part of Fig. 55, shows excellent agreement with the independently computed results for $P/\lambda \leq 2.5$, beyond which the time-domain derived values progressively depart from the correct results. For loop structures, modeling guidelines[33] indicate that the spatial sample density per wavelength (N_λ) in the frequency-domain must be $6 < N_\lambda \leq 10$, so that the response of the highest frequency component of the incident pulse, which can be accurately determined is approximately $(P/\lambda)_{max} \approx 2.5$. The $(P/\lambda)_{max}$ values from modeling experience in the frequency-domain and our numerical results are thus in close agreement.

The loop antenna calculation was also repeated, using the Gaussian pulse of the previous computations. Although the temporal response of the source current was, of course, quite different in this case and, in fact, reached a steady-state non-zero value for late time, all responses akin to spectral transfer functions (such as input admittance) agreed closely with the results obtained from the Gaussian derivative. This particular calculation can be viewed as a demanding test of the numerical procedure; and considering that the steady-state current became numerically stable in the fourth decimal place, the overall numerical accuracy of the approach is evidently quite good.

The final antenna to be treated here is the zig-zag dipole antenna excited with a Gaussian source. The computed results are shown in Fig. 56. By virtue of the cusps in the wire geometry, this antenna represents a particularly stringent test of the Lagrangian interpolation scheme described below.

For such a structure, the effects of a current in a given segment during a given time step can be felt in adjacent spatial segments during the same time step using, as we have here, $c\Delta t = \Delta z$, Also, the high Q factor of this type of structure tests the ability of the computer program to predict not only late time behavior but also the highly peaked spectral transfer function (input addmittance).

The source current behavior for this structure is plotted in the upper part of Fig. 56, while the input admittance is plotted in the lower part. The agreement between the time- and frequency-domain results is quite good for $L/\lambda < 1.3$, L being the total wire length. With modeling guidelines for zig-zag structures indicating[33] that $N_\lambda \sim 20$ is required for relative errors less than 10%, one finds that $(L/\lambda)_{max} \leq 1.1$ is the approximate limit for accurate results in the frequency-domain, again in reasonable agreement with the calculated data.

c. Wire Scatterers

The technique for determining the behavior of a given wire structure operated as a scatterer of an electromagnetic pulse in the form of a plane wave differs only slightly from that for determining its behavior as an antenna. The difference lies only in the form of the applied field $\bar{E}^A$.

For an antenna, $\bar{E}^A$ is specified as due to a time-dependent voltage: that is, as a tangential electric field over a region at the surface of the wire. For scatterers, the applied field can illuminate the entire structure and is described as a Gaussian traveling wave, expressed in V/m, of the form

$$\bar{E}^A(z,t) = \hat{x} \exp\left\{-A^2\left[z/c - (t - t_{max})\right]^2\right\},$$

where the field is x polarized and the propagation direction is given by $\hat{z}$.

The radiated or scattered field is determined from the computed time history of current. As described previously, an additional temporal translation is introduced at the far-field point in order that the zero time point corresponds to the instant a wave first reaches that observer.

Figure 57 shows the responses of a dipole operated as a scatterer for an incident electric field polarized along the wire axis, with the scattered field computed in the backscatter direction for broadside incidence via Eq. (15). The constants associated with the Gaussian incident field are defined in the figure caption. From these constants, it is easily seen that the spatial width of the applied pulse is approximately equal to the length of the scatterer. The normalized radar cross section is computed from the Fourier transforms of the radiated and applied fields.

A comparison with independent frequency-domain calculations is provided in the lower part of this figure. Not that the results begin to diverge for $L/\lambda \gtrsim 1.5$. This observation is consistent with results already obtained for antennas, based on the space-time sampling density and the excitation pulse width in space relative to the structure's size.

A wider bandwidth calculation for the dipole scatterer using the same model and pulse width employed to obtain the results of Figs. 50-54 is shown in Figs. 58 and 59. The characteristic staircase response of the dipole is obtained to an L/λ value of approximately 10, beyond which the numerical noise predominates.

Figure 60 illustrates the response of a ring, modeled by a 12-sided polygon, to an axially incident Gaussian pulse. As evident from the time response (upper part of the figure), the far field of the loop settles into a ringing mode very rapidly and oscillates at the fundamental frequency (with exponential decay). This indicates a sharp peaking in the frequency response; and indeed this is observed in the lower part of the figure, where the results are compared with independent data. A deterioration brought on by the finite number of samples is again noted at the higher frequencies. Since $N_\lambda \sim 6\text{-}10$ for polygons,[33] we obtain $(P/\lambda)_{max} \approx 1.5$, in agreement with the present time-domain calculation.

The backscatter response of a 48-side polygon model of a ring using the incident pulse and time sampling employed for the wide-band dipole resuls presented in Figs. 58 and 59 is shown in Figs. 61 and 62. It is interesting to observe the relatively fast decay of the scattered field in this case, compared with that shown in Fig. 57. This is evidently due to the larger wire size relative to the ring radius used for this case

compared with that of Fig. 57, thus producing a lower Q scatterer. It is also interesting to see that the ring scatterer exhibits resonances at P/λ values of approximately 1, 5, 9, 13 compared with the dipole resonances which occur at L/λ values of approximately 1/2, 3/2, 5/2, etc.

Extending the single-loop results, we show in Fig. 63 the responses of two coplanar rings to an axially incident Gaussian pulse. An amplitude-scaled version of the incident pulse is shown in the time response. The temporal behavior of the radiated field is somewhat more erratic than that found for the single loop for early times ($t < 2.5\ P/c$) but settles down to a simple ringing mode for later times.

Another observed characteristic is the much lower field strength seen in the double-loop case for times greater than $1.5\ P/c$. The reason for this will become obvious when we look at the time-dependent currents on the rings. The normalized radar cross-section curve exhibits reasonable good agreement with independent results for $P/\lambda < 1.0$, deterioration occuring above that point. A frequency shift seems to have taken place, but aside from this it is encouraging to note that the null point in the response is well predicted. The maximum P/λ for accurate results is computed according to $N_\lambda \sim 6\text{-}10$ so that $(P/\lambda)_{max} \approx 1.5$. Note that this value is near the deep null in the normalized radar cross section (RCS).

In Fig. 64 we see the current at the point on each ring where the incident magnetic field is orthogonal to the ring as a function of time. For very early times, the currents are independent; that is, there is no interaction between the rings. The currents thus start out in phase but lose their phase correlation as the combination of mutual electromagnetic coupling between the rings and their differing natural frequencies takes effect. In fact, for times greater than $1.5\ P/c$, the currents are almost in phase opposition (though differing somewhat in amplitude and period), thus giving rise to oscillations similar to a transmission line (push-pull) mode. The strong peak in the scattered fields at early times and its rapid decay to a lower oscillation level are thereby explained.

Another example of time-domain calculations, the response of a

circular crown band to an axially incident Gaussian pulse, is shown in Fig. 65. The crown band is a zig-zag wire structure 85 in. in length, wrapped on the surface of a cylinder 25.13 in. in circumference. This example is particularly well suited to our approach since it represents a stringent test of the ability of the interpolation scheme described below to allow arbitrary space-time sampling. In fact, for this case, one can easily see that $c\Delta t > \Delta R$; that is, the distance a wave propagates in one time step is greater than the distance between sample points. This in turn allows interactions between various segments within the same time step.

The crown band is also a fine example of a high Q scatterer with a highly peaked response curve in the frequency domain. The slow wave characteristic of the zig-zag structure is exhibited by the ringing period of the radiated field, which in turn is reflected by the resonance in the normalized radar cross section. Agreement with independently computed results is quite good for $P/\lambda < 1.5$.

d. Hybrid Structure Analysis

The treatment of a structure having both wire and surface features can be implemented by combining Eqs. (1) and (14). This basically involves using each equation type to determine the self-interaction of the surface and wire portions, respectively. In addition, the mutual interaction fields must be formulated to account for the effect of each on the current distribution on the other. The latter can be expressed by using Eq. (7) to obtain the electric field on the wire portion due to the surface current distribution, and by applying the thin-wire approximation to Eq. (8) to find the magnetic field of the wire current-distribution on the surface portion of the structure. These manipulations of Eqs. (7), (8), (10), and (14) lead to the coupled set

$$\overline{K}(\overline{r}, t) = 2\hat{n} \times \overline{H}^{inc}(\overline{r}, t)$$

$$+ \frac{1}{2\pi} \hat{n} \times \int_S \left[\frac{1}{c} \frac{\partial}{\partial \tau} \overline{K}(\overline{r}', \tau) + \overline{K}(\overline{r}', \tau) \frac{1}{R} \right]$$

$$\times \frac{\overline{R}}{R^2} ds' + \frac{2\hat{n}}{4\pi} \int_C \left[\frac{\overline{I}(\overline{r}', \tau)}{R} \right.$$

$$\left. + \frac{1}{c} \frac{\partial}{\partial \tau} \overline{I}(\overline{r}', \tau) \right] \frac{\overline{R}}{R} d\ell', \qquad (16a)$$

$$\hat{s} \cdot \bar{E}^{inc}(r, t) = \text{RHS of Eq. (14)} + \hat{s} \cdot \text{RHS of Eq. (7).} \qquad (16b)$$

Bennett, et. al., have obtained numerical solutions for a hybrid structure by employing (16a) for its surface portion, but replacing (16b) by

$$\Box^2 I(x, t) = -\frac{1}{\alpha}\left\{\frac{1}{\eta_0}\frac{\partial E_x^{inc}(x, t)}{\partial t} + \frac{1}{4\pi}\Box^2 \int_{nonself} \frac{I(x', \tau)}{R}\, dx' + \frac{1}{\eta_0}\frac{\partial}{\partial t}\left[\nabla x \frac{1}{4\pi}\int_S \left(\frac{1}{R^2} + \frac{1}{R}\frac{\partial}{\partial \tau}\right)\bar{K}(\bar{r}', \tau) \times \frac{\bar{R}}{R}\, dS'\right]_x\right\} \qquad (16c)$$

where

$$\Box^2 = \frac{\partial^2}{\partial x^2} - \frac{1}{c^2}\frac{\partial^2}{\partial t^2}$$

and

$$\alpha = \frac{1}{2\pi} \ell n\left(\frac{\Delta x + \sqrt{\Delta x^2 + a^2}}{a}\right).$$

This form of integral equation for the wire currents is derived for the special case of straight wire appendages attached to surface structures.

The far-fields of the resulting currents can of course be found from the expressions previously given for the surface and wire current distributions.

Two numerical cases treated by Bennett, et. al.,[10] are shown in Figs. 66 through 71, where the first figure of each set depicts the

scatterer geometry, the second shows the bistatic scattering patterns and the third shows a comparison between the backscatter waveform and the numerical solution. The geometries treated represent the small scientific (SSS) and early warning reconnaissance (EWRS) satellites. The SSS model consists of a sphere with four wire antennas attached at 90 deg intervals around the equatorial plane with the incident pulse traveling down the polar axis. The EWRS model is a right circular cylinder with an aspect length-to-width ration of 3 to 1. It has two perpendicular wire antennas attached at each one of 180 intervals one-third of the length of the cylinder from the end on which the exciting field is axially incident. Again, there is quite good agreement between experiment and theory.

In each case, the influence of the wires can be seen in the backscatter waveform. For the SSS, the initial or specular return is similar to that found for the previous sphere backscatter waveforms, as would be expected. The latter time returns exhibit differences, however, which are attributable to the attached wires. In the EWRS case the effect of the wire antennas is seen as a continuation of the back scattered waveform as the incident pulse propagates down the side of the cylinder. The isolated cylinder would produce no significant return from this region.

The Numerical Solution

The integral equations (more precisely integro-differential equations) derived above for surface, wire, and hybrid geometries are sufficiently different as to require a certain dissimilarity in their numerical treatment. They exhibit in common, however, the influence of the causality which exists between the field at a given observation point and the geometrically separated source current which determines it. It is this property of the time-dependent integral equations, which permits their solution without the matrix inversion normally associated with the corresponding frequency-domain approach.

Consider for example, that at a given instant of time, t, the sampled currents (or fields) for all previous time steps $t - \Delta t$, $t - 2\Delta t$, etc. with t the time step, are known everywhere on the structure. Then it can be

seen from Eqs. (9) and (10), that formally, the unknown current (or field) sample at a given point is completely determined by earlier, hence already known sampled values of the current (or field) on the rest of the structure. But these earlier current (or field) values have themselves been found in the same way, beginning at the time when the known source field has just been turned on, prior to which all quantities are assumed to be zero. Thus, the integral equation can be solved in principle as an initial value problem.

There are of course other factors to consider which may complicate, but not basically change, the rather simple solution procedure just described. If causality is to be satisfied, as it must, in the numerical reduction of the integral equation to a computer algorithm, then we would conclude from the above discussion that $c\Delta t \leq \Delta r$ is required with Δt the time step size and Δr the space sample separation. But this may be an impractical or inefficient restriction to impose (as discussed further below), requiring that the solution procedure be generalized to allow for arbitrary Δt and Δr. The practical result of lifting this restriction is to require that allowance be made for two or more samples to interact within the same time step (i.e., $c\Delta t > \Delta r$). This can be accomplished using time interpolation. Details associated with this procedure are described below.

Solution of the above integral equations can be accomplished using the moment method, the application of which is already well established for frequency-domain formulations. The moment method, described in detail by Harrington,[34] basically involves the reduction of a functional equation to an approximate matrix which can be solved by standard techniques. The time-domain integral equations, however, requiring a time as well as space sampling, can be viewed in matrix form as a repetitive application of a sparse, time-independent matrix operator. From a practical viewpoint this is a process significantly different from the corresponding frequency-domain formulation, even though both solutions are based on the moment method. Essential features of the computer programs, as presently developed, for the surface and wire geometries are outlined below. The hybrid structure will not be discussed, except in passing, since its treatment combines the features of both the surface and the wire geometrics solution methods.

a. Surface Geometries

The most significant differences between the wire and surface integral equations, insofar as their numerical solution is concerned, are that the latter has the unknown outside of, as well as under, the integral, and a lower order derivative appearing in the kernel. Thus, it is possible to solve the surface equation using both a current expansion and space integration method crude in comparison to the one required for the wire.

We select as the current basis function expansion on the surface,

$$\bar{J}(\bar{r},t) = \sum_{i=1}^{N_S} \sum_{j=1}^{N_T} \bar{A}_{ij}(\bar{r} - \bar{r}_i; t - t_j) \times V(\bar{r}_i)\, U(t_j) \qquad (17)$$

where

$V(\bar{r}_i)$ = 1 for $\bar{r}$ on the surface patch of area ΔS_i centered at $\bar{r}_i$ and 0 elsewhere

and

$U(t_j)$ = 1 for t in the time interval Δt centered at t_j and 0 elsewhere.

We also assume $\Delta t_j = \Delta t$, $j = 1, \ldots, N_T$. The $\bar{A}_{ij}$ function may be seen to represent a set of space-time sampled current values on the surface of the structure. Following the already well established frequency-domain approach, we might expect to obtain reasonable accuracy by using the simple pulse approximation for the current, i.e., taking $\bar{A}_{ij}$ to be constant in value over surface patch i and time interval j. This representation actually suffices for integration of the current, allowing surprisingly good accuracy to be obtained from the rather crude approximation that, for example,

$$\int_{\Delta S_i} \bar{J}(\bar{r}') \times \nabla\phi(\bar{r},\bar{r}')\, ds' \approx \bar{J}(\bar{r}_i) \times \nabla\phi(\bar{r},\bar{r}_i)\, \Delta S_i.$$

Integration over the surface patch i is thus achieved by a single integrand sample at the point $\bar{r}_i$, and the temporal current variation over the patch due to the changing retarded time is ignored.

The current time variation might be similarly allowed for, if all space samples were separated by distances which are integral multiples of $c\Delta t$. This is not in general the case. Furthermore, since a current derivative with respect to retarded time appears in the surface integral, it is necessary to perform a current interpolation in time. A polynomial expansion in time allows the required interpolation to be achieved, i.e.,

$$\bar{A}_{ij}(\bar{r}_i, t - t_j) = \bar{A}^{(0)}_{ij}(\bar{r}_i) + \bar{A}^{(1)}_{ij}(\bar{r}_i)(t - t_j) + \ldots + \bar{A}^{(a)}_{ij}(\bar{r}_i)(t - t_j)^a \qquad (18a)$$

where as usual, the expansion coefficients are found in terms of adjacent temporal current samples on either side of the ij'th sample $\bar{A}^{(0)}_{ij}$. If $t - t_j < a\Delta t$, there exists the possibility of interpolating to future current values, in which case the interpolation interval is shifted backwards in time. The a + 1 coefficients in Eq. (18a) are, in any case, found in terms of $\bar{A}^{(0)}_{i,j-b}, \bar{A}^{(0)}_{i,j-b+1}, \ldots, \bar{A}^{(0)}_{i,j-b+a}$, which are sampled values of the current on patch i at times $t_j - b\Delta t, t_j - (b-1)\Delta t, \ldots, t_j - (b-a)\Delta t$ respectively. Thus,

$$\bar{A}_{ij}(\bar{r}_i, t - t_j) = \sum_{d=0}^{a} A^{(0)}_{i,j-(b-d)} \times \sum_{e=0}^{a} B_{d,e}(t - t_j)^e, \qquad (18b)$$

where the interpolation function $B_{d,e}$ is explicitly determined by the particular interpolation order.

Thus, we have a space-time current representation suitable for the

surface geometry integral equation. Upon inserting Eq. (17) into the integral equation [Eq. (10)], performing the integration over the sample patches, and collocating the observation points at the patch centers, we formally obtain

$$\bar{A}_{ij}^{(0)} = 2\hat{n}_i \times \bar{H}_{ij}^{I} + \frac{1}{2\pi}\hat{n}_i \sum_{i'=1}^{N_S} \times \left\{ \sum_{d=0}^{a} A_{i',j'-(b-d)}^{(0)} \sum_{e=0}^{a} B_{d,e} \times \left[(t' - t_{j'})^e \frac{1}{R_{ij'}^3} + e(t' - t_{i'})^{e-1} \times \frac{1}{R_{ii'c}^2} \right] \bar{R}_{ii'}, \Delta S_{i'} \right\} \tag{19}$$

where

$$\bar{R}_{ii'} = \bar{r}_i - \bar{r}_{i'}, \qquad j = 1, \ldots, N_T$$

$$i, i' = 1, \ldots, N_S$$

$$R_{ii'} = |\bar{R}_{ii'}|$$

$$t' = t - R_{ii'}/c\Delta t, \quad t = t_0 + (j-1)\Delta t$$

$$j' = j - r_{ii'}$$

with $r_{ii'}$ being the rounded off value of $R_{ii'}/c\Delta t$.

We observe, that if $\bar{A}_{i'j'}^{(0)}$ is known for $j' \leq j - 1$, that Eq. (19) allows a simple arithmetic calculation of $\bar{A}_{ij}^{(0)}$, $i = 1, \ldots, N_S$, if $c\Delta t \leq \Delta r_{min}$ with Δr_{min} the minimum value of $R_{ii'}$. If however, $c\Delta t < \Delta r_{min}$, then the situation arises where $\bar{A}_{ij}^{(0)}$ is dependent upon the value of $\bar{A}_{i'j}^{(0)}$, i.e., it is a function of the current on other patches at the present time step. It is then but a simple matter to rewrite

Eq. (19) in matrix form with $\overline{A}_{ij}^{(0)}$ the unknowns, and i = 1, . . ., N_S and j arbitrary. The resulting matrix will be very sparse, and can be solved by the usual techniques, to obtain a simultaneous solution for the coupled surface-current values at each time step. The matrix coefficients are themselves independent of time, so that the matrix solution need be performed but once. Note that the matrix coefficients are determined solely by the structural geometry, its segmentation, and the time interpolation method used. The time-domain surface program used to generate the numerical results presented in this paper has been developed subject to the condtion that $c\Delta t \leq \Delta r_{min}$. Its extension to allow for more general time-space current sampling should be straight forward.

The computer time required to find the time-dependent surface current by a stepwise solution of Eq. (19) will usually exceed that necessary for all subsequent calculations. Evaluation of the far-field, for example, is by comparison a generally more efficient procedure in either the time- or frequency-domain (via Fourier Transform). In this regard, it might be noted that the efficiency of such computations can be a sensitive function of the order in which they are performed. Calculation of the backscatter cross-section in the frequency-domain could be performed by either Fourier transforming the time-dependent backscattered field, or first Fourier transforming the surface current distribution, from which the direct frequency behavior of the backscattered field can be found. The former approach requires only a single Fourier transorm, however, while the latter entails N_S such transforms and so can be considerably less efficient.

b. Wire Geometries

A solution of the wire version of the time-domain integral equation can be expected, if our frequency-domain experience is any guide, to require a more elaborate numerical treatment than the surface integral equation. It has been found in the frequency-domain, for example, that the surface integral equation can be solved with reasonable accuracy using impulse current samples and a single integrand sample per patch. The wire equation, on the contrary, greatly benefits from sub-segment

integration and a higher order current expansion. Even then, the maximum sample separation that can be used in general is on the order of one-sixth the wavelength compared with the one-fourth wavelength separation found to be acceptable in some cases for the surface equation. At the risk of some degree of oversimplification, this difference may be attributed to the differences between the two equations in the order of their respective integrand simularities and the fact that the surface and wire equations are Fredholm equations of the second and first kind, respectively.

We can thus expect that, at a minimum, a space integration will be necessary to evaluate the interaction fields of the wire currents, even when impulse current samples are employed. And as already noted, if $jc\Delta t \neq \Delta r$ is to be allowed for, time interpolation is also necessary, particularly to allow for the mutual interactions within the same time step which occurs when $c\Delta t > \Delta r$. But since retarded time varies with position along a given current-segment, it becomes necessary to allow for this when performing the space integration. Space interpolation of the current is thus also in order if the space-time current representation is to be reasonably self-consistent and numerically efficient.

Two-dimensional interpolation can be accomplished via one of many standard methods. The relationship between the space and time sample points is illustrated by Fig. 72, where the mutual interaction region for the ij'th sample point (i ~ space, j ~ time) is confined to the lines along the light cone. It may be concluded from this diagram that the space-time patch involved in integrating over current segment i' at time step j' is a line along the light cone from midway between segments i' - 1 to i' + 1. This integration path requires a current expression accurate over the entire ij'th sample patch. For this reason we adopt a general quadratic space-time current expansion which includes all products to second order in space and time, i.e.,

$$A_{ij}(s - s_i, t - t_j) = A_{ij}^{(0)} + A_{ij}^{(1)}(t - t_j) + A_{ij}^{(2)}(t - t_j)^2 + A_{ij}^{(3)}(s - s_i)$$

$$+ A_{ij}^{(4)}(s - s_i)(t - t_j) + A_{ij}^{(5)}(s - s_i)(t - t_j)^2 + A_{ij}^{(6)}(s - s_i)^2 + A_{ij}^{(7)}(s - s_i)^2(t - t_j)$$

$$+ A_{ij}^{(8)}(s - s_i)^2(t - t_j)^2$$

where the expansion coefficients $A_{ij}^{(0)}, \ldots, A_{ij}^{(8)}$ are obtained from interpolating the ij'th current to the currents at the centers of the adjacent space-time samples. As before, we avoid future current samples by adjusting the interpolation interval. We also interpolate I to zero at the wire ends. After performing this interpolation we can express the current on space-time sample ij in the manner of Eq. (18b) already used fo the surface-current representation. With quadratic terms in both s and t, we obtain the general form

$$I_{ij}(s_i'', t_j'') = \sum_{\ell=-1}^{\ell=+1} \sum_{m=n}^{m=n+2} \times B_{ij}^{(\ell,m)} I_{i+\ell,j+m}, \qquad (20a)$$

where

$$B_{ij}^{(\ell,m)} = \prod_{p=-1}^{p=1}{}^{\ell} \prod_{q=n}^{q=n+2}{}^{m} \times \frac{(s' - s_{i+p})(t' - t_{j+q})}{(s_{i+\ell} - s_{i+p})(t_{j+m} - t_{j+q})}$$

$$= \prod_{p=-1}^{p=+1}{}^{\ell} \prod_{q=n}^{q=n+2}{}^{m} \times \frac{(s_i'' + s_i - s_{i+p})(t_j'' + t_j - t_{j+q})}{(s_{i+\ell} - s_{i+p})(t_{j+m} - t_{j+q})} \qquad (20b)$$

with $|s_i''| \leq \Delta s/2$, $|t_j''| \leq \Delta t/2$, n = -2 for $R/[c\Delta t] < 0.5$ and -1 otherwise. The spatial and temporal sample sizes are denoted by Δs and Δt respectively and the superscripts ℓ and m on the product symbols denote that the terms $p = \ell$, $q = m$ are omitted from Eq. (11). Substitution of this current expansion and of similar forms for the charge and current derivative terms into the original integral equation

together with a linear piecewise modeling of the original structure, leads to an integral equation similar in form to that for the surface, Eq. (19). This equation is very complicated, but we include it here for the sake of completeness; it is discussed in detail by Miller, Poggio, and Burke.[11]

$$\overline{\overline{Z}} \cdot \overline{I}_v = \overline{E}_v + \sum_{\ell=-1}^{+1} \sum_{m=n}^{n+2} r_{i-\ell,u}$$

$$\times \overline{\overline{X}}^{(\ell,m)} \cdot \overline{I}_{v-r_{i-\ell,u}+m} + \sum_{\ell=-1}^{+1}$$

$$\times \sum_{r=-1}^{+1} \sum_{m=n'}^{n'+2} \sum_{t=n}^{n+2} \left\langle \frac{r_{i-\ell-r,u}+|m|+1}{2} \right\rangle$$

$$\times \overline{\overline{W}}^{(\ell,m,r,t)} \sum_{s=1}^{v-r_{i-\ell-r,u}+m}$$

$$\times \overline{I}_{v-r_{i-\ell-r,u}+m+t+1-s}, \qquad (21)$$

where

$$Z_{ui} = \frac{\mu_0}{4\pi} \hat{s}_u \cdot \sum_{\ell=-1}^{+1} \left\{ \int_{-\Delta/2}^{\Delta/2} ds''_{i-\ell} \right.$$

$$\times \sum_{p=0}^{1} \delta(r_{i-\ell,u} - p) \left[\frac{\hat{s}_{i-\ell}}{R_{i-\ell,u}} \, {}_tB_{i-\ell}^{(\ell,p)} \right.$$

$$\left. \left. + c \frac{\overline{R}_{i-\ell,u}}{R_{i-\ell,u}^2} \, {}_sB_{i-\ell}^{(\ell,p)} \right] - c^2 \right.$$

$$\times \sum_{r=-1}^{+1} \int_{-\Delta/2}^{\Delta/2} ds''_{i-\ell-r}$$

$$\times \frac{\overline{R}_{i-\ell-r,u}}{R^3_{i-\ell-r,u}} \sum_{q=0}^{2} \delta(r_{i-\ell-r,u} - q)$$

$$\times B^{(\ell,\langle q/2\rangle)}_{i-\ell-r} \, C^{\left(r,\langle\frac{q+1}{2}\rangle\right)}_{i-r} \Bigg\}$$

and

$$X^{(\ell,m)}_{ui} = -\frac{\mu_0}{4\pi} \hat{s}_u \cdot \Bigg\{ \int_{-\Delta/2}^{\Delta/2} ds''_{i-\ell}$$

$$\times \left[\frac{\hat{s}_{i-\ell}}{\overline{R}_{i-\ell,u}} \, {}_tB^{(\ell,m)}_{i-\ell} + c \, \frac{\overline{R}_{i-\ell,u}}{R^2_{i-\ell,u}} \, {}_sB^{(\ell,m)}_{i-\ell} \right] \Bigg\}$$

$$W^{(\ell,m,r,t)}_{ui} = c^2 \frac{\mu_0}{4\pi} \hat{s}_u \cdot \int_{-\Delta/2}^{\Delta/2} ds''_{i-\ell-r}$$

$$\times \frac{\overline{R}_{i-\ell-r,u}}{R^3_{i-\ell-r,u}} \, B^{(\ell,m)}_{i-\ell-r} \, C^{(r,t)}_{i+\ell}$$

$${}_tB^{(\ell,m)}_i = \sum_{w=+n}^{w=n+2} {}^{m} \frac{1}{(t' - t_{j+w})} \, B^{(\ell,m)}_{ij}$$

$$= \sum_{w=n}^{w=n+2} {}^{m} \frac{1}{(t''_j + t_j - t_{j+w})} \, B^{(\ell,m)}_{ij} .$$

$${}_sB^{(\ell,m)}_i = \sum_{r=-1}^{r=1} {}^{\ell} \frac{1}{(s' - s_{i+r})} \, B^{(\ell,m)}_{ij}$$

$$= \sum_{r=-1}^{r=+1} {}^{\ell} \frac{1}{(s''_i + s_i - s_{i+r})} \, B^{(\ell,m)}_{ij} .$$

$$C^{(\ell,m)}_i = \left[-\Delta t \sum_{r=-1}^{r=+1} {}^{\ell} \frac{1}{(s_i - s_{i+r})} \right.$$

$$\times \prod_{p=-1}^{p=+1}{}^{\ell} \frac{(s_i - s_{i+p})}{(s_{i+\ell} - s_{i+p})} \Bigg]$$

$$\times \Bigg[\sum_{s=0}^{s=1} \prod_{q=n}^{q=n+2}{}^{m} \frac{q^s}{(m - q)} \Bigg] .$$

Also, $\langle\ \rangle$ signifies round off to the lower integer value, $R_{i,j} = |\bar{r}_j - \bar{r}_i - \bar{s}_i|$ with $\bar{s}_i$ measured along segment i from its center at $\bar{r}_i$ and $r_{i,j} = R_{i,j}/c\Delta t$ rounded off to the closest integer value.

The added complexity of the wire equation over that for the durface is primarily due to the extra space interpolation employed and to the extra term which appears in it. Its extension to the multiple junction case would be even more involved. The wire equation is also solvable as an initial value problem, prior to which a geometry dependent sparse matrix must be inverted. The procedure is described in more detail by Miller, Poggio, and Burke.[11]

c. Factors Common to the Wire and Surface Formulations

Although the specific details of their numerical solutions differ, there are aspects of the surface and wire formulations which are similar enough to be jointly considered. Among them are the questions of accuracy, beginning and terminating the solution in time, and the influence of symmetry

d. Accuracey

The numerical accuracy attainable using a time-domain approach is dependent upon more factors than is the corresponding problem in the frequency-domain. Common to both domains, however, are the questions of spatial sampling relative to the wavelength(s) involved and the proper geometric modeling of the structure being considered. The former question has been considered rather thoroughly by Miller et al.[33] for wire geometries and is discussed for surface geometries by Poggio and Miller.[7] The latter problem concerns the use of a numerical model which not only meets spatial sampling requirements, but adequately conforms to the actual structural geometry. It is particularly

demanding for structures which are of complex shape or construction.

Unique to the time-domain formulation are the problems of (1) temporal sampling requirements, (2) the exciting pulse shape, and (3) the ratio of body-size to the pulse width in space. These questions are considered separately below.

a. Temporal Sampling Requirements

The exciting source and the currents and fields which it produces must be sampled at a sufficient rate in time to adequately resolve their temporal variation, much as their spatial variation requires a certain spatial sample density. The temporal sample density should be chosen so as to provide an accuracy compatible with that obtainable from the spatial sample density. In this way, neither sampling rate alone, but both together, determine the overall numerical accuracy. As a consequence, the total computer time required to obtain a given accuracy can be minimized.

We already have developed some spatial sample density guidelines, i.e., $\Delta R \sim \lambda/S$ where S is on the order of 4 to 8 for the surface integral equation and varies from 6 to 20 for the wire integral equation, depending upon the structural complexity. Now we inquire as to what value of Δt will be compatible with this Δx, insofar as the overall solution accuracy and computer time are concerned. This is a question which is difficult to answer without some consideration of how accuracy is to be defined, a topic discussed further below in connection with the pulse shape used for the calculation. For the present, we ignore the specifics of defining accuracy and proceed instead on a sampling theorem basis.

The Shannon-Kotelinkov Sampling Theorem states that the maximum resolvable frequency F of a band-limited spectrum using a temporal step size of Δt is $F = 1/2\,\Delta t$. According to the preceding discussion we then have $\Delta R \sim \lambda/S = c/FS = c2\Delta t/S$. We then conclude that for surfaces

$$\Delta R \sim c\Delta t/2 \text{ to } c\Delta t/4,$$

while for wire structures

$$\Delta R \sim c\Delta t/3 \text{ to } c\Delta t/10.$$

This result implies that if we are to in any way optimize the computer time required to obtain results accurate up to the frequency F, then adjacent spatial samples must be allowed to interact within the time Δt.

There may appear to be an inconsistency, however, in requiring only two samples per temporal cycle, while requiring up to 20 samples per spatial cycle. The reason for this difference in sampling rates lies in the character of the time and spatial variation of the currents and fields themselves. The spatial variation of the current on a structure when excited by a monochromatic source of frequency F, except in special cases such as an infinite two-wire transmission line, is not a spatial sinusoid with a wavelength $\lambda = c/F$. It can instead, as a minimum, consist of oppositely traveling waves of length λ or exhibit an even more complex variation when represented by a spatial Fourier series, which extends to several spatial harmonics of λ. This behavior of the current plus the approximations associated with the numerical colution procedure itself, can require many times the minimum two samples per wavelength. The temporal variation, on the other hand, can be sampled as to phase and amplitude at the frequency F using two data points. If, however, the time interpolation method uses other than a sinusoid variation of frequency F, quadratic interpolation for example, then more than two samples per temporal cycle may be necessary. Quadratic interpolation has been found to require more samples per wavelength (i.e., result in a larger value for s) than sinusoidal interpolation for the frequency-domain treatment of wire structures.

The results derived above can be used to obtain an estimate of the maximum L/λ value for which transient calculations of a wire structure of length L will be valid. This estimate[11] is

$$(L/\lambda)_{max} \simeq N_T\left(\frac{L}{cT}\right) \min\left(\frac{1}{2}, \frac{1}{\alpha N_\lambda}\right), \qquad (22)$$

where $\alpha = \Delta R/c\Delta t$, N_λ is the spatial sample density per wavelength, and N_T is the number of time samples over the exciting pulse (assumed Gaussian) whose spatial extent is $\sim cT$. Transient calculations for several wire structures (see examples in this paper) have produced

data in agreement with this formula. However, since $c\Delta t = \Delta R$ was used for the most part, the temporal sample density limitation on accuracy (the first term in the bracket of Eq. (22) was not tested.

f. Exciting Pulse Shape

One of the attractive features of transient calculations is the wide bandwidth information which they are potentially capable of providing in but a single computer run. It is obvious that a wide bandwidth exciting source is required to realize this capability. This implies the use of a short pulse in time, something approaching a delta function. Delta functions are convenient to employ theoretically, but they cannot be used numerically; it is convenient instead to use a Gaussian pulse shape, which in the limit of vanishing duration approaches the delta function.

The time-domain Gaussian pulse of unit amplitude is given by

$$g(t) = (A/\sqrt{\pi})e^{-t^2A^2}$$

and has the frequency-domain counterpart

$$G(f) = e^{-\pi^2 f^2/A^2} .$$

The 0.1 values of the pulse occur in the time and frequency-domain when $t \sim 1.5/A$ and $f \sim 0.5A$ respectively. If we assume $F \sim 0.5A$, then $\Delta t \sim A^{-1}$ is implied. Upon letting the temporal (and spatial) pulse widths be denoted by W_T (and W_S) we have that $W_T \sim 3/A$, so that $\Delta t \sim W_T/3$. This means that we would sample the pulse, at a minimum, only three times between its 0.1 values, 4.3 times between its 0.001 values. This sampling rate is somewhat lower than that of the 10 samples per W_T used for the numerical results presented here. However, the relationship $F \sim 1/2\Delta t$ is true under optimum conditions, which cannot be necessarily assumed to hold in actual practice, particularly since the time interpolation is achieved via polynomial interpotation.

It might be asked whether other pulse shapes might be better suited for numerical purposes than the Gaussian. The answer to this

depends upon numerous factors, foremost among them being the error-generating mechanisms associated with the numerical computation the way in which these errors accumulate in the final answer. Assessment of the error impact on the computed results requires some criteria for judging the numerical accuracy of the result. Such a judgement may be more easily made because of prior experience in the frequency-domain.

Let the exact frequency-domain response of the structure, current, far field, etc., be denoted by $R(f)$, and the computed response by $\tilde{R}(f)$. The error in $\tilde{R}(f)$, $N(f)$, numerical noise analogous to that in an electronic circuit, can be defined by

$$N(f) = [\tilde{R}(f) - R(f)]/R(f).$$

In most applications, it would be desired that the signal-to-noise (error)-ratio, $S(f) = \tilde{R}(f)/N(f)$, exceed some value over the range of f being considered. For simplicity of analysis, assume $S(f) = S$ over the range* 0 to F.

Now, how might we assure that the desired S is actually achieved in our numerical computation? Recall that $\tilde{R}(f)$ is obtained from the ratio $H(f)/G(f)$ with $H(f)$ being the Fourier Transform of the transient waveform $h(t)$ due to the exciting source $g(t)$. The function $G(f)$ is known analytically, for a Gaussian pulse at least, so that any error in $\tilde{R}(f)$ comes directly from $H(f)$.

Application of the finite Fourier transform to $h(t)$ to compute $H(f)$ may be viewed as a matrix operation, whereby the sequence of sampled values for $h(t)$ is multiplied by a Fourier Transform matrix operator. The operator is also analytically known and thus exact so that the errors in $H(f)$ come only from $h(t)$. Since errors are cumulative in addition or subtraction, the errors in $h(t)$ will be additive for each sampled value of $H(f)$. We thus conclude that $S(f)$ will have a relatively constant value over f, if $H(f)$ is also relatively independent of f. But since $H(f) = G(f)\tilde{R}(f)$, we find that a frequency independent $H(f)$ requires that

$$G(f) \sim \tilde{R}^{-1}(f),$$

*In actual practice the low frequency response, the Rayleigh region of a scatterer for example, may not be essential, so that the range in f might be from some non-zero lower limit to F.

i.e., the exciting pulse should have a time variation which is the Fourier Transform of the inverse frequency response of the structure.

This is a rather interesting result, but since the idea of the calculation is to find $\tilde{R}(f)$, of what use is it? The answer would seem to be that it offers the potential for increasing the value of F for which the results will be valid by performing a few iterations in the calculation of H(f). We could, for example, initially use the Gaussian pulse from which $H_0(f)$ is obtained. A new $G_1(f)$ obtained from $\tilde{R}_0^{-1}(f) = G_0(f)/H_0(f)$ could then be used to find a new $H_1(f)$, and thence if desired, a new $G_2(f)$. This process might be repeated until the results for H(f) stabilize. The potential advantage of following this procedure is that, as shown below, the computer time for a transient calculation varies with wire length L or body radius a, by to $(kL)^4$ and $(ka)^6$ respectively. Thus, if by p of the iterations above, the effective range of validity in f can be extended to (1 + y)F, a computer time savings can be effected if

$$p(kL)^4 < [kL(1 + y)]^4$$

or

$$p(ka)^6 < [ka(1 + y)]^6$$

for wire or surface structures respectively.

Note that using $G(f) \sim \tilde{R}^{-1}(f)$ de-emphasizes the structural resonances and enhances the anti-resonant response. As a result, the induced response h(t) will become approximately Gaussian. The computation time may then be reduced because fewer time steps would be required for h(t) to become negligible as a result of not exciting the structure at its resonant frequency (ies).

g. Pulse Width Relative to Body Size

The influence of the temporal and spatial sampling rates on the maximum frequency, F, for which valid numerical results can be expected, has been discussed. The ratio of the body size to pulse width is also a factor to be considered in this regard.

The temporal sampling rate must be sufficient to adequately resolve

the time variation of the exciting pulse. The pulse time duration W_T must thus contain some minimum number of time steps of length Δt. In addition, W_T must be sufficiently short as to contain significant frequency components up to F, upon whose wavelength the spatial sampling rate is based.

The pulse width in time can be defined to be the time interval over which the pulse exceeds some fraction of its maximum value, say V. Then for a Gaussian pulse, for example

$$W_T = (2/A)\sqrt{-\ell nV}$$

and the corresponding spatial pulse width W_S is given by

$$W_S = cW_T.$$

The time- and frequency-domain forms for the Gaussian pulse then become

$$g(t) = (2/W_T)\sqrt{-\ell nV/\pi}$$

and

$$G(f) = e^{\pi^2 f^2 W_S^2/c^2 4\ell nV}.$$

Now let the spatial pulse width be some fraction w of the minimum diameter (d) sphere in which the structure can be enclosed, i.e.,

$$W_S = d/w.$$

Then G(f) can be written

$$G(f) = e^{(kd/4w)^2/\ell nV}$$

so that G(f) decreases to the value V when

$$kd = 4w|\ell nV|.$$

Since the spatial sample separation Δx is given by λ/S as discussed above, we find that

$$w = \frac{\pi d}{2|\ell nV|\Delta xS}.$$

Thus, once the spatial sampling rate, or maximum d/λ value, has been selected, the exciting pulse width is fixed.

From previous discussion it was determined that

$$A^{-1} \simeq \Delta t = (\pi/2A\sqrt{-\ell nV}) = \frac{W_T \pi}{4|\ell nV|}.$$

In the present case we obtain

$$\Delta x \sim \frac{\pi W_s}{2S|\ell nV|} ,$$

from which

$$\Delta x \sim \frac{2c\Delta t}{S} ,$$

in agreement with the result derived from sampling considerations alone.

h. Beginning and Terminating the Solution in Time

One aspect of the time-domain formulation that requires special attention is that of determining the first non-zero current values as the exciting source is initially turned on. The Gaussian pulse for example is non-zero for all times which are finitely different from t = 0. Numerically, of course, early time source values that are sufficiently small should have no practical effect upon the eventual solution. The problem arises then of establishing at what point in the source buildup the solution should be started. Similar observations apply to the truncation of the time-stepping solution, where the induced current level, rather than the source strength, is the determining factor.

The numerical results presented here have been obtained starting with source strengths 10^{-3} to 10^{-2} of the maximum source value. This level appears sufficiently small so as not to limit the accuracy of the calculations. Time interpolation of the current and charge is performed using zero values for prior time samples of these quantities. In some instances it has been found expedient to begin the solution using shorter time steps, and to increase the temporal sampling interval after the first several time samples have been obtained.[8]

The point at which the solution process can be stopped depends entirely on the transient characteristics of the structure. Some geometrical shapes, the sphere for example, do not exhibit sharp resonances, and as a consequence the calculation can be terminated a relatively short time after the exciting pulse has decayed to the point where it has no practical effect. Resonant structures, such as the crown band scatterer, give results (Fig. 56) which may exhibit very

slowly decaying currents and fields. These require continuing the solution for many time steps unless some suitable method, which has the effect of increasing the decay rate, can be found. A simple means of accomplishing this, at least for structures with one or a few persistent harmonics, is to obtain their periods and decay constants early in the calculation, and to then analytically extrapolate the resultant waveform to the point of acceptable convergence. This procedure can drastically reduce the number of time steps required for the overall solution. Impedance loading can also accomplish this.

It is interesting to note that the number of time samples used to set up the finite Fourier Transform to the frequency domain can be adjusted with the goal of improving the appearance of the frequency-domain data. By the artifice of adding zeroes (or analytically calculated extrapolated data) to the calculated values and thus widening the time window of the Fourier Transform, interpolation or smoothing of the frequency-domain data is achieved. This occurs since the interval in frequency (Δf) between calculated data points is given by $\Delta f = 1/T$, with T the total time window, while the frequency interval covered is $F = 1/2\ \Delta t$. If Δt remains unchanged while T is increased, then Δf decreases effecting a frequency interpolation.

i. Symmetry

As is true in frequency-domain solutions, computer time and storage requirements can be dramatically decreased by exploiting structural mirror and rotational symmetry in the time-domain approach. The effect of symmetry can reduce the number of independent currents which must be solved for, as well as allowing decomposition of the source into modes for which the resultant currents can be more efficiently obtained.

Consider as an example, a scatterer having a wave of arbitrary polarization incident in a plane of symmetry. By decomposing the source into TE and TM modes with respect to the symmetry plane, the number of current unknowns can be reduced by a factor of two by reason of their even or odd symmetry about the mirror plane of the body. The computation time then changes from the order of N^2N_T to $2N^2N_T/4$, the multiplier coming from the two polarizations which must be solved for. For

rotationally symmetric bodies and axially incident sources the decrease can be even more substantial since the current sampling then becomes a function of the body size rather than surface area. Further aspects of structural symmetry are discussed by Poggio and Miller.[7]

IV. COMPARISON WITH FREQUENCY-DOMAIN APPROACHES

The frequency- and time-domains offer alternative methods for obtaining the same information. A paramount question concerning their use is the relative advantages they offer for the solution of the same problem. Of particular interest here, of course, is the time-domain formulation. We must ask whether it truly offers an advantage in any given instance over the frequency-domain approach, or is it simply a unique and novel way of deriving the same information. These are the questions to which the discussion below is addressed.

Computer Time Requirements

An especially important factor in establishing the relative merits of competing computational methods applicable to the same problem is that of the computer time which they require. We will develop general expressions in this section for the frequency- and time-domain computer time requirements, from which comparisons will be made for specific problem types (i.e., mono-static RCS time response, single frequency bistatic antenna patterns, etc.).

a. Frequency Domain

There are four basic steps involved in obtaining the frequency-domain solution for a given structure. They are (1) Computation of the impedance matrix from the geometrical data; (2) factorization, inversion, or other solution of the linear system to obtain the admittance matrix; (3) calculation of the currents induced on the structure by the specifiedsource(s); and (4) evaluation of observables such as the far-field radiation pattern or near-field behavior. In terms of the number of current samples N, the calculation time (t_f) for a single frequency can be written in the same order as steps (1)-(4) as

$$t_f \sim A_f N^2 + B_f N^3 + C_f N^2 N_I$$

$$+ D_f N N_I N_A \qquad (23)$$

where the coefficients $A_f, \ldots, D_f$ are computer and algorithm dependent timing coefficients, N_I is the number of separate sources considered and N_A the number of viewing angles in the far-field. For simplicity we limit our attention to structures without symmetry, consider only solution via factorization, and include field computations for the far-field only. This and subsequent discussion are, furthermore, order of magnitude only and are for puposes of making a gross comparison between the time- and frequency-domains.

The order in N of the various terms in Eq. (23) is easily established. Matrix fill time is of order N^2, since the interaction of each of the N segments with its N neighbors must be determined, while matrix factorization is well known to be of order N^3. The current computation is of order N^2, since it involves the multiplication of an N-dimensional source vector to find each of the N currents. Far-field evaluation time is of order N, since N current segment contributions must be summed for each field point.

Numerical evaluation of t_f requires the relationship of N to the body size in wavelengths. Previous studies have shown that about 2π current samples per wavelength are required for the analysis of wire structures when using the sinusoidal current expansion and the electric field integral equation. Similarly, on the order of 12π samples per square wavelength (noting that two current components must be sampled every 1/4 wavelength) are necessary for the treatment of surface objects via the magnetic field integral equation.

Let $\lambda_u (f_u)$ correspond to the shortest wavelength (highest frequency) for which the transient calculation is to apply. Then on the order of $N_u \sim 2\pi L/\lambda_u$ and $12\pi A/\lambda_u^2$ current samples at a maximum will be required for a wire of length L or surface of area A. For the latter we assume $A \sim 4\pi a^2$ with a being the radius of the minimum

enclosing sphere. In addition, we let the number of current samples at a frequency step i, $i = N_t, N_t + 1, \ldots, N_f$ by given by $N_i = iN_u/N_f$ and $N_i = i^2N_u^2/N_f^2$ for the wire and surface cases respectively, with corresponding values for N_f given by $N_f \sim 2\pi L/\lambda_u$ and $N_f \sim 2\pi k_u a$. For simplicity we will use $N_t = 1$. The angular sampling rates N_I and N_A are similarly taken to be $\sim 2\pi N$ for 2π radian coverage of the two principal polarizations, or $\sim 12\pi L/\lambda_u$ and $12\pi a/\lambda_u$ for wires and surfaces respectively. These values are derived from consideration of the minimum sampling required to represent monostatic or bistatic angular patterns or aspect-constant frequency variations using $\sim 2\pi$ samples per unit wavelength change in length (L/λ_u) or circumference (C/λ_u). Then, upon summing Eq. (22) over $i = 1, \ldots N_f$ for wire and surface structures, we obtain the computation times for transient analysis as

$$T_{fw} \sim \sum_{i=1}^{N_f} t_{fwi} \sim \frac{N_f^3}{3} A_{fw} + \frac{N_f^4}{4} B_{fw} + \frac{2\pi N_f^3}{3} D_{fw} + \begin{cases} \frac{2\pi N_f^4}{4} C_{fw} \\ \frac{N_f^3}{3} C_{fw} \end{cases} \tag{24a}$$

$$T_{fs} \sim \sum_{i=1}^{N_f} t_{fsi} \sim \frac{N_f^5}{80} A_{fs} + \frac{N_f^7}{448} B_{fs} + \frac{\pi N_f^4}{8} D_{fs} + \begin{cases} \frac{\pi N_f^6}{48} C_{fs} \\ \frac{N_f^5}{80} C_{fs} \end{cases} \tag{24b}$$

where the upper part of each bracket refers to a monstatic calculation and the lower part to a single-source bistatic calculation. Note that since $N_f \sim 2\pi L/\lambda_u$ for wires and $2\pi k_u a$ for surfaces, the corresponding computation times increase as the fourth and seventh powers of the frequency! The Fourier transform time, on the order of $N_f \log_2 N_f$, is not included here since it is usually insignificant compared with the other time requirements.

It is worthwhile to include the corresponding computer time requirements for a single frequency calculation using the frequency-domain formulation. They are, at frequency f_u,

$$t_{fw} \sim N_f^2 A_{fw} + N_f^3 B_{fw}$$

$$+ 2\pi N_f^2 D_{fw} + \begin{cases} 2\pi N_f^3 C_{fw} \\ N_f^2 C_{fw} \end{cases}$$

$$t_{fs} \sim \frac{N_f^4}{16} A_{fs} + \frac{N_f^6}{64} B_{fs}$$

$$+ \frac{\pi N_f^3}{2} D_{fs} + \begin{cases} \frac{\pi N_f^5}{8} C_{fs} \\ \frac{N_f^4}{16} C_{fs} \end{cases}$$

The above expressions for T_f yield the approximate solution times for obtaining transient scattering or radiation information using a frequency-domain formulation. Single freqeucny computation times are obtained from t_f evaluated with f_u equal to the frequency of interest. Note incidentally that Eqs. (24a) and (24b) make use of frequency-variable segmentation and viewing-angle sampling densities. The use of a single model for the entire frequency range which might be more convenient, could increase the calculation times by a factor

of up to 7, the actual value for each term being the exponent of N_f in that term.

Numerical values of the coefficients (in seconds on a CDC 6600) in Eq. (24) for the surface and wire programs under consideration are approximately:

	A_f	B_f	C_f	D_f
Surface	3×10^{-4}	5×10^{-6}	2×10^{-5}	1×10^{-4}
Wire	2×10^{-3}	5×10^{-6}	2×10^{-5}	3×10^{-4}

The B and C coefficients are the same for both programs since these operations are performed by common subroutines. Note that for the surface program and single frequency calculation, the matrix inversion time exceeds matrix fill time for $N > 60$, while the increased matrix fill time for the wire program due to more complex matrix coefficients necessitates that $N > 400$ before inversion time dominates. For transient calculation, the corresponding values for N, when inversion time dominates, are 75 and 533 respectively.

b. Time Domain

A time-domain solution involves the following steps: (1) computation of the geometry dependent matrix (and its inverse if interaction within a time step is allowed for); (2) step-by-step calculation of the time dependent current; (3) computation of the time-dependent far field; and (4) Fourier transform to the frequency domain (if desired) of the current or far-field. The calculation time can be written in the same order as steps (1) - (4),

$$T_t \sim A_t N^2 N_T N_I + B_t N_T N_I N_A, \qquad (25)$$

where N_T is the number of time steps, and N_I and N_A the number of incident fields and far-field observation points, as before. In writing Eq. (25), we neglect the matrix setup time (1) and the Fourier transform time (4) as being relatively unimportant.

Coefficient values (in seconds on a CDC 6600) for the surface and wire time-domain programs under discussion are:

	A_t	B_t
Surface	4×10^{-4}	1×10^{-4}
Wire	1×10^{-4}	2×10^{-5}

The various sampling rates in Eq. (25) can be expressed in terms of the number of frequency steps, N_f, as already done for the frequency-domain calculation. For example, it can be concluded that the approximate equality of N_T and $2N_f$ is essentially due to the fact that the time-domain quantities such as current, scattered field, etc. are real, whereas in the frequency-domain they are complex (i.e., have a phase and magnitude). We also know from our frequency-domain discussion that N_A and $N_I \sim 2\pi N_f$, while $N \sim N_f$ for wires and $N_f^2/4$ for surfaces, where $N_f \sim 2\pi L/\lambda_u$ and $2\pi k_u a = 2\pi C/\lambda_u$.

The wire and surface computation times for obtaining transient results from a time-domain calculation are then

$$T_{tw} \sim \begin{cases} 4\pi N_f^4 A_{tw} \\ \\ 2N_f^3 A_{tw} \end{cases} + 4\pi N_f^3 B_{tw} \qquad (26a)$$

$$T_{ts} \sim \begin{cases} \frac{\pi}{4} N_f^6 A_{ts} \\ \\ \frac{N_f^5}{8} A_{ts} \end{cases} + \pi N_f^4 B_{ts} \qquad (26b)$$

where the upper part of each bracket refers to a monostatic, and the lower to a single source bistatic, calculation. In contrast to the case of the frequency-domain formulation, there is no difference in the time required to obtain the transient response of a structure, or to find its behavior at a single frequency, when following the time-domain approach. Note however, that in obtaining the structural response at a single frequency, one would choose N_f for that frequency,

i.e., at the maximum useable frequency of the calculation.

It is interesting to tabulate the highest order terms in L/λ and C/λ contained in the computer time expressions just derived. If we consider both single frequency and transient calculations for both the single source bistatic and monostatic cases we obtain the results shown in Table 1. There we observe that by considering only highest order terms in the computer time equations and by further ignoring the coefficients which multiply them, we find that the time-domain formulation evidently requires equal or less computer time than the frequency-domain approach for all but the monochromatic, monostatic, wire case. That this is not the case for problems of practical interest is shown in following section where the actual computer time estimates are presented. Furthermore, the misleading nature of computer time comparisons performed in this way is demonstrated.

c. Comparison of Computation Times

The general expressions developed above for the computer time requirements of the frequency- and time-domain formulations allow us now to obtain specific numerical comparisons of their relative computation times for typical problems. These expressions have been developed for the two most often encountered cases of practical interest, (1) monostatic scattering and (2) single-source bistatic radiation (or scattering). It is of interest here to compare the computer times associated with the analysis of these two cases using either the time- or frequency-domain approaches.

It is convenient to first rewrite Eqs. (24) and (25) in terms of L/λ or $ka = C/\lambda$ with C the enclosing sphere circumference, and also to use the numerical values of A, . . ., D. We obtain

$$T_{fw} \sim 3 \times 10^{-1}(L/\lambda)^3 + \left\{ \begin{array}{c} 5 \times 10^{-2}(L/\lambda)^4 \\ \\ 2 \times 10^{-3}(L/\lambda)^4 \end{array} \right\}$$

$$T_{fs} \sim 6 \times 10^{-2}(C/\lambda)^4 + 4 \times 10^{-1}(C/\lambda)^5$$

$$+ \begin{Bmatrix} 8\times10^{-2}(C/\lambda)^6 \\ 0 \end{Bmatrix} + 4\times10^{-3}(C/\lambda)^7 \qquad (27)$$

$$T_{tw} \sim \begin{Bmatrix} 6\times10^{-2}(L/\lambda)^3 + 2\times10^{0}(L/\lambda)^4 \\ 8\times10^{-2}(L/\lambda)^3 + 0 \end{Bmatrix}$$

$$T_{ts} \sim 5\times10^{-1}(C/\lambda)^4 + \begin{Bmatrix} 2\times10^{1}(C/\lambda)^6 \\ 5\times10^{-1}(C/\lambda)^5 \end{Bmatrix} \qquad (28)$$

For the single frequency cases we also have

$$t_{fw} \sim 1 \times 10^{-1}(L/\lambda)^2 + \begin{Bmatrix} 3 \times 10^{-2}(L/\lambda)^3 \\ 1 \times 10^{-3}(L/\lambda)^3 \end{Bmatrix}$$

$$t_{fs} \sim 4 \times 10^{-2}(C/\lambda)^3 + 3 \times 10^{-2}(C/\lambda)^4$$

$$+ \begin{Bmatrix} 8 \times 10^{-2}(C/\lambda)^5 \\ 0 \end{Bmatrix} + 5 \times 10^{-3}(C/\lambda)^6 .$$

Let us define the ratio of the time-domain to frequency-domain computer time as $R_{t/f}$. Using Eqs. (27) and (28), with the superscripts m,b to denote the monostatic and bistatic cases respectively, we find the following expressions for $R_{t/f}$:

$$R_{t/f}^{m,w} \sim \frac{6 \times 10^{-2} + 2L/\lambda}{3 \times 10^{-1} + 5 \times 10^{-2}\ L/\lambda} \qquad (29a)$$

$$R_{t/f}^{b,w} \sim \frac{8 \times 10^{-2}}{3 \times 10^{-1} + 2 \times 10^{-3}\ L/\lambda} \qquad (29b)$$

$$R_{t/f}^{m,s} \sim \frac{5 \times 10^{-1} + 2 \times 10^{1} (C/\lambda)^2}{6 \times 10^{-2} + 4 \times 10^{-2} C/\lambda + 8 \times 10^{-2} (C/\lambda)^2 + 4 \times 10^{-3} (C/\lambda)^3} \quad (29c)$$

$$R_{t/f}^{b,s} \sim \frac{5 \times 10^{-1} + 5 \times 10^{-1} C/\lambda}{6 \times 10^{-2} + 4 \times 10^{-2} C/\lambda + 4 \times 10^{-3} (C/\lambda)^3} \quad (29d)$$

The bistatic calculations can apparently be done more efficiently in the time-domain in terms of the order of L/λ or C/λ, but monostatic results require less computer time in the frequency-domain. Graphs of the computer times from Eqs. (24) and (25) and the time-domain, frequency-domain ratios are included in Figs. 73 through 76 for easy comparison.

It sould be noted that the numerical comparison of these calculation times is both computer and algorithm dependent. These results, particularly the absolute calculation times, can be expected to differ for other computers and may also be substantially changed if the algorithms were to be optimized. The expressions given by Eqs. (23) and (25) are, however, completely general and are thus more universally indicative of the computer time requirements for the frequency- and time-domain formulations.

Computer Storage Requirements

Besides the different computer times involved in generating the same numerical results in the frequency- and time-domains, there is also the computer storage requirement to be considered. The time-domain approach offers some potential savings in this area because of time causality, the phenomenon which also makes possible the time-stepping solution of the time dependent integral equation. As shown below, the savings effected depends upon whether the structure is of the wire or surface type.

If N is the number of current samples used, then in the frequency-domain, on the order of $2N^2$ real numbers must be computed and stored for impedance (or admittance) matrix. The number of real currents which are computed in the time-domain is $N N_T$ for N_T time steps. Of this total, however, only those which contribute to the fields over the structure at the present observation time need be considered.

Let d be the diameter of the smallest sphere in which the structure

can be enclosed. If Δt is the time interval used in the calculation, then the maximum number (N_m) of current values which can interact in any time step is

$$N_m \sim Nd/c\Delta t.$$

Since

$$c\Delta t \sim \Delta RS/2,$$

we obtain

$$N_m \sim Nd2/S\Delta R.$$

For a wire object of total length L, we have

$$L/\Delta x = N \geq d/\Delta R.$$

In this case

$$N_m \leq N^2\, 2/S.$$

The ratio of computer storage required in the time-domain compared with the frequency-domain, $S_{t/f}$, is for wire structures thus given by

$$S_{t/f} = N_m/2N^2 \leq 1/S.$$

A storage saving of 1/6 to 1/20 is then achievable at a minimum for wire structures, at the expense of a moderate increase in the program's complexity.

In the case of a surface structure of area A, we have

$$2A/\Delta R^2 = N \approx 2\pi d^2/\Delta R^2,$$

since A can exceed or be less than the surface area of the enclosing sphere. Then N_m becomes

$$N_m \approx 2N^{3/2}/\sqrt{2\pi}S.$$

The time-domain to frequency-domain storage ratio for the surface case is then

$$S_{t/f} \approx 1/\sqrt{2\pi N}\ S.$$

The potential time-domain storage savings is thus much greater than for the wire structure. As an example, if N = 200, (a reasonable number for a roughly spherical scatterer one wavelength in diam) then $S_{t/f} \sim 1/35$ (using S = 1). Looked at another way, the total storage required is decreased from

80,000 words to only 2,300 words or so, a substantial reduction.

Representation Complexity

One of the factors which deserves consideration when comparing the time- and frequency-domain approaches to a given problem is identification of the most suitable format for expressing the calculated response and the relative ease with which the parameters that characterize it may be obtained. The response of a highly resonant structure, for example the crown scatterer previously discussed, may be adequately described over a wide frequency range by using only its resonant frequency and the "Q" of the resonance peak. A digital (as opposed to analog) representation of such a response could be accomplished with just a few non-zero samples in the frequency-domain. The corresponding time-domain description, on the other hand, could require a greater number (an order of magnitude or more) of samples to accomplish the same thing. On a numerical basis then, in contrast to an analytical description, there may be a marked advantage of one domain over the other in terms of the amount of information required to qualify a given response.

It is pertinent to ask whether a significant benefit may accrue to one domain over the other on the purely numerical basis of obtaining a computer solution. Again consider the crown scatterer as an example. It can be verified from Fig. 65 that after a time of approximately P/c, with P the cylinder circumference, the backscattered field decays as a damped sinusoid at the scatterer's resonance frequency. On the order of only $\simeq 3\ P/c\Delta t$ time steps are required to carry the solution to the point where the resonance frequency and decay rate can be determined.

Beyond that point we can extrapolate the damped sinusoid behavior with reasonable assurance because this is a property characteristic of physical systems. On the other hand a frequency-domain calculation to locate the resonance and determine its Q may require may more samples over the bandwidth effectively covered by the time-domain calculation. The computation time advantage of the time-domain for this kind of problem would then become even more pronounced.

What about the case where the frequency variation of the structural

response resembles a damped sinusoid over the band of interest? If we could be absolutely sure of the entire frequency behavior from a limited sample of its response, it would be possible to extrapolate the remaining frequency variation in the same fashion as for the time response considered above. The extrapolation cannot be this confidently performed, however, since there is no obvious physical reason to expect the un-calculated response to exhibit a continued damped oscillatory behavior. This is in contrast to the time-domain case. The frequency-domain approach thus cannot exploit our general knowledge of a physical system's response in the same way as is possible in the time-domain. Broadly speaking, it appears reasonable to conclude that the time-domain offers a more dependable medium for shortening the calculation time without loss of significant information. However, loss in the accuracy of the low level frequency response away from the resonance can result from such a time-domain extrapolation.

V. EXTENSIONS AND POTENTIALS OF TIME-DOMAIN METHODS

The examples presented in the section on Integral Equation Techniques demonstrate the state-of-the-art in electromagnetic time-domain numerical capabilities. In addition, the potential advantage of time-domain over frequency-domain techniques for certain classes of problems, notably those involving limited source variation characteristic of antenna analysis or radar cross-section calculation for a small number of viewing angles was discussed in the previous section. It appears worthwhile to ask if further significant developments such as extending the structure complexity, widening the bandwidth, or increasing the efficiency of the numerical calculation may be possible. Furthermore, some thought should be devoted to identifying practical applications where time-domain techniques may offer analytical capabilities not available via the frequency-domain, i.e., non-linear effects. These topics are considered in order below.

Structural Complexity

The problems thus far treated from the time-domain integral equation viewpoint are not trivally simple. The satellite-type structures for example, especially those with wire appendages, are reasonable complicated even in the context of a frequency-domain analysis. Similarly, the wire problems presented

above also demonstrate a capability for treating wire geometries of reasonably complex shape. There are, however, extensions to both problem areas which would allow treating an even wider variety of geometries having significant practical interest. Aside from the obvious advantage to be gained from increasing the bandwidth of the calculation, which is considered in the following section, certain developments relating to structure complexity are also immediately suggested.

a. Multiple Wire Junctions

The capability for handling multiple wire junctions, i.e., junctions of three or more wires, has been found to greatly increase the scope of applicability of frequency-domain computer analysis. A similar advantage would accrue to the time-domain approach if it could be modified to handle this case as well. Since the time-domain numerical solution procedure for the two-wire junction case is already considerably more complex than that for the multiple-junction frequency-domain approach, we might expect that its extension to handle multiple junctions will be no easy task. We can, however, draw upon our frequency-domain experience to gain some insight as to the general approach that might be taken.

The basic requirement of a valid frequency-domain multiple-junction treatment is that it satisfy conditions of current continuity at the junction. One method for realizing this is described by Gee et al.[35] A three term current expansion (constant sine and cosine) is used together with an interpolation procedure between the segments connected at the junction to approximate the required continuity conditions there. This interpolation technique is a straightforward extension of that used for the simpler two wire junction and has been found to increase the accuracy of the calculation relative to that obtained when a constant current basis (no interpolation) is used for the Pocklington integral equation. Inclusion of a similar interpolation method for treating multiple junctions in the time-domain merits investigation.

This interpolation approach would result in the expression of the current on a segment connected to a multiple junction in terms of the sampled current values on all the other segments at the junction.

We would thus find that Eq. (30) for the two-wire junction case would be formally modified to take the form

$$I_{ij}(s_i'', t_j'') = \sum_{\ell=-1}^{\ell=+1} \times \sum_{m=n}^{m=n+2} B_{ij}^{(\ell,m)} \left[I_{i+\ell,j+m} + \left(\sum_{\ell'=1}^{\ell'=w} I_{i'+\ell'+1,j+m} \right) \delta_{1\ell} \right], \qquad (30)$$

with w denoting the number of wires connected to segment i at its positive end, $B_{ij}^{(\ell,m)}$ as previously given, and all segment lengths assumed equal. Similar expressions would apply to all other segments connected to the multiple junctions.

Another approach to the multiple junction probelm may be provided by frequency-domain method employed by Chao and Strait.[36] Their treatment of this problem is to model wire junctions as combinations of L-shaped open-ended wires which overlap at the junction over an interval of two segments. This allows the multiple junction to be analyzed without the necessity for developing a special multiple junction formulation and computer program. A piecewise linear current expansion and Galerkin's method is used in their numerical reduction of the wire integral equation. If this approach could be employed for the time-domain solution, it would permit the present program to be applied to multiple junction problems with relatively little modification.

b. Hybrid Structures

Hybrid structures consisting of spheres and cylinders with straight wire appendages have been formulated for solution in the time-domain through use of a combination of surface and wire integral equations as

discussed above. The range of hybrid structures, which can be analyzed in the time-domain, could be significantly broadened by generalizing treatment to handle wire appendages of arbitrary shape. This might be most easily accomplished by combining the surface program developed by Bennett et al.[10] with the wire program described by Miller et al.[11] The wire treatment used by Bennett et al. is applicable to straight wires only.

c. Shell Geometries

Many structures of practical interest consist of thin shell-like geometries which can not be conveniently treated via existing wire or surface programs in either the frequency or the time-domain.

Aircraft for example, have relatively thin wing and tail surfaces which are not well suited for treatment using a surface integral equation because the close proximity of the opposite sides tends to produce ill-conditioned matrices. While wire grids may sometimes provide a tractable numerical model for this geometry, they are known to lead to a generally less efficient numerical treatment of surfaces than a surface integral equation.

The development of special integral equation techniques for the time- and frequency-domain analysis of shell-like geometries would greatly extend the range of problems amenable to numerical modeling. Effort directed in this area is certianly indicated since a requirement for this capability arises frequently in electromagnetic anlaysis. The successful development of such techniques could add significantly to the state-of-the-art.

Wide Bandwidth Calculations

Extension of the bandwidth of the calculation is one of the most pressing needs in the further development of transient numerical techniques. The rapid growth in computer time requirement with increasing structure size in wavelengths demonstrated by Eqs. (24) and (25) underscores the impracticability of extending time-domain integral equation techniques very much beyond the resonance region. Many interesting transient problems, however, involve structures whose dimensions are large compared with the

shortest wavelengths producing a significant response. There is a need, consequently, to develop approaches, combining whatever techniques may be appropriate, for the transient evaluation of structures arbitrarily large relative to the shortest wavelength in the exciting source spectrum. Some methods which may have some application for increasing the calculation bandwidth are suggested below.

a. Integral Equation Extensions

There seem to be few possibilities by which the integral-equation approach can be modified to extend the high frequency cutoff of the time-domain calculation. Most of the techniques that come to mind involve combinations of the time-domain formulation with various high frequency, frequency-domain approximations (as discussed below). There is one approximation, however, that may have some potential for directly extending the bandwidth of the time-domain calculation.

It has been verified by frequency-domain results that points on a structure separated by a wavelength or more may not appreciably interact, and can thus be neglected in the computation of the impedance matrix. A similar approximation may possibly also be invoked for the time-domain calculation. In this case it would be the retarded time difference which would serve as the criterion for neglecting mutual interactions. This approximation would reduce the storage and computation time dependencies on the number of space samples from N^2 to N'^2 where N' is the reduced number of interacting current samples.

Adaptive time stepping should also allow the time-domain computation to be extended to a wider bandwidth. The early time response contains more high frequency information, and is thus more rapidly varying, than the latter time waveform. It is consequently necessary to sample the initial current values at time intervals appropriate to the highest frequency intended to be resolved. The late-time, low-frequency samples could be calculated at more widely separated times so that a longer time span could be covered with fewer current samples, and require a reduced computation time. It may be similarly possible to reduce the spatial sample density as the high frequency waveform decays to small amplitudes.

A practical method for conveniently achieving this may be via an iterative process whereby successive calculations which employ smaller space and time samples together with a narrower pulse are performed. Each computation will be truncated where its current agrees to within some specified amount of the previously calculated case. Only that part of the spectrum associated with the higher frequency incident pulse, and not the low frequency data, would be re-computed then.

b. Physical and Geometrical Optics

Any consideration of extended frequency calculations must inevitably include those proven frequency-domain techniques based upon physical and geometrical optics. The capability provided by the FFT for economically deriving transient behavior from the frequency response enables us to substitute such frequency-domain methods for direct time-domain solutions. It may furthermore develop that some problems can be formulated directly in a transient sense using such approximations, thus circumventing the need for their prior treatment in the frequency-domain and the attendant necessity for a Fourier Transform.

An in-depth discussion of this area is beyond the scope of this presentation. We can, however, briefly consider the problem involved in obtaining a transient response synthesized from combining the results of two or more, ideally overlapping, band-limited calculations performed in either the frequency- or time-domains. Suppose for example, that separate results are available for a structure that covers the ranges from essentially zero frequency to F_1 (response R_1 from a time-domain integral equation), from F_2 to F_3 (response R_2 from physical optics) and from F_4 to F_5 (response R_3 from geometrical optics). If $F_2 \leq F_1$ and $F_3 \leq F_4$, then a composite frequency response can be rather easily obtained; most simply by setting the overall response R equal to R_1 from 0 to F_1, R_2 from F_2 to F_3 and R_3 from F_4 to F_5, while averaging the responses in the regions of overlap. If it happens however that $F_2 > F_1$, then a more sophisticated interpolation procedure might be used to generate R. Note that from Parseval's Theorem the root mean square errors in the frequency- and time-domains are equal so that bounds on the transient response error may be derivable.

c. Moving Time-Space Window

It has been found practicable for some problems in the frequency-domain to decrease the computation time by neglecting interaction between current elements whose separation exceeds some minimum distance. This procedure can not only decrease the number of impedance matrix elements requiring calculation, but can under certain circumstances greatly facilitate the matrix inversion as well. A straight wire offers a particular example of a structure which can be effectiely treated using this approach.

Application of a similar method to the solution of the time-domain integral equation may offer similar advantages. Implementation of this idea in the time-domain is not likely to be as straightforward as for the frequency-domain calculation. What it might involve is a space window of the appropriate width traveling with the incident pulse (in the case of a scatterer) outside of which mutual interactions are neglected. The effect of this approximation on the calculation time would be to reduce the N^2 current sample term in Eq. (25). This reduction could be substantial if the number of current samples in the space window is significantly less than the total number of current samples on the structure. A potential problem of methods like this is the difficulty of their adaption to a workable computer program and their tendency to become too problem oriented, losing as a result the desirable quality of flexibility of application.

Increased Efficiency

The computer time requirements dicussed above for numerical solution of the time-domain integral equation are not only computer, but algorithm dependent. It may be possible, consequently, to significantly reduce the indicated times by optimizing the programs. Whatever is feasible in this regard is not likely alone to greatly extend the upper frequency cutoff F of the time-domain calculation because of the high order polynomial dependence of the computer time on F. There may be other methods for increasing the computational efficiency, which taken altogether could measurably increase the applicability of transient techniques for certain problems.

One obvious way of decreasing computer time (and storage) is the exploitation of structural symmetry. Many objects of interst are mirror or rotationally symmetric. The latter property offers a particularly advantageous method for increasing either the size, or decreasing the expense, of treating surface structures, since then area current sampling can be replaced by linear sampling instead. This has the effect of reducing the order of the C/λ terms in Eq. (28) to something similar to those in the wire structure equation (27). Advantage can be taken of symmetry, even when the entire structure is not symmetric, by augmented matrix or partitioning methods similar to those found useful in such cases in the frequency-domain. A disadvantage of techniques like this is that their computer programming can become quite complex.

Another method by which calculation efficiency might be increase is the use of adaptive time stepping in obtaining a time-domain solution, or analogously, adaptive frequency stepping for frequency-domain solutions. The early time response of a structure will generally have more influence on its high frequency behavior than will the latter part of the time waveform. Consequently, it may be possible to use shorter time steps initally, and then to increase their size as the high frequency response decays, leaving the lower frequencies to dominate the time behavior. The actual time step used and the criteria for determining when it should be changed could be based on a polynomial extrapolation of past time results to the present time step for comparison with the actual calculated values. Similar methods have been used in predictor-corrector differential equation solver routines.[37] Time-step size changes have been utilized by Bennett and Weeks[8] in the solution of two-dimensional time-domain problems.

Adaptive frequency stepping for frequency-somain solutions should allow the response of a resonant structure such as the crown band (Fig. 65) to be more efficiently obtained. Rather than calculate the scattered field at an evenly spaced sequence of points, the calculations would instead be performed where the response is most rapidly changing, in this case the resonance peak. In some cases, a similar principle applied to numerical quadrature has been found to reduce the integration time of peaked functions by orders of magnitude.[38]

Selection of more suitable time interpolation functions may also help reduce the computation time in the time-domain. If instead of using a polynomial basis function for the induced current's time variation, one were to use a sinusoidal function having a frequency equal to the lowest resonance frequency of the structure, the current could be more accurately matched and thus require fewer samples per unit time. Balanced against this potential advantage would be the possible increase in computational complexity due to the new basis function. Terms harmonic to the lowest resonance might also be used in the current expansion. Richmond[6] has investigated similar questions in the frequency-domain.

Truncation of the time-domain calculation might be made possible earlier in the calculation by computing the frequency response of the structure on the basis of the information obtained to the present time step together with its extrapolation to future time. If this operation were repeated at suitable time intervals, the convergence of the frequency variation could be readily determined. When two successive frequency responses are found to agree within some convergence criterion, the time-domain calculation could be stopped with a reasonable degree of confidence in the computed data. Coupled with this might also be the utilization of a more sophisticated time extrapolation function, i.e., one which allows for a multi-harmonic waveform.

Applications

There are various reasons why electromagnetic problems may be advantageously viewed on a transient basis. Object identification is one area for which knowledge of the short pulse or transient response of a target is desirable. The resulting increase in bandwidth improves the possibility for discriminating between targets. Must of the motivation for the early work by Bennett and his colleagues originated from this application.

Another area of interest, which stems from object identification, is the need for antenna designs which radiate short pulse waveforms of specified shapes. This requirement leads to the concept of antenna "fidelity" as discussed by Susman and Lamensdorf.[39] The antenna in this case becomes one part of a pulse shaping and processing network, the overall response of which is needed to determine the input pulse shape

which will produce a desired radiated pulse, or to derive the incident pulse shape from the antenna circuit response.

The nuclear electromagnetic pulse (EMP), which is produced when a nuclear device is detonated under the appropriate conditions, requires an understanding of the short pulse response of systems such as rockets, communications networks missile installations, etc. if they are to be adequately protected against possible EMP damage. The short rise time (~ 10 nanoseconds) and large peak field strengths (~ 50,000 V/m) which characterize the EMP can cause extremely complicated responses from systems it illuninates. The intractability to analysis or computer modeling of this problem has led to the development of EMP simulators which provide an experimental avenue for determining system response and consequent possible hardening requirements. Simulator design also leads to the necessity for finding the short pulse response of candidate designs, which, while typically simpler to analyze than the systems to be tested, still pose a challenging problem in transient electromagnetics to the analyst. Furthermore, while the system problems are indeed difficult, some progress towards their understanding can be realized by performing transient studies of simpler related problems.

An area particularly suited to a time-domain treatment is non-linear analysis. There has developed in recent years an interest in the active loading of both antennas and scatterers. The former is of concern since active impedance loads evidently have some potential for achieving significant size reduction of antennas. The use of active impedance loads for scatterers has been studied from the viewpoint of radar cross-section reduction and masking. In both applications, a capability for realistically evaluating the effects of active, and thus generally non-linear, loads would facilitate their exploitation in antenna and scatter design. While it may be feasible to perform some non-linear analysis in the frequency-domain, the time-domain can be expected to provide a more tractable medium for such studies.

VI. TIME-DOMAIN TECHNIQUES IN PERSPECTIVE

We have attempted in this presentation to place the time-domain approach in perspective relative to the more commonly used frequency-domain formulation

of electromegnetic analysis for obtaining either transient or monochromatic information. Our main concern has been to document the state-of-the-art in time-domain computations, and to examine whether it is more than simply a novel, but not otherwise unique, method for solving Maxwell's Equations. While there is no doubt that the transient representation has a valuable role to play in electromagnetic theory, it is not so obvious that a time-domain approach is necessary for its derivation. Conventional frequency-domain analysis may suffice as well for obtaining transient solutions.

Except for the natural advantage provided by the time-domain for non-linear analysis, the time- and frequency-domains may be viewed as offering alternative and complimentary routes for obtaining and representing electromagnetic phenomena. Each domain has its own areas and applications where it may offer advantages over the other as to computer time and storage requirements and interpretation of physical behavior. This is true whether the information sought is for time- or frequency-domain application. Thus in some cases, transient analysis may be more economically realized using a frequency-domain formulation followed by a Fourier transform to the time-domain. This may be the case for example, when the single-source transient backscatter response of a surface structure is desired, as demonstrated in the above discussion. On the other hand, the wide-band frequency response of a wire structure to single source excitation may be more efficiently determined via a Fourier transform of the time-domain derived response.

The relative computational advantages of analysis in either of the two domains may change as improvements in numerical techniques and formulations are made. Thus, the comparisons made in this presentation are subject to revision as advances occur in electromagnetic computer modeling. It seems obvious, however, that transient electromagnetics will continue to draw upon both time- and frequency-domain analytic methods.

Extensions to handle larger structures, drawing upon the special features of both the time- and frequency-domain deserve further study. Improvements in computational efficiency such as the use of more sophisticated time waveform extrapolation, adaptive time stepping, and

symmetry exploitation would perhaps enhance the value of time-domain analysis. Also indicated is the need to develop analysis methods for modeling more complex structures. A particular requirement, which is associated with developing the latter capability, is the need for simplifying both the body geometry description for computer input as well as presentation in compact form of the computed electromagnetic characteristics. It is the large amount of information inherently possessed by the time-domain waveforms which makes the transient presentation so useful, and which makes time-domain analysis a truly valuable addition to electromagnetic theory.

VII. ACKNOWLEDGMENT

The author greatly appreciates the assistance provided by C. L. Bennett of the Sperry Rand Research Center in gathering and organizing the material presented here.

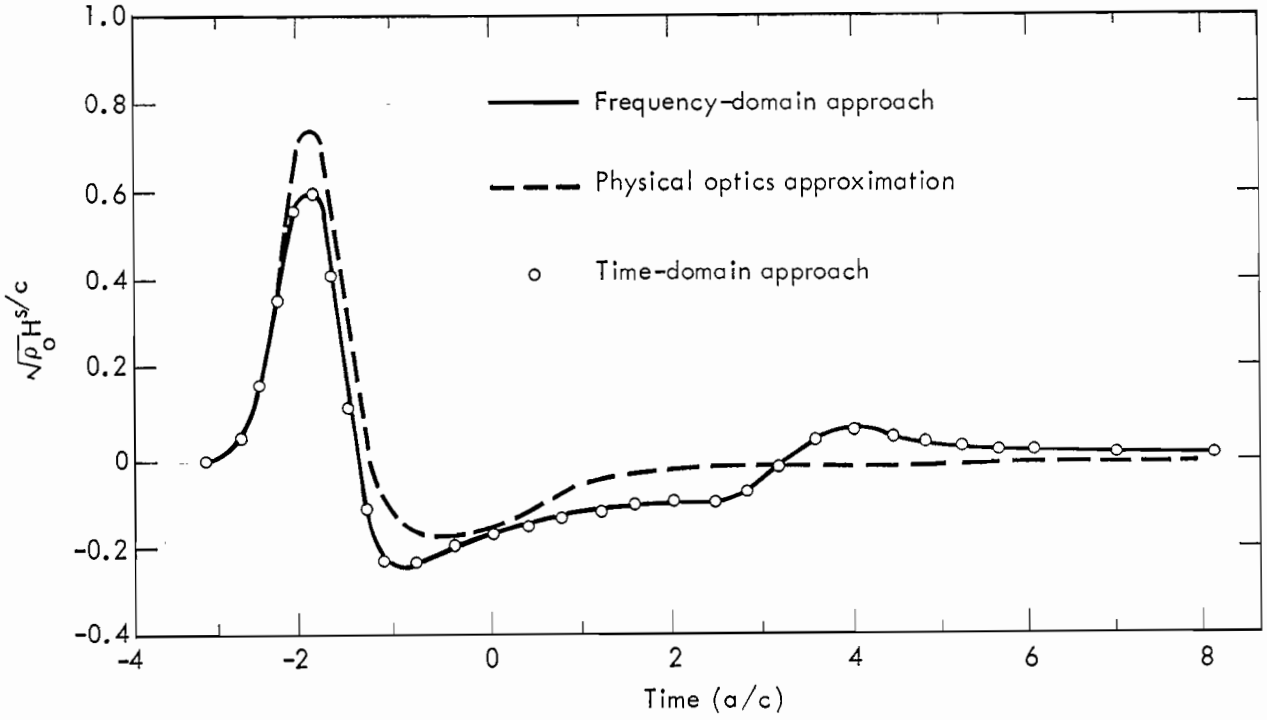

Fig. 1. Approximate transverse electric (TE) response of a circular cylinder in the backscatter direction (after Bennett and Weeks[8]).

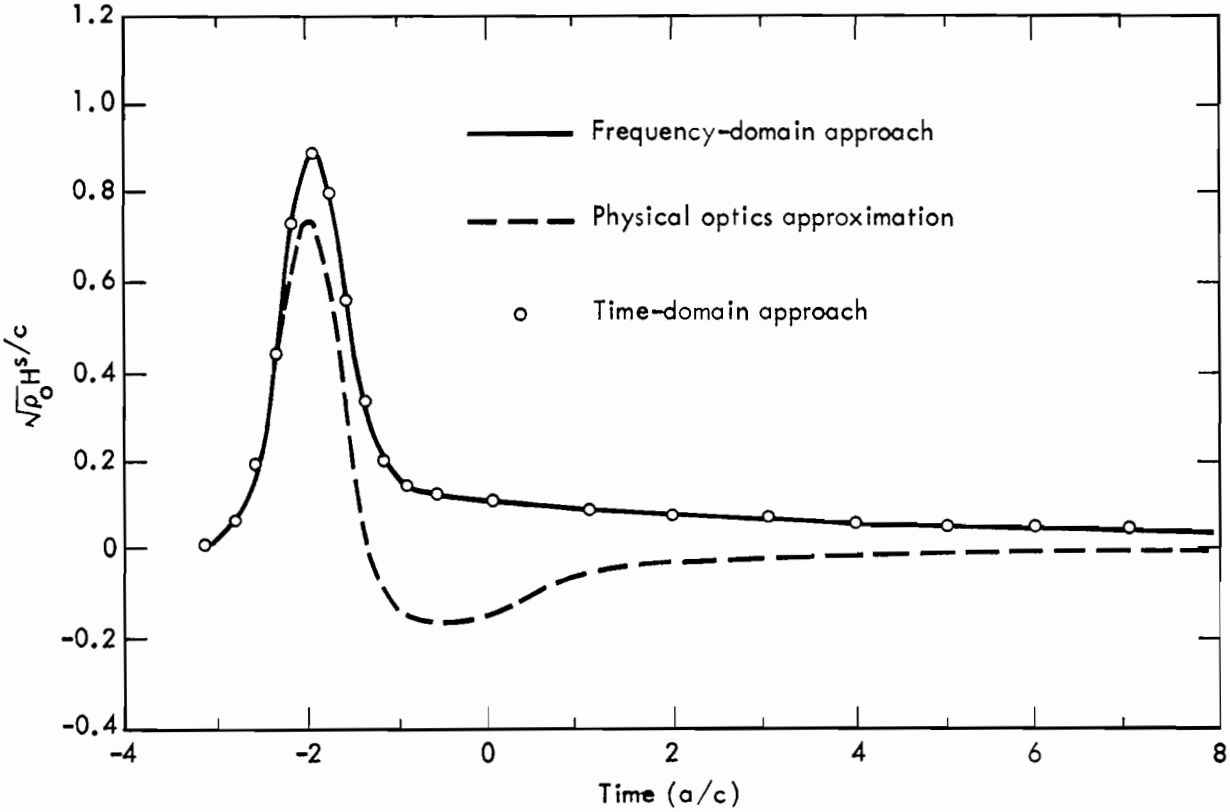

Fig. 2. Approximate transverse magnetic (TM) response of a circular cylinder in the backscatter direction (after Bennett and Weeks[8]).

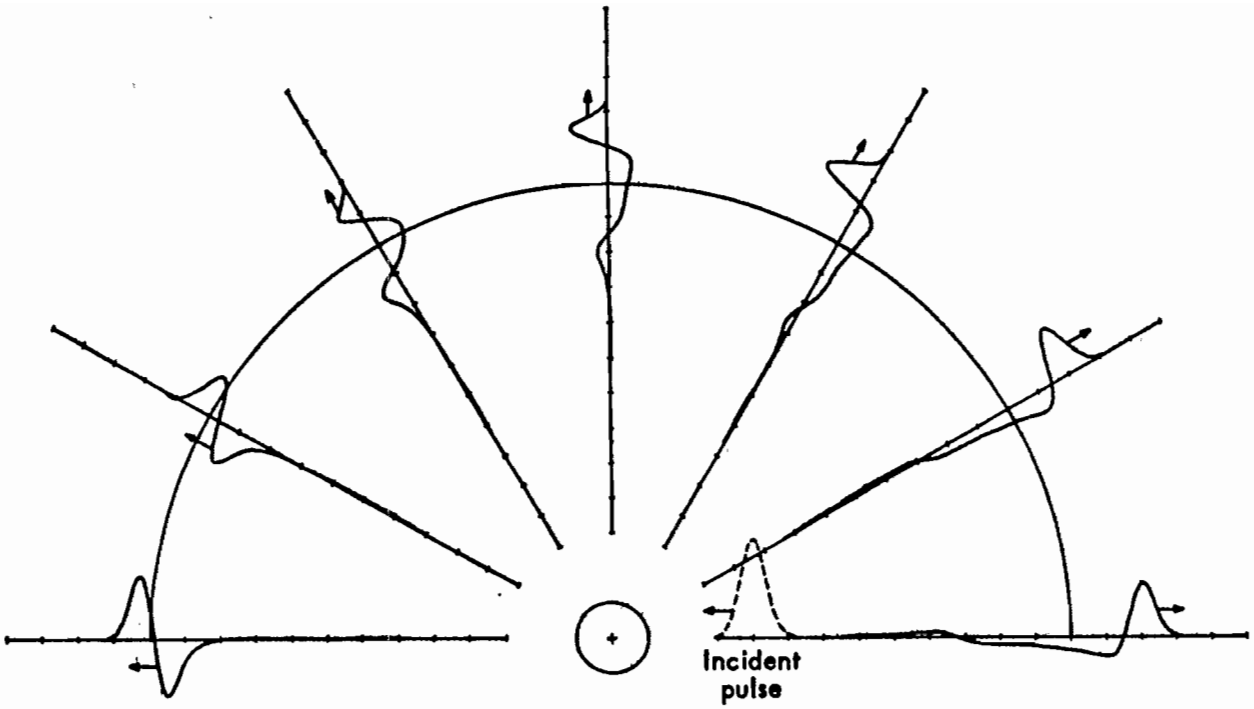

Fig. 3. Approximate TE impulse response of a circular cylinder (after Bennett and Weeks[8]).

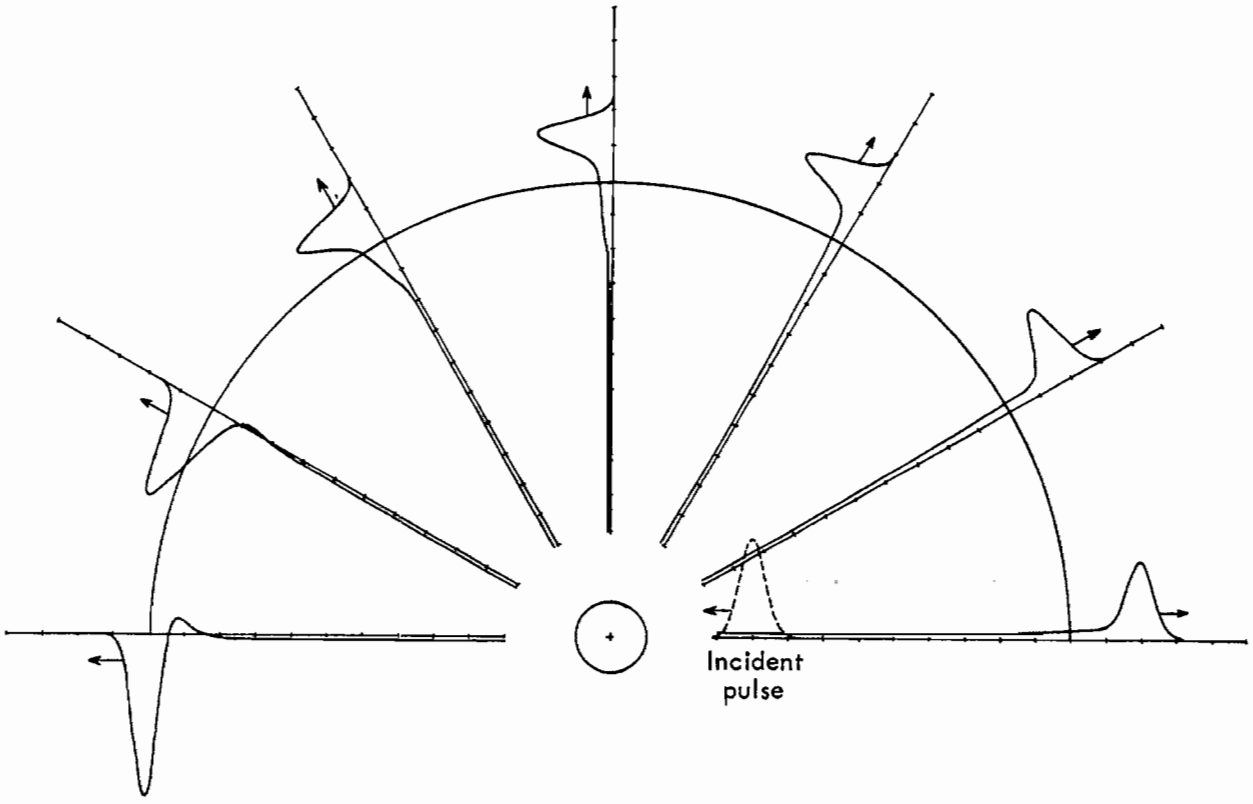

Fig. 4. Approximate TM impulse response of a circular cylinder (after Bennett and Weeks[8]).

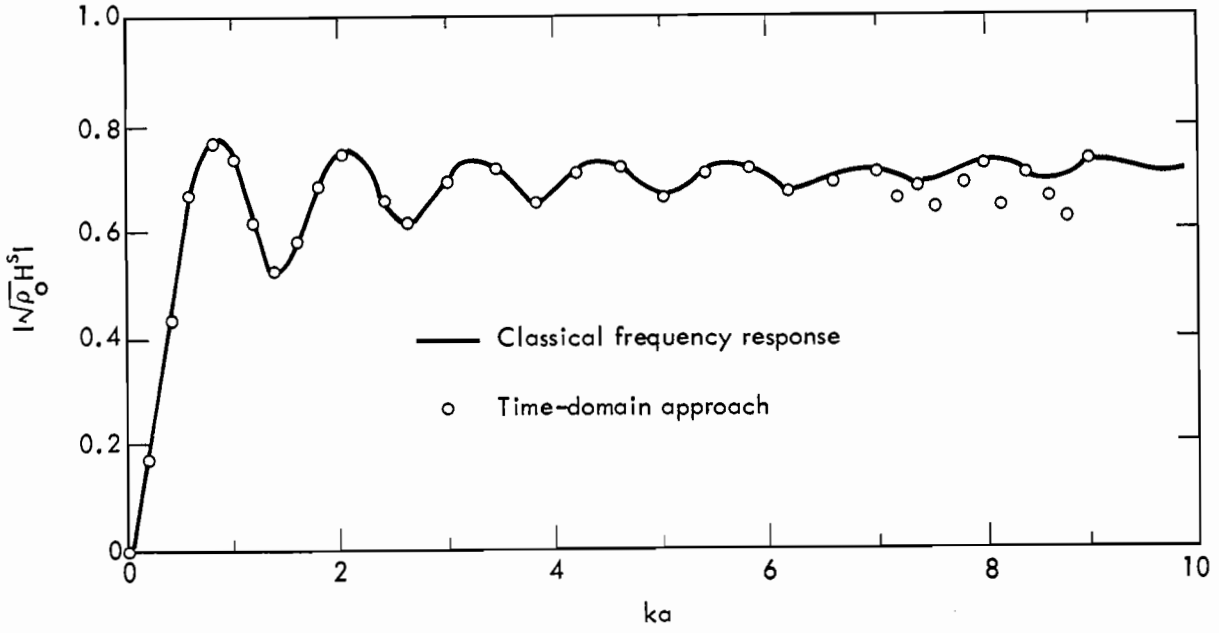

Fig. 5. Transverse electric frequency response in the backscatter direction of a circular cylinder of 1-m radius (after Bennett and Weeks[8]).

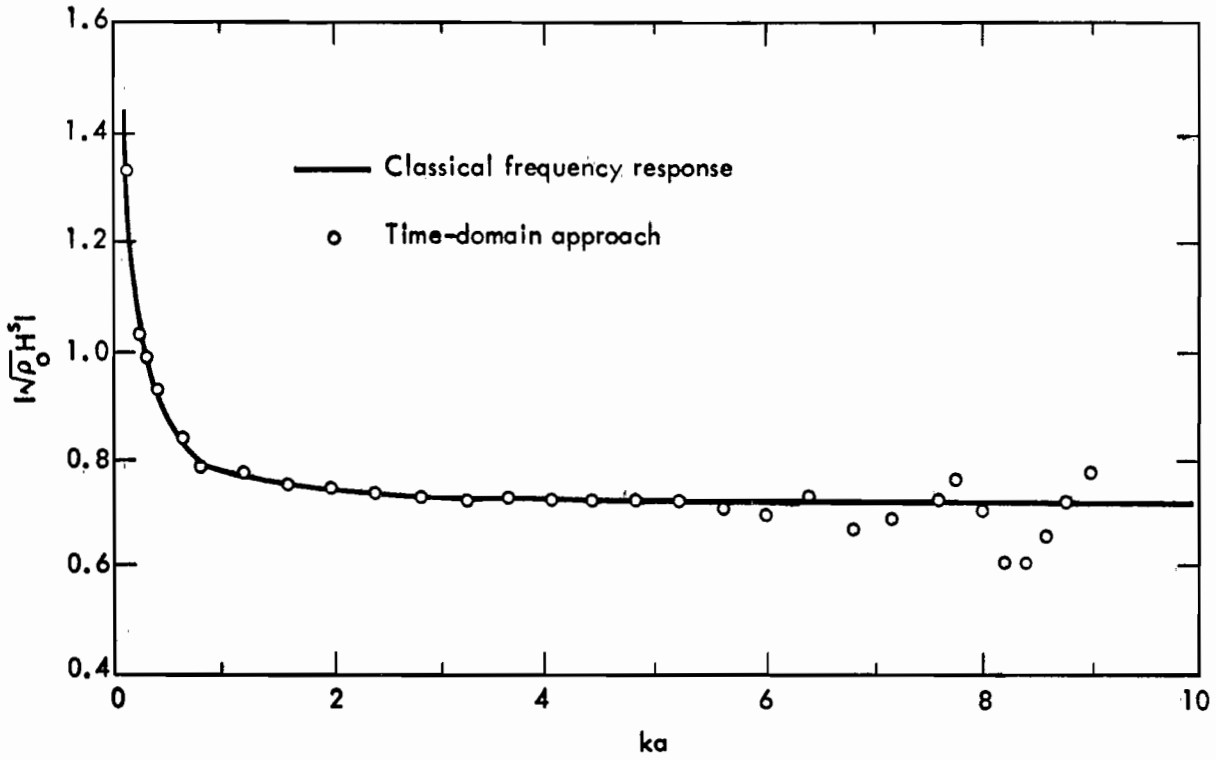

Fig.6. Transverse magnetic frequency response in the backscatter direction of a circular cylinder of 1-m radius (after Bennett and Weeks[8]).

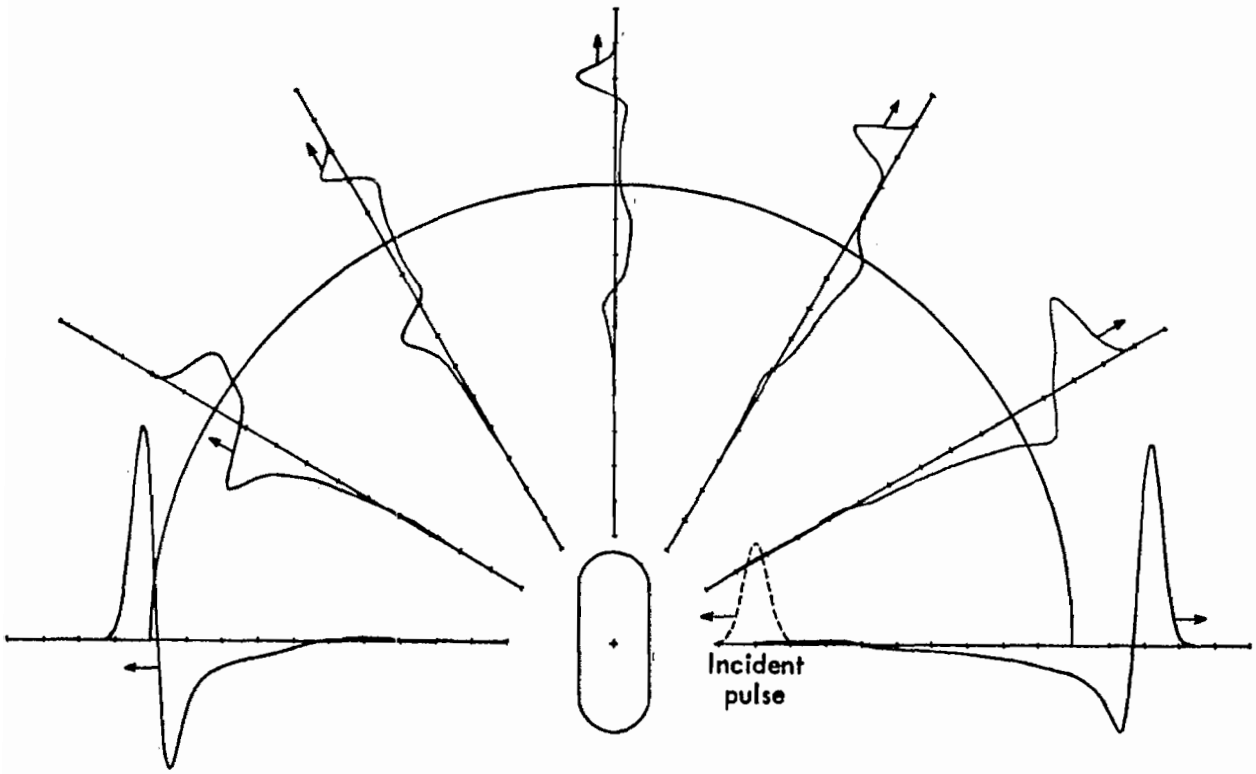

Fig. 7. Approximate TE impulse response of a strip with broadside incidence (after Bennett and Weeks[8]).

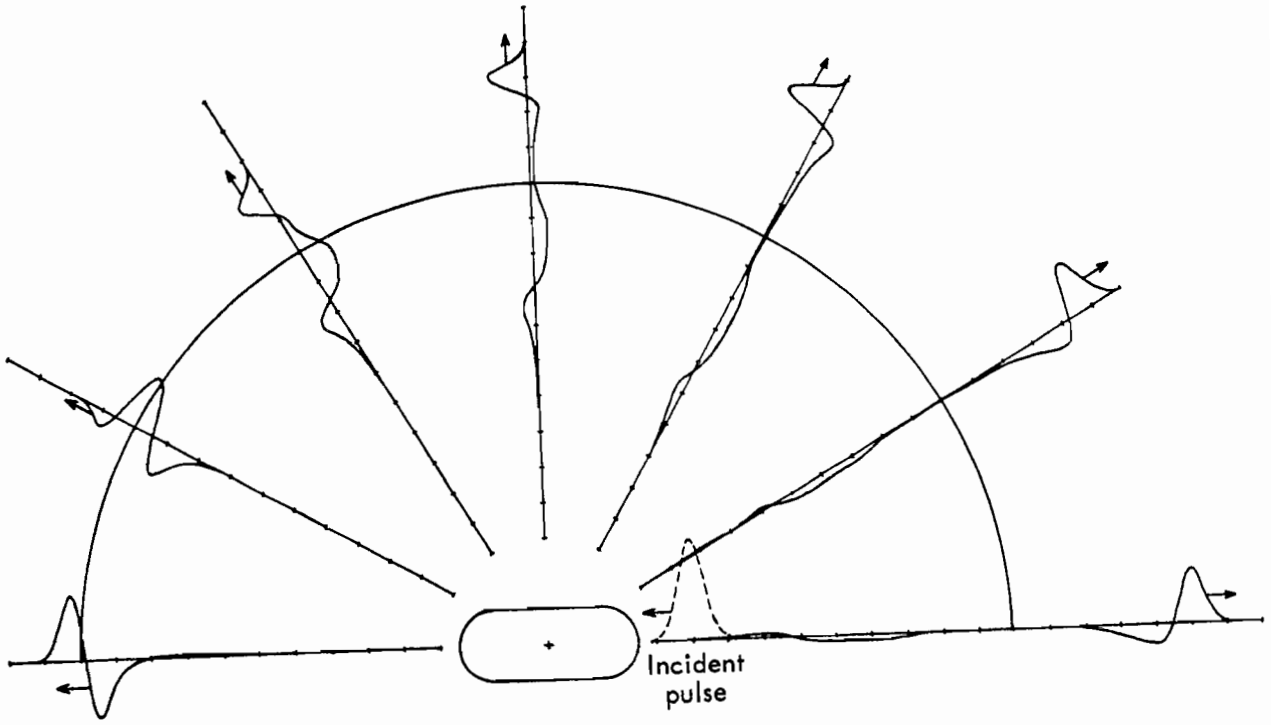

Fig. 8. Approximate TE impules response of a strip with end-on incidence (after Bennett and Weeks[8]).

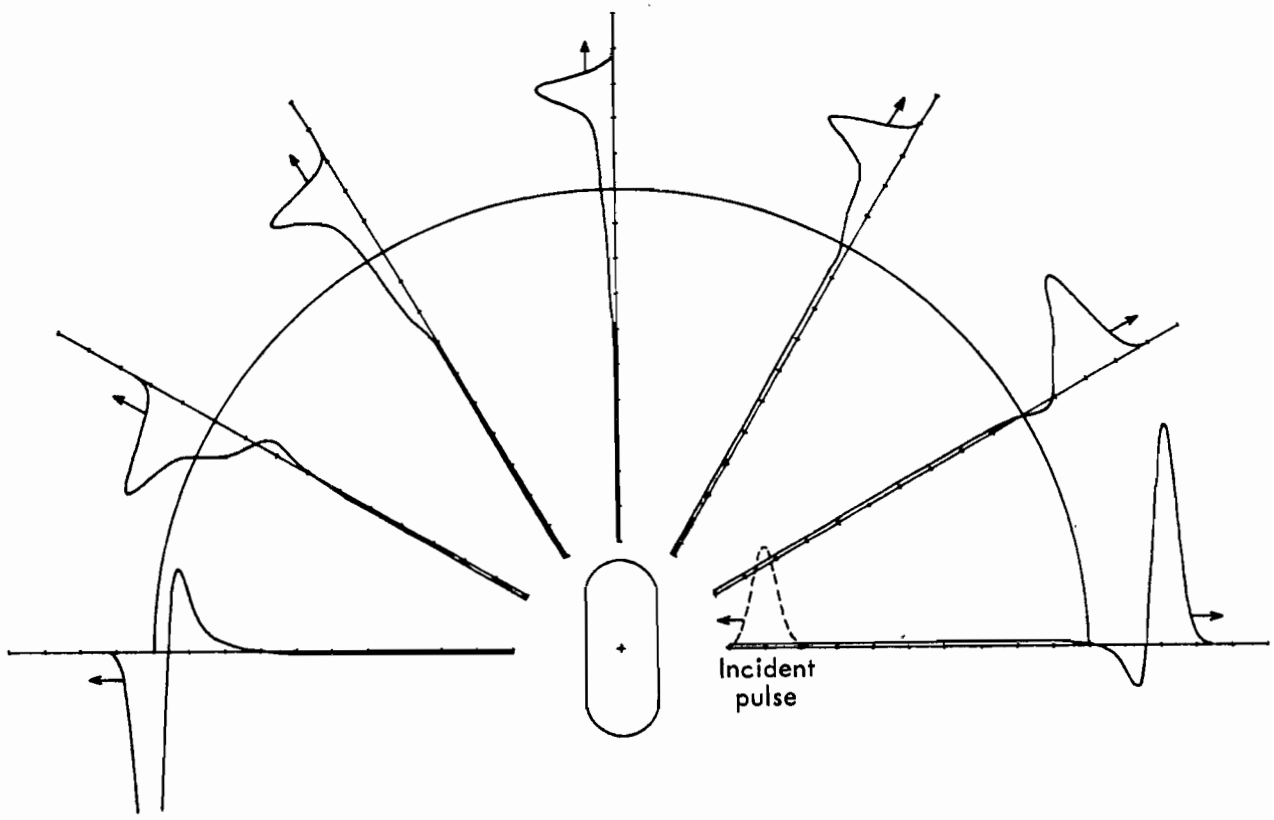

Fig. 9. Approximate TM impulse response of a strip with broadside incidence (after Bennett and Weeks[8]).

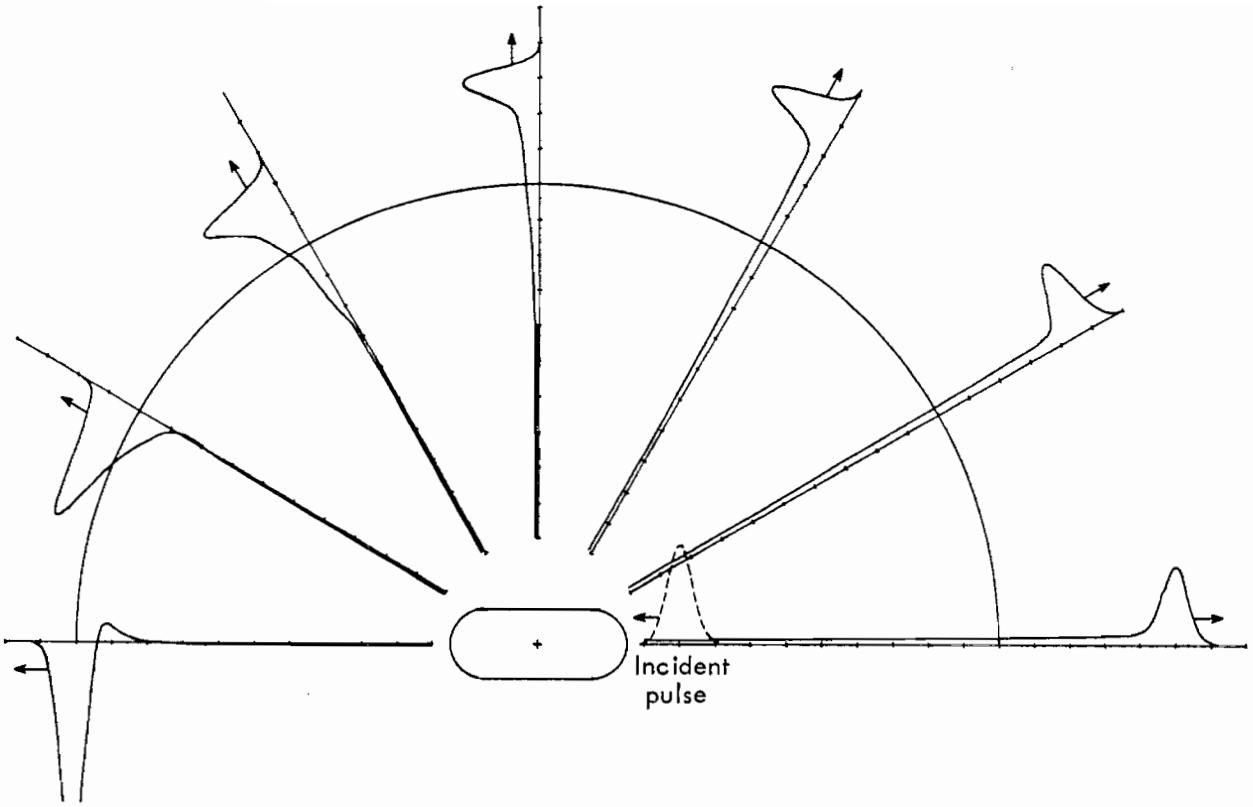

Fig. 10. Approximate TM impulse response of a strip with end-on incidence (after Bennett and Weeks[8]).

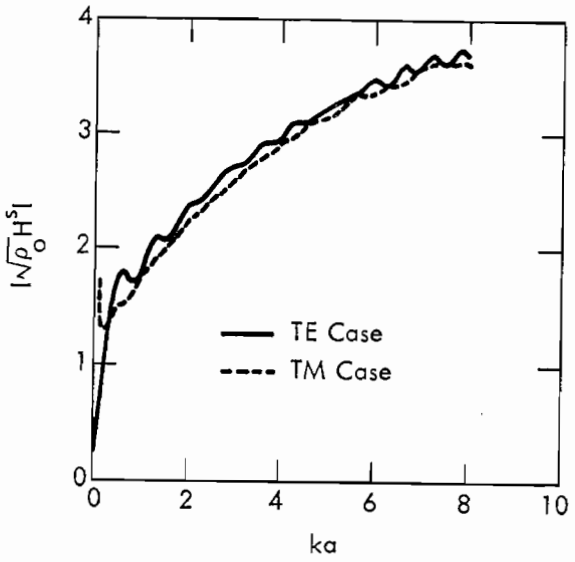

Fig. 11. Frequency response in the back-scatter direction of a strip with broadside incidence (after Bennett and Weeks[8]).

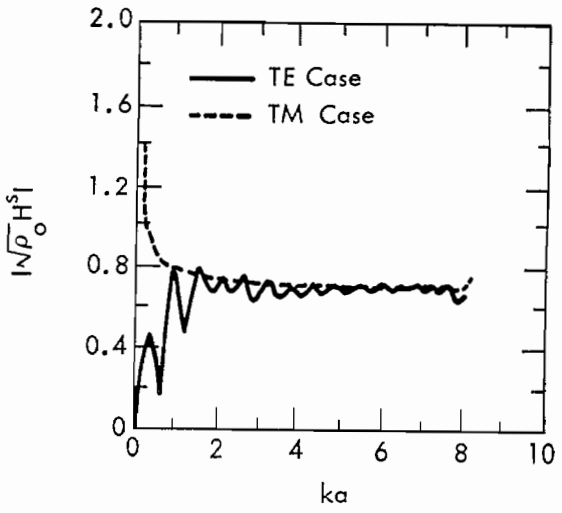

Fig. 12. Frequency response in the back-scatter direction of a strip with end on incidence (after Bennett and Weeks[8]).

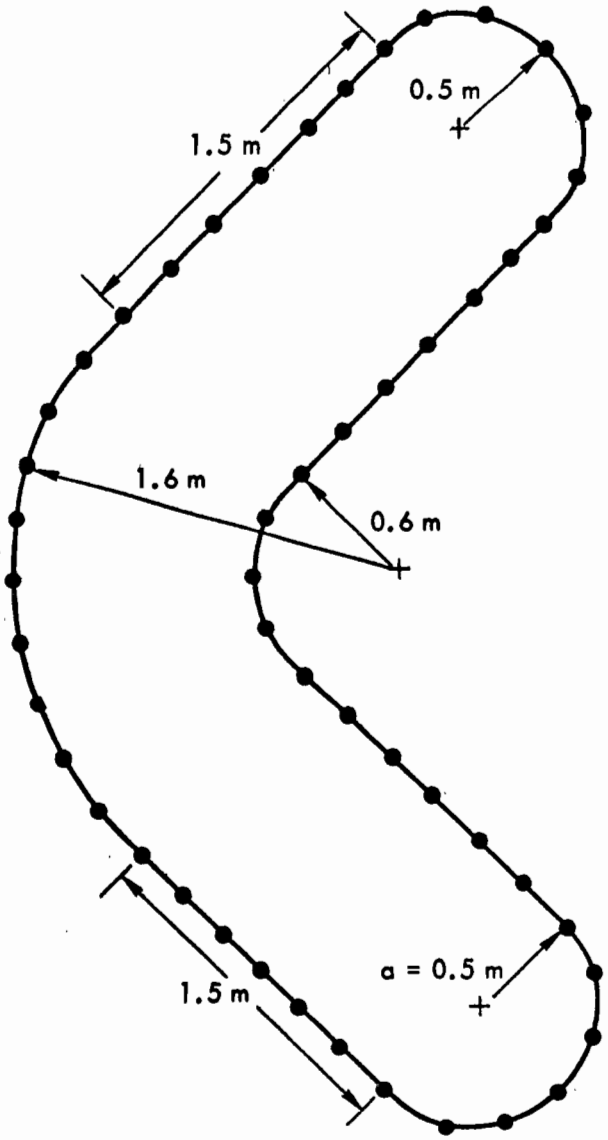

Fig. 13. Geometry of the corner reflector (after Bennett and Weeks[8]).

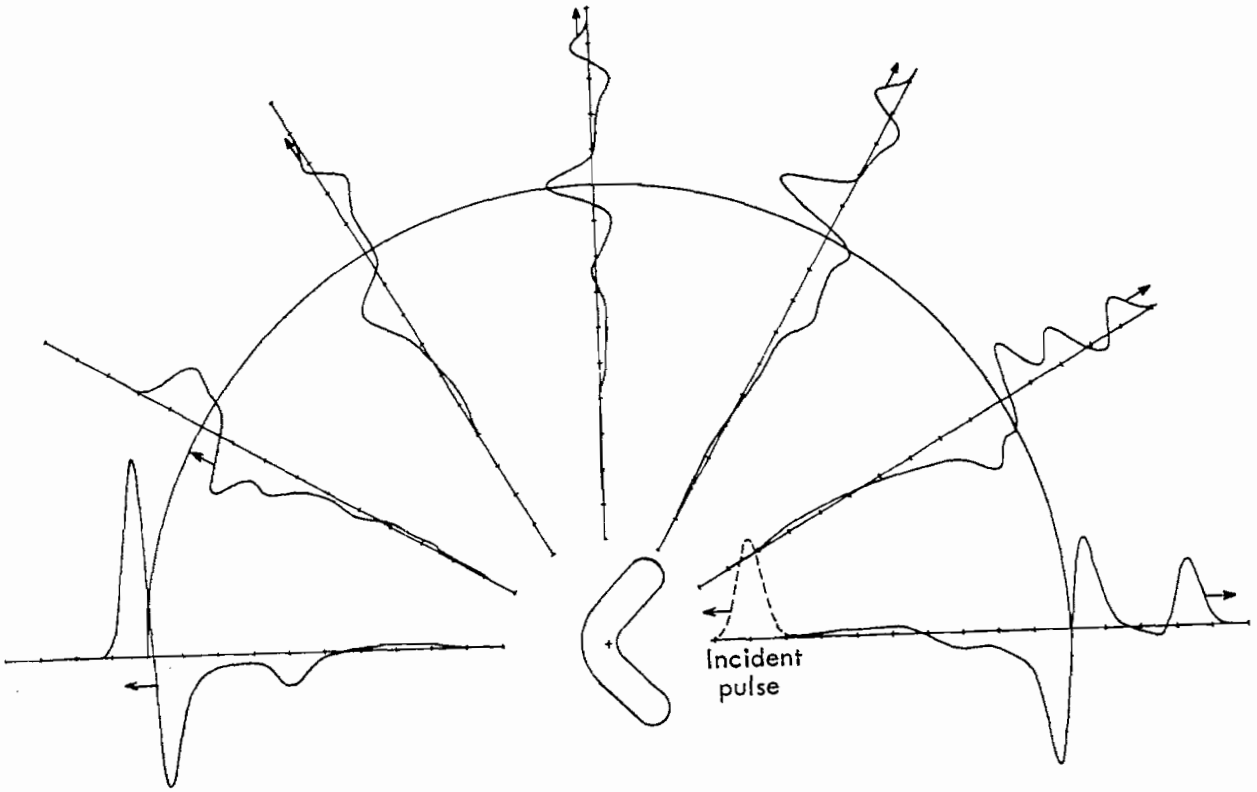

Fig. 14. Approximate TE impulse response of a corner reflector with frontside incidence (after Bennett and Weeks[8]).

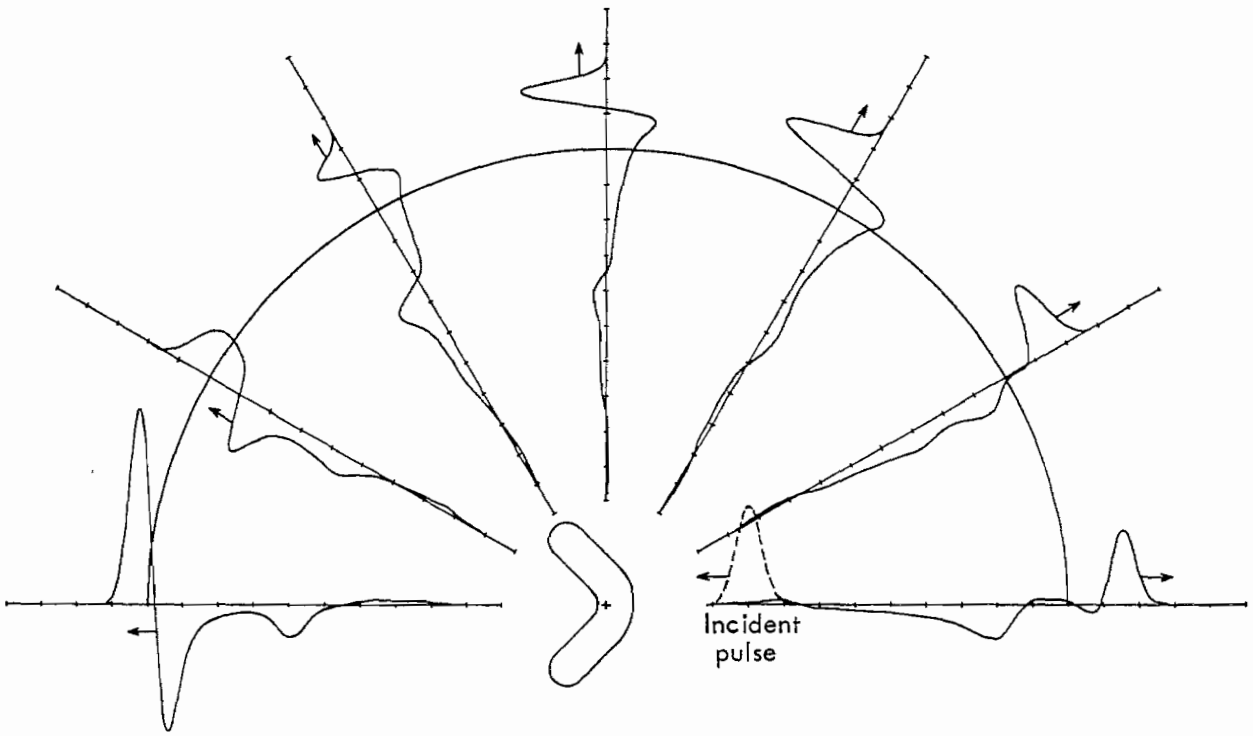

Fig. 15. Approximate TE impulse response of a corner reflector with backside incidence (after Bennett and Weeks[8]).

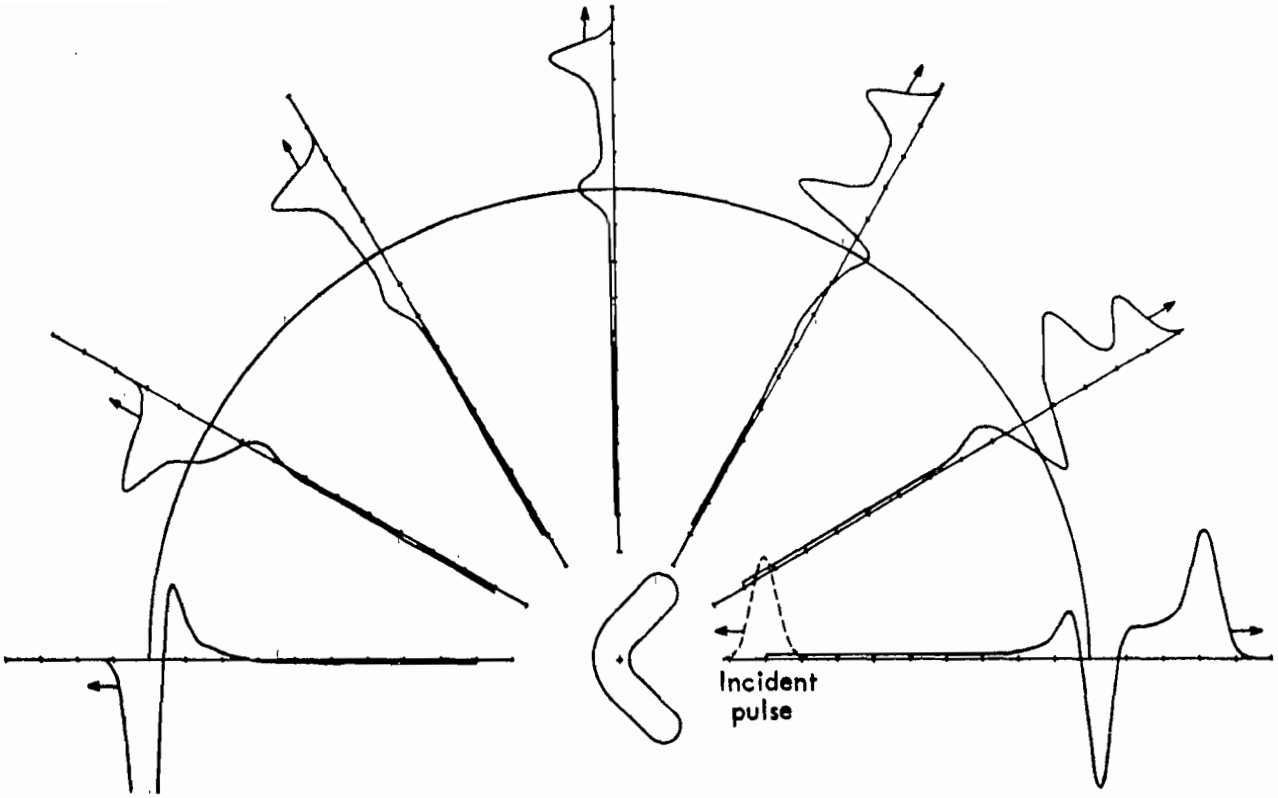

Fig. 16. Approximate TM impulse response of a corner reflector with frontside incidence (after Bennett and Weeks[8]).

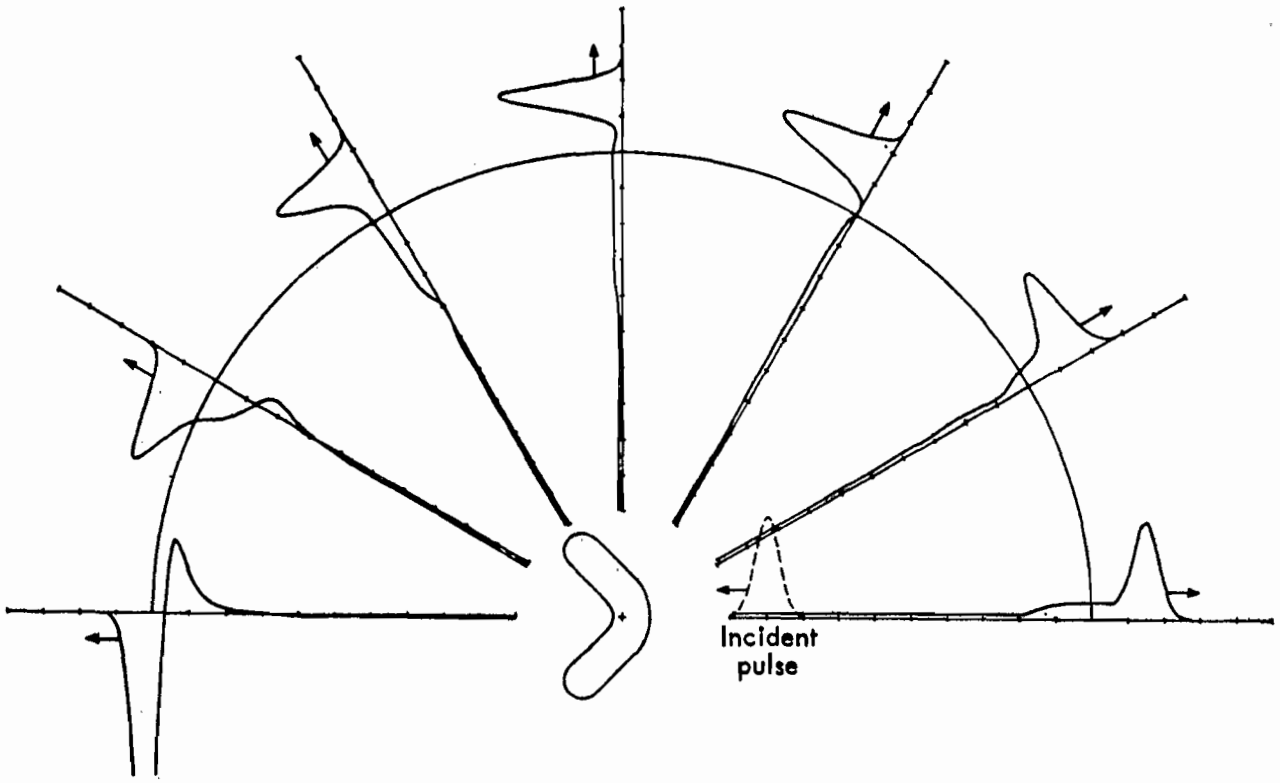

Fig. 17. Approximate TM impulse response of a corner reflector with backside incidence (after Bennett and Weeks[8]).

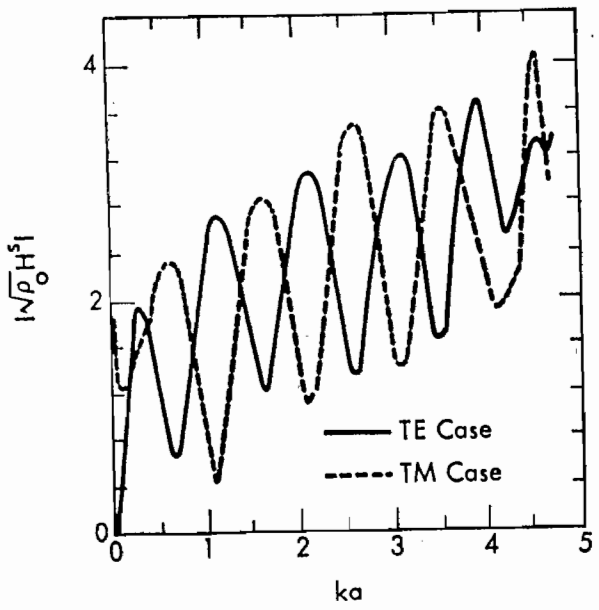

Fig. 18. Frequency response in the backscatter direction of a corner reflector with frontside incidence (after Bennett and Weeks[8]).

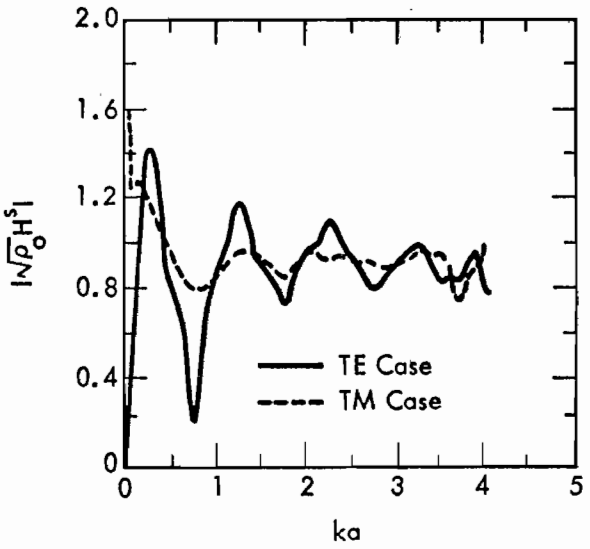

Fig. 19. Frequency response in the backscatter direction of a corner reflector with backside incidence (after Bennett and Weeks[8]).

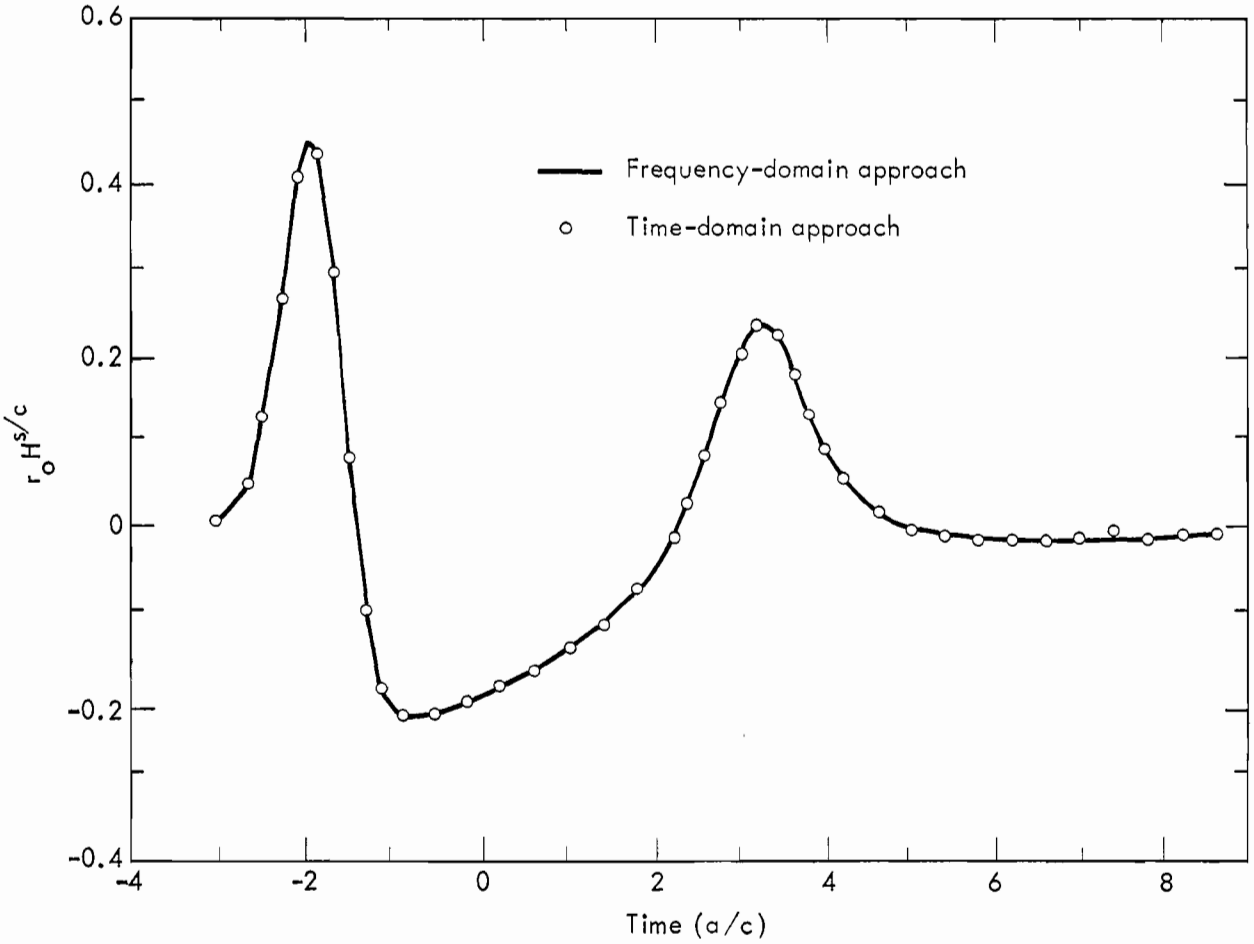

Fig. 20. Approximate impulse response of a sphere in the backscatter direction (after Bennett and Weeks[8]).

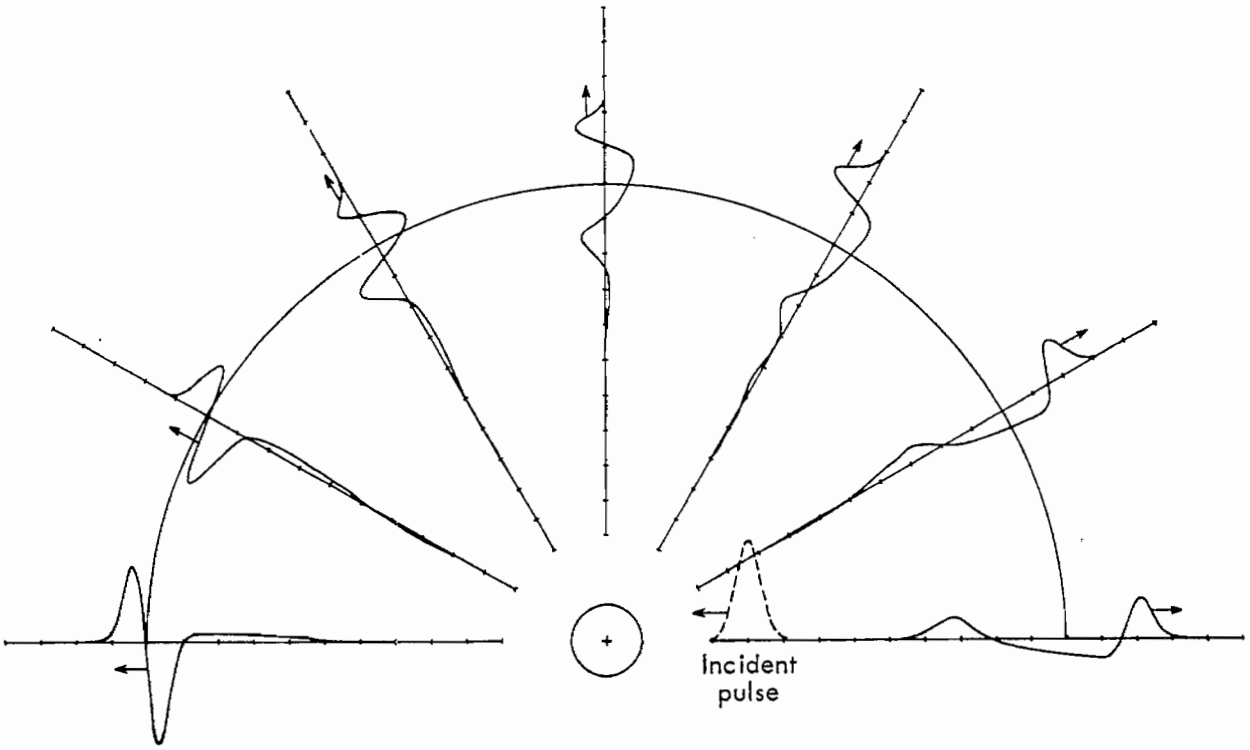

Fig. 21. Approximate impulse response of a sphere in E-plane (after Bennett and Weeks[8]).

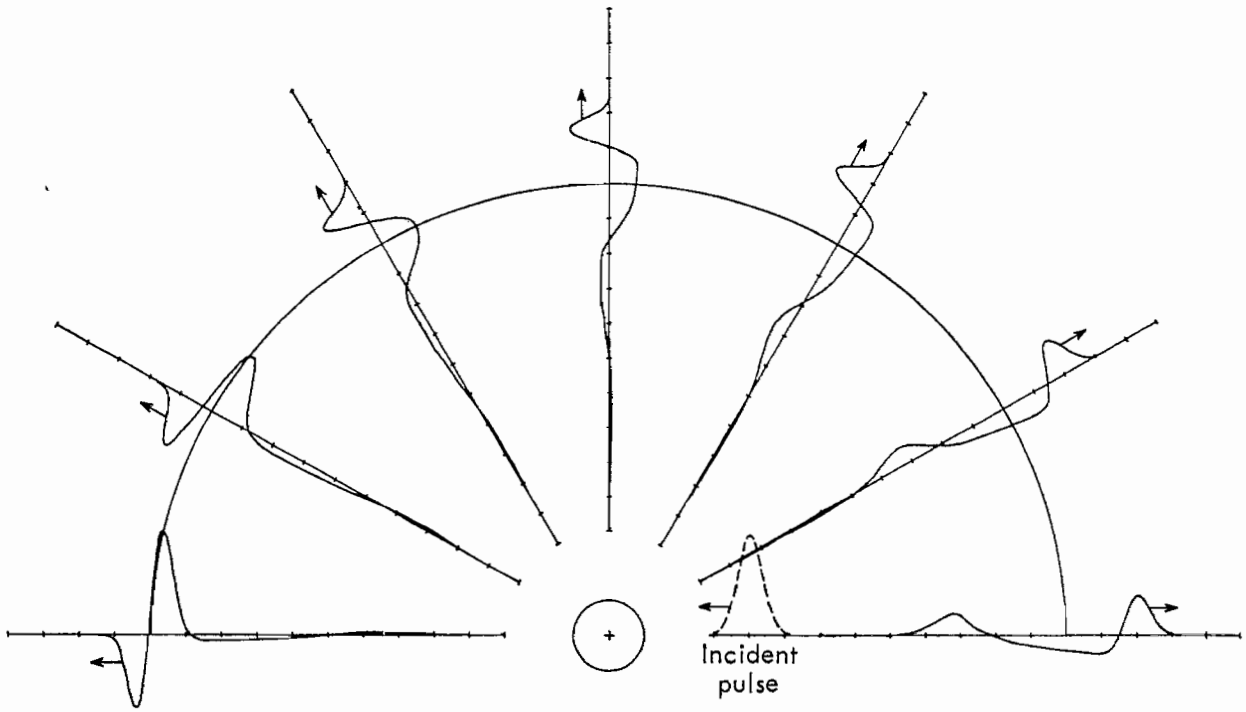

Fig. 22. Approximate impulse response of a sphere in the H-plane (after Bennett and Weeks[8]).

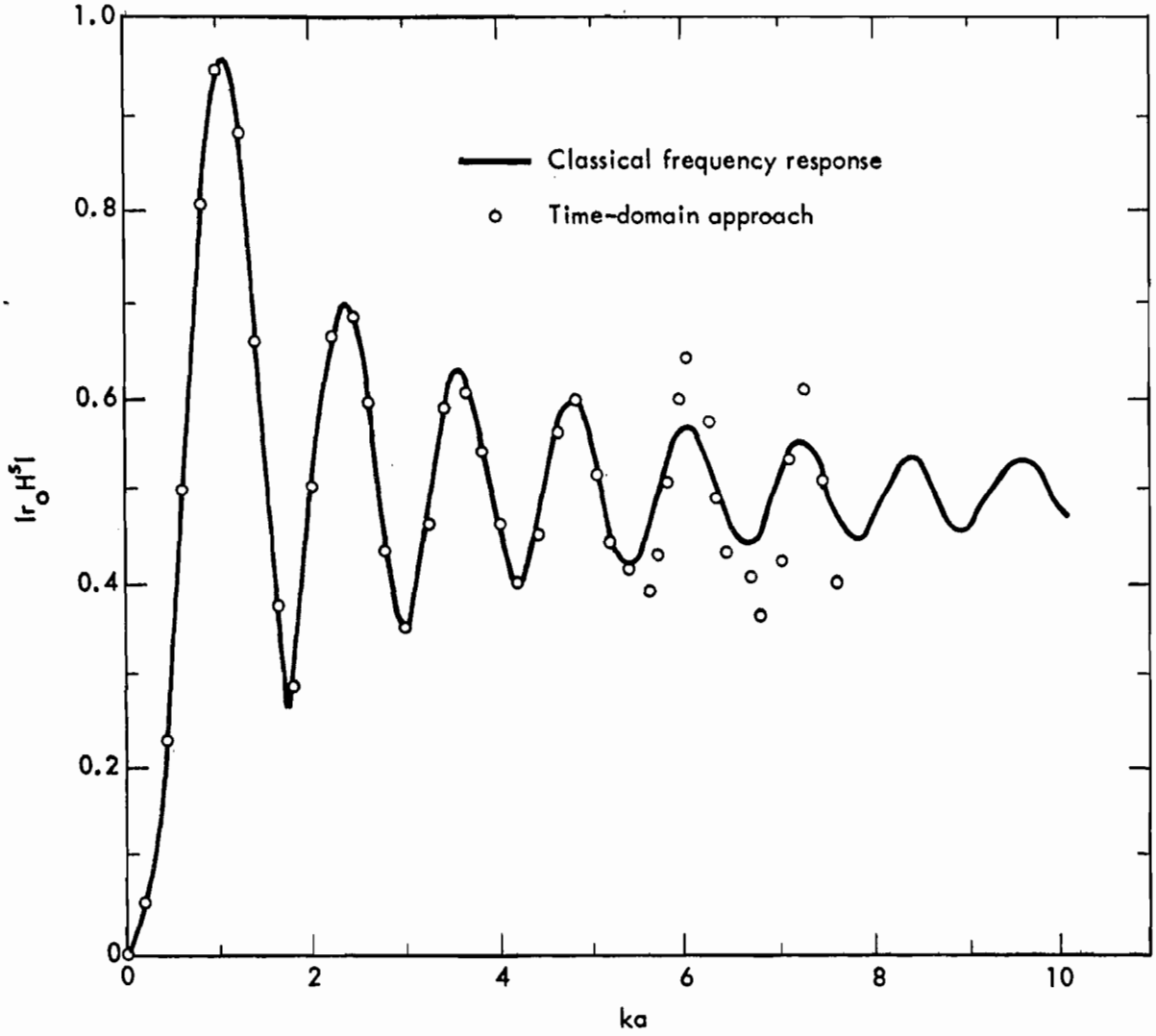

Fig. 23. Frequency response in backscatter direction of a sphere of 1-m radius (after Bennett and Weeks[8]).

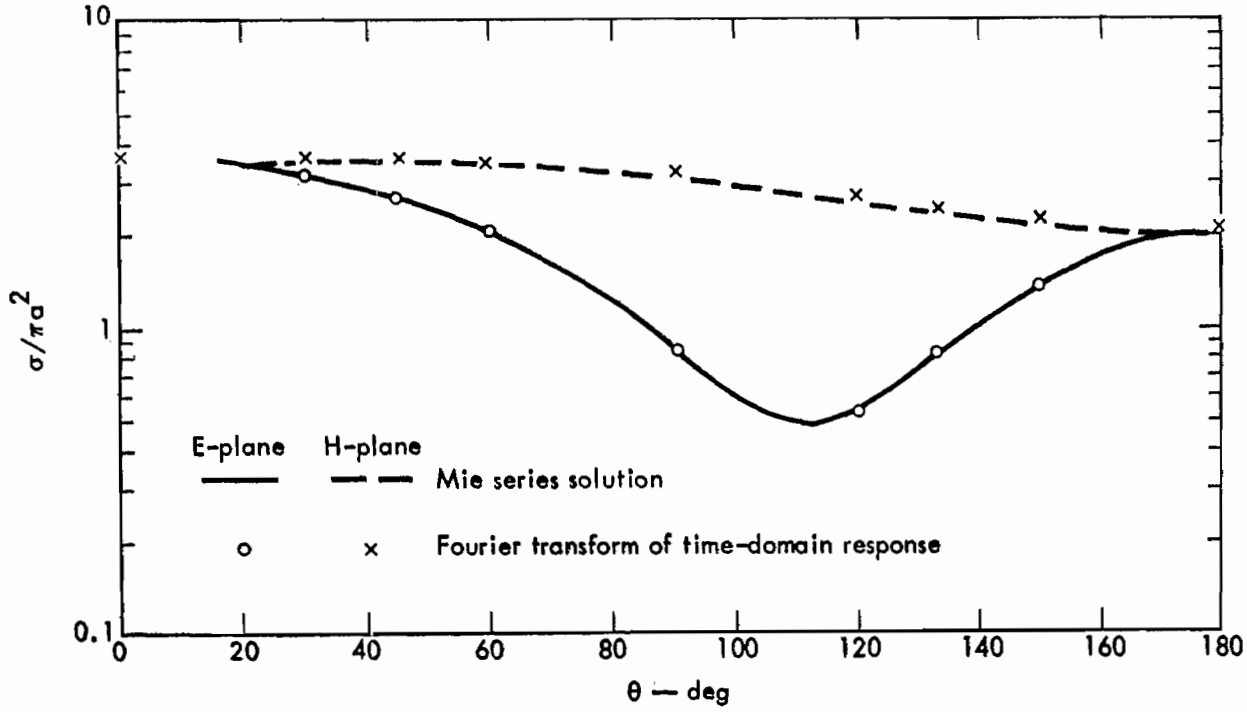

Fig. 24. Bistatic Radar Cross Section (RCS) of a sphere with ka = 1.1 (after Poggio and Miller[7]).

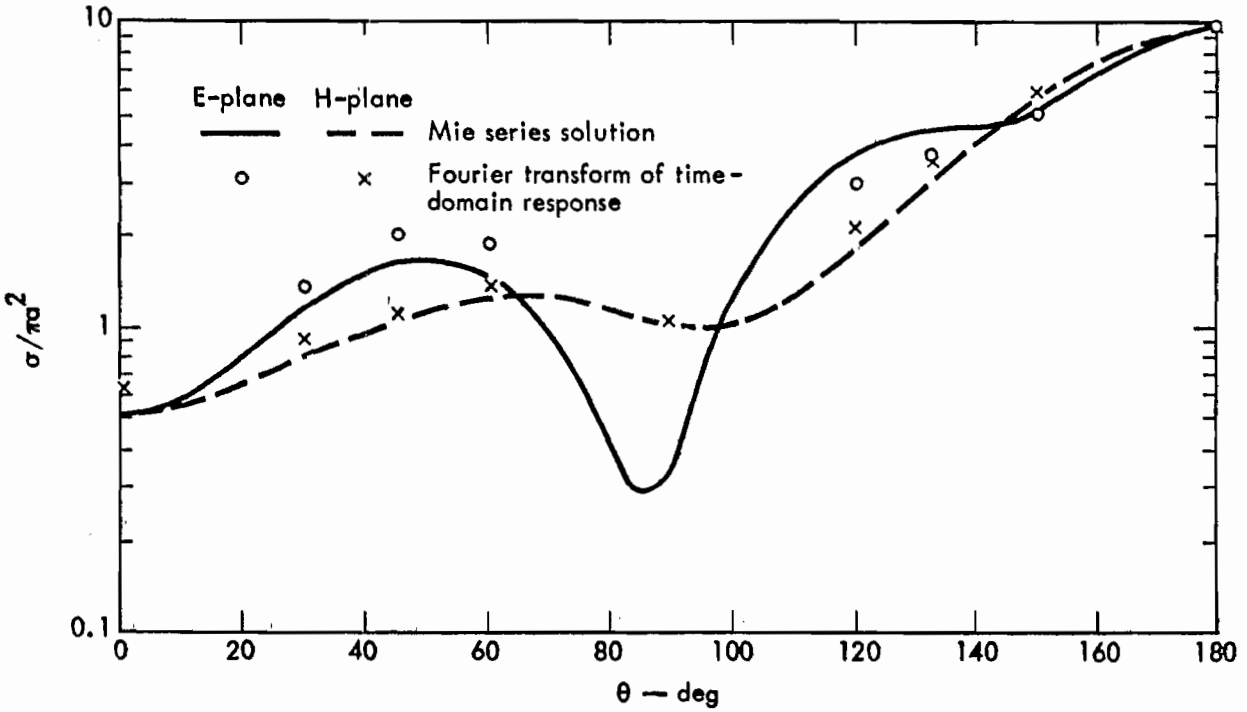

Fig. 25. Bistatic RCS of a sphere with ka = 2.9 (after Poggio and Miller[7]).

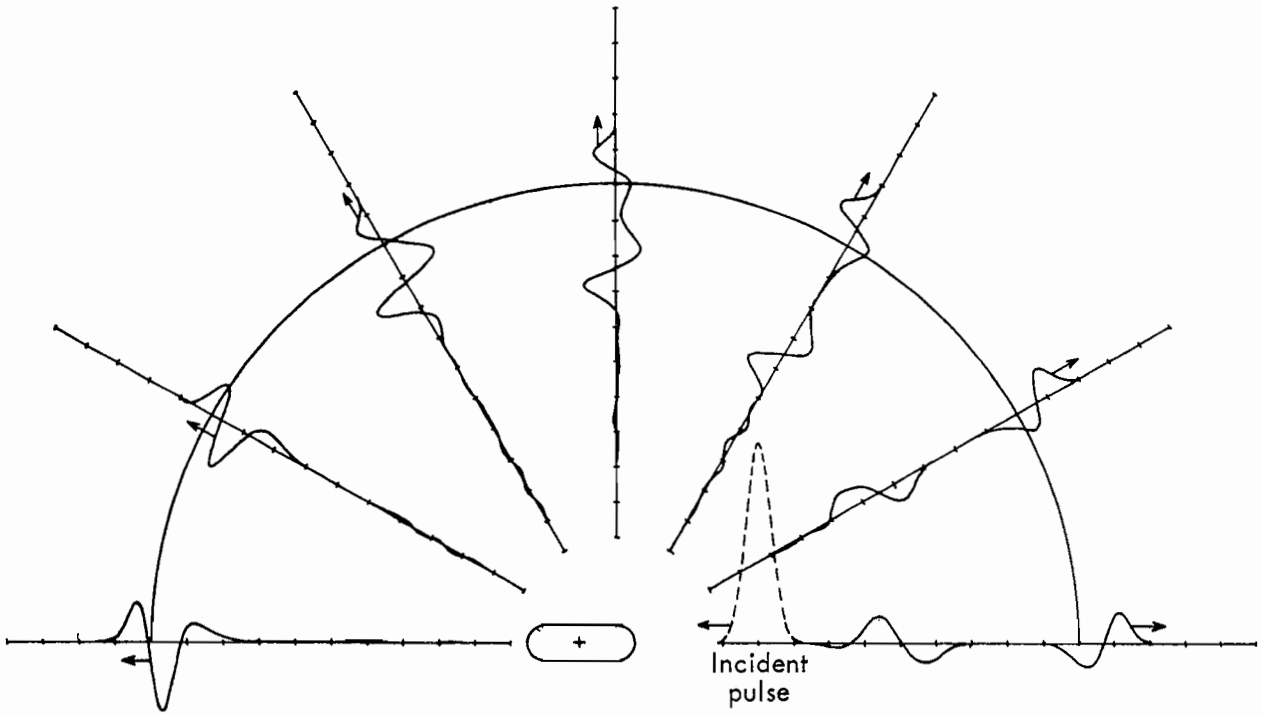

Fig. 26. Approximate impulse response of a sphere capped cylinder with axial incidence in the E-plane (after Bennett and Weeks[8]).

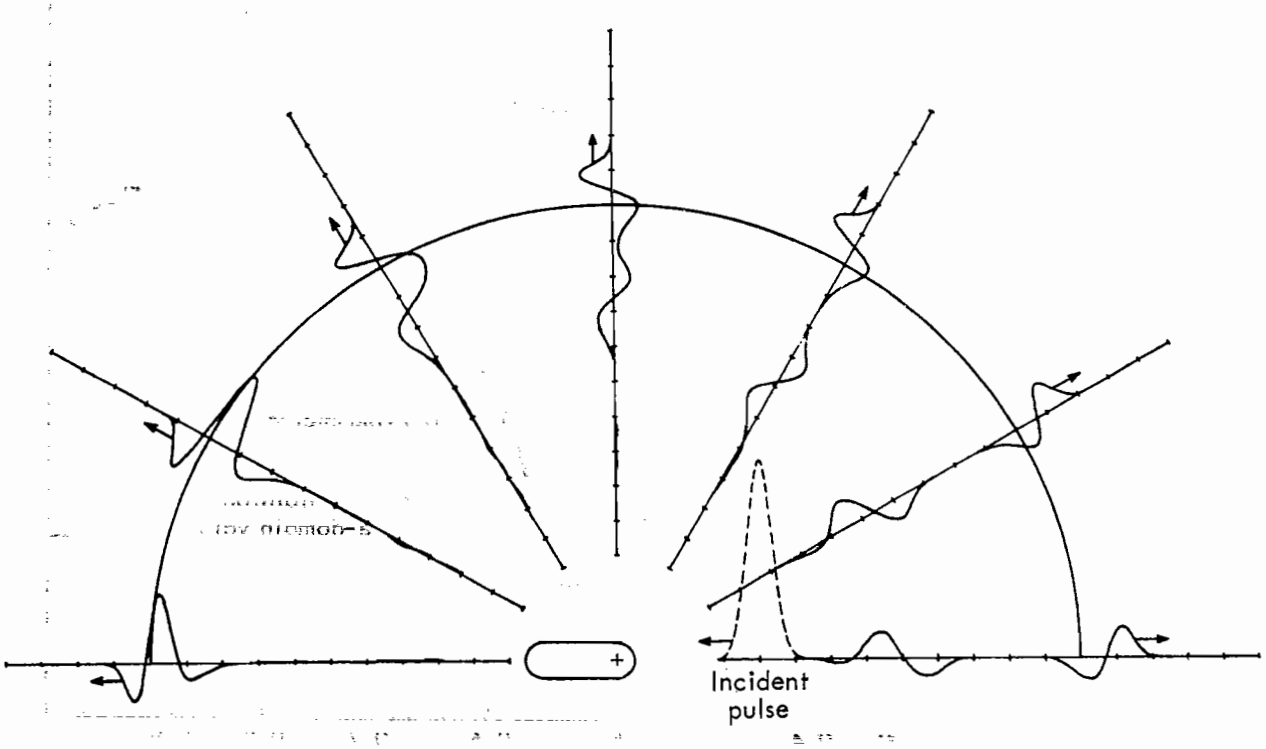

Fig. 27. Approximate impulse response of a sphere capped cylinder with axial incidence in the H-plane (after Bennett and Weeks[8]).

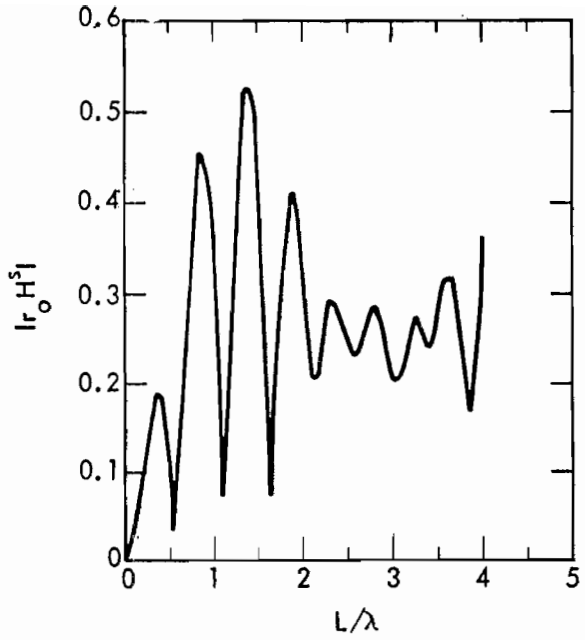

Fig. 28. Frequency response in the backscatter direction of a sphere capped cylinder with axial incidence (after Bennett and Weeks[8]).

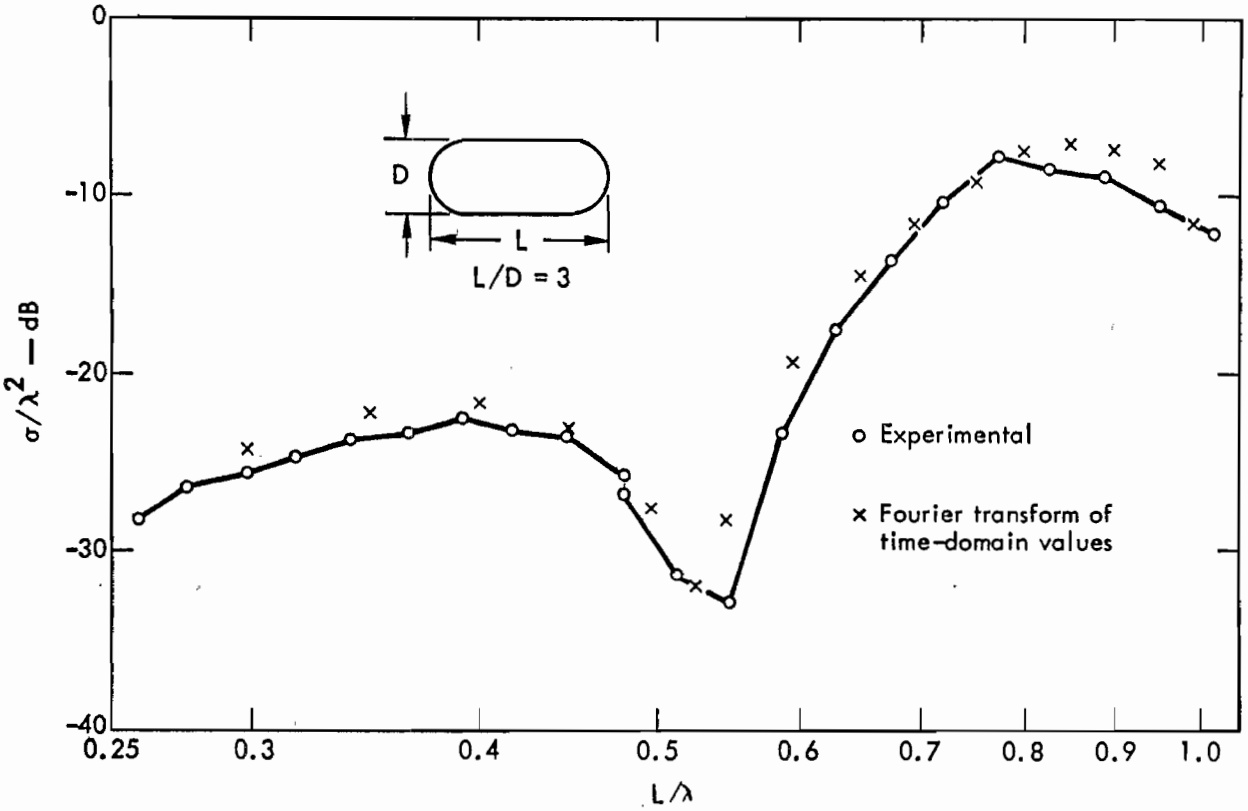

Fig. 29. Comparison of the numerical vs experimental backscatter RCS frequency response of a sphere capped cylinder for axial incidence (after Poggio and Miller[7]).

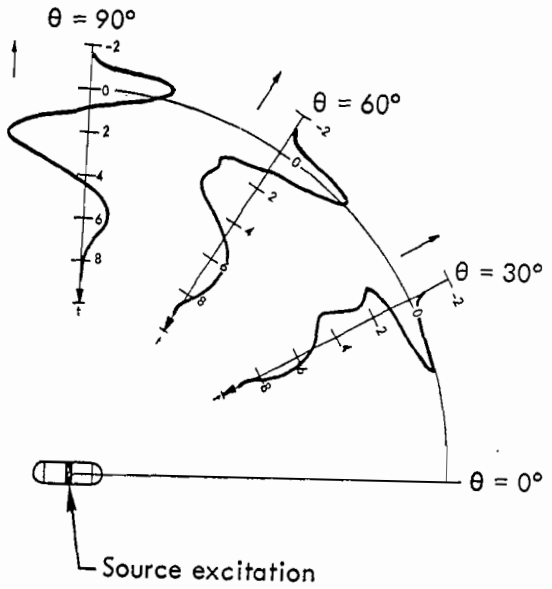

Fig. 30. Bistatic time response of a sphere capped cylinder antenna (after Poggio and Miller[7]).

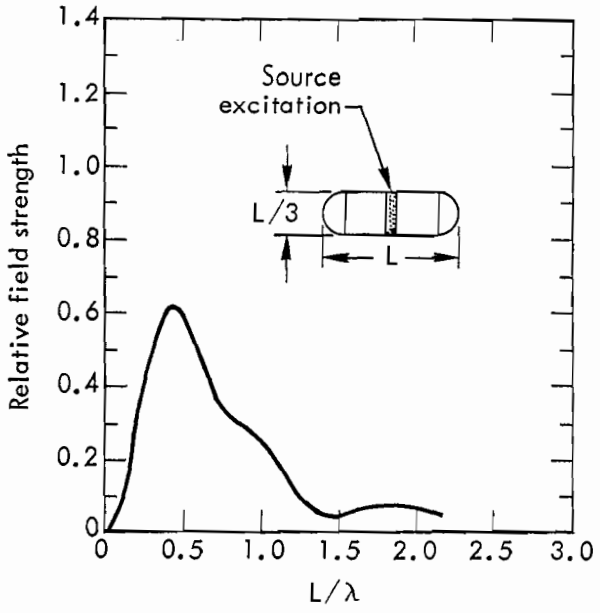

Fig. 31. Frequency response of the broadside radiation from a sphere capped cylinder antenna computed from Gaussian impulse response (after Poggio and Miller[7]).

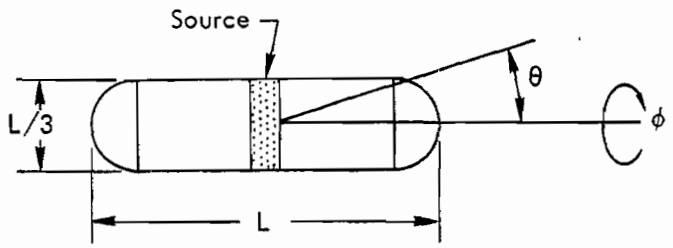

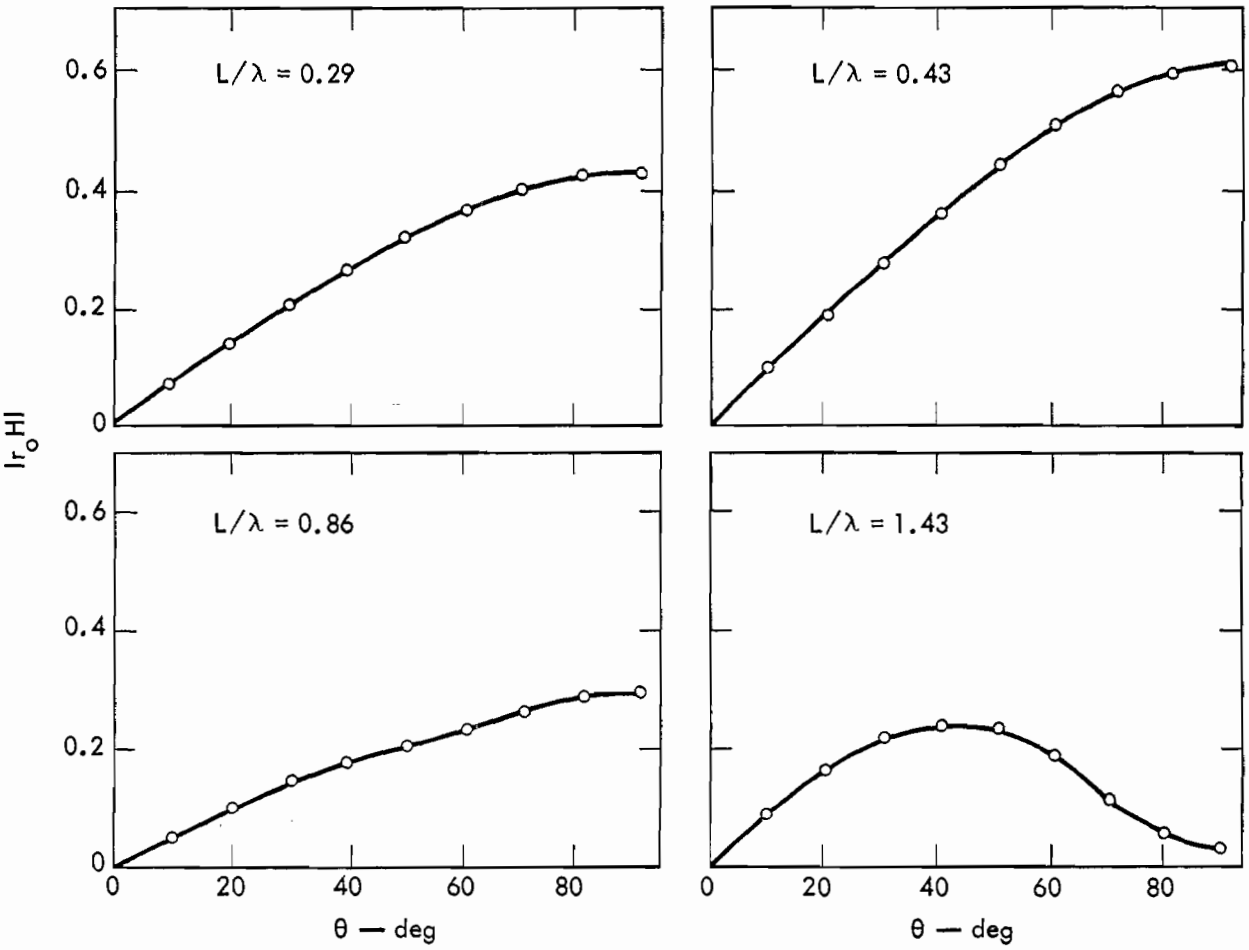

Fig. 32. Radiation pattern of a sphere-capped cylinder antenna computed from the Gaussian impulse response (after Poggio and Miller[7]).

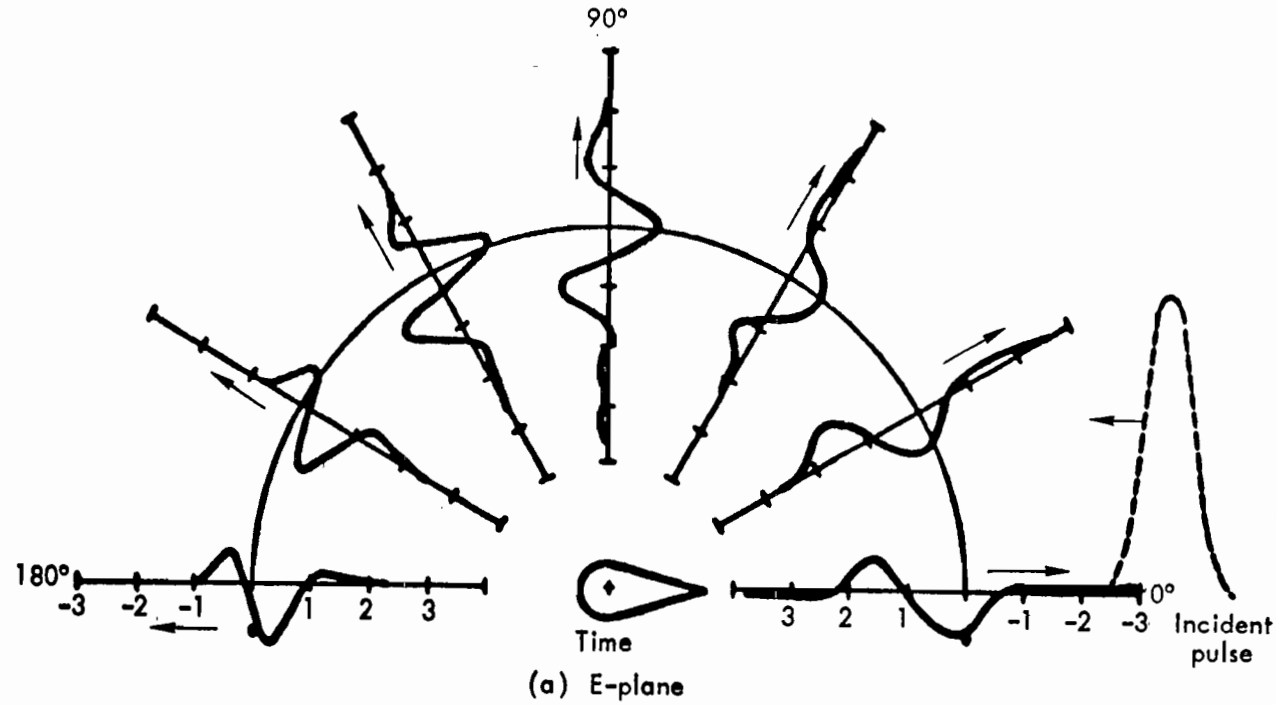

(a) E-plane

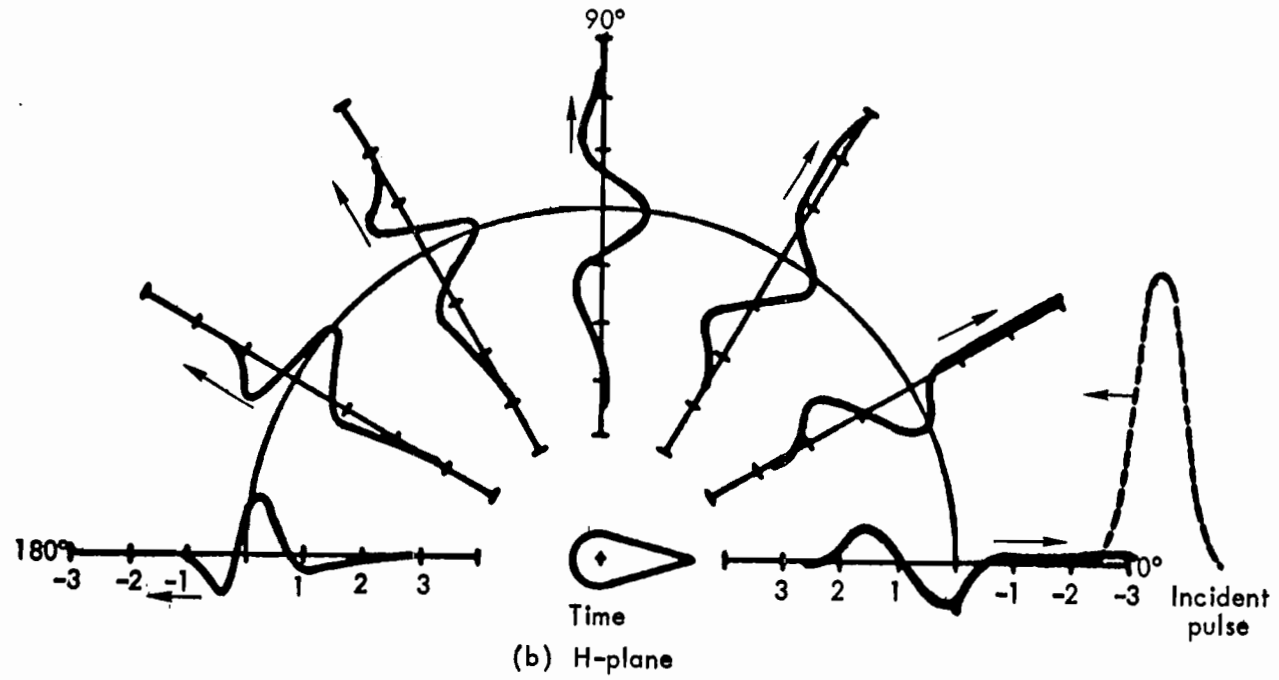

(b) H-plane

Fig. 33. Approximate bistatic impulse response of a 15 degree half-angle cone-sphere in the E- and H-planes for cone-tip incidence (after Poggio and Miller[7]).

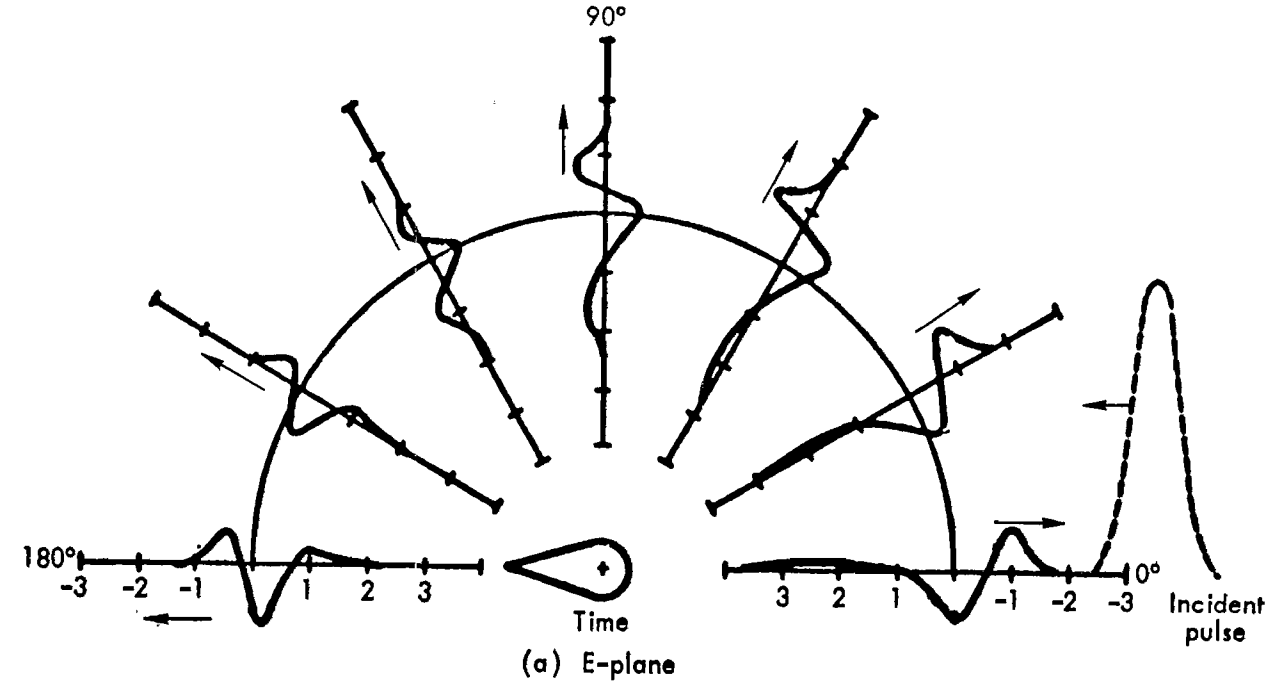

(a) E-plane

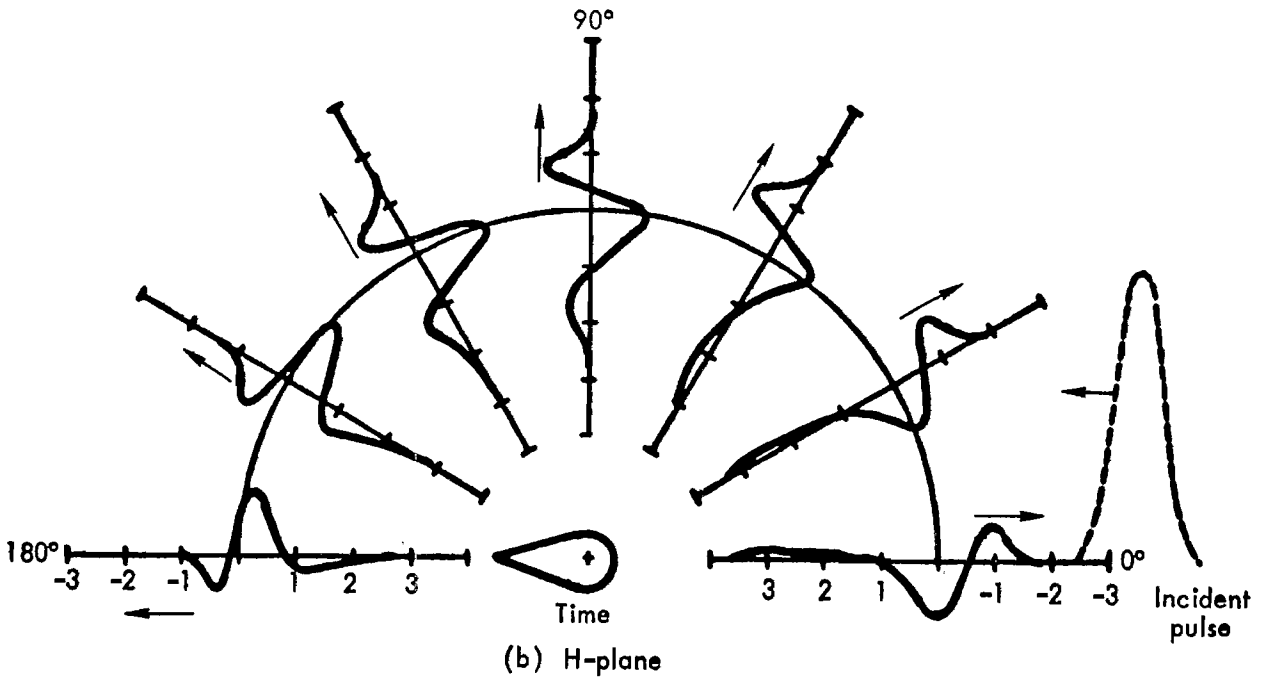

(b) H-plane

Fig. 34. Approximate bistatic impulse response of a 15 degree half-angle cone-sphere in the E- and H-planes for sphere-end incidence (after Poggio and Miller[7]).

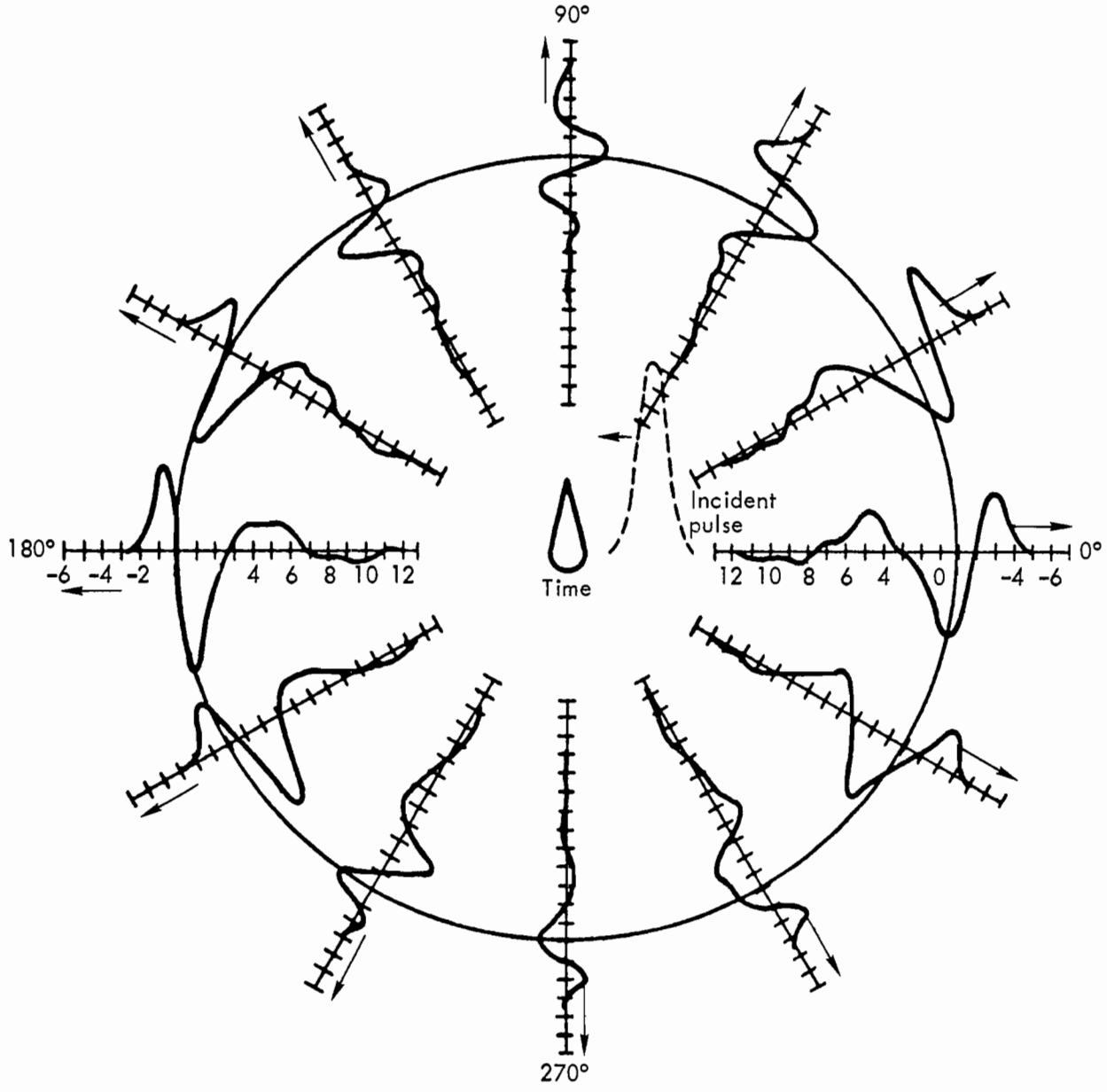

Fig. 35. Approximate bistatic impulse response of a 15 degree half-angle cone-sphere in the E-plane for broadside incidence (after Poggio and Miller[7]).

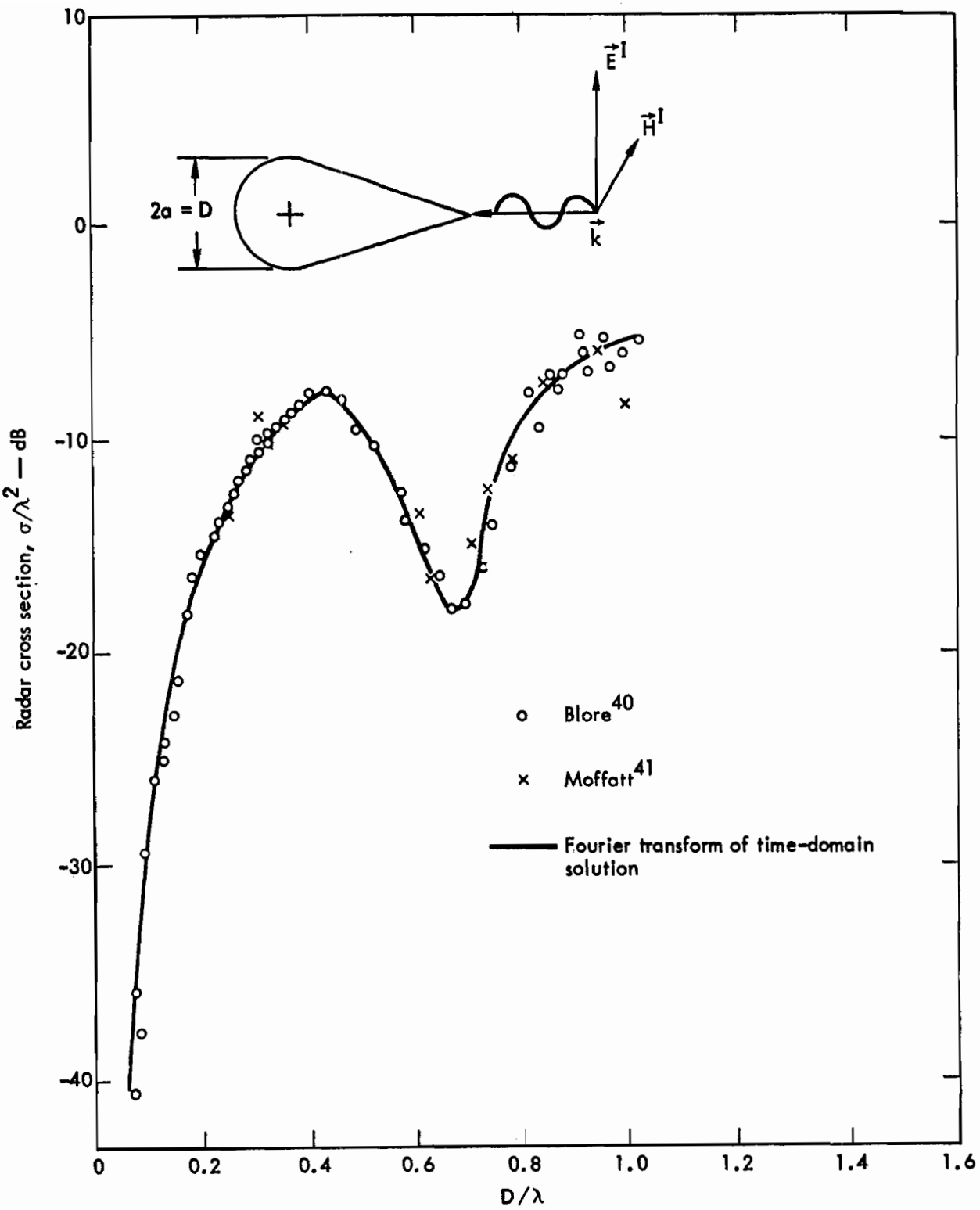

Fig. 36. Comparison of the numerical vs experimental backscatter RCS frequency response of a 15 degree half-angle cone-sphere for cone-tip incidence (after Poggio and Miller[7]).

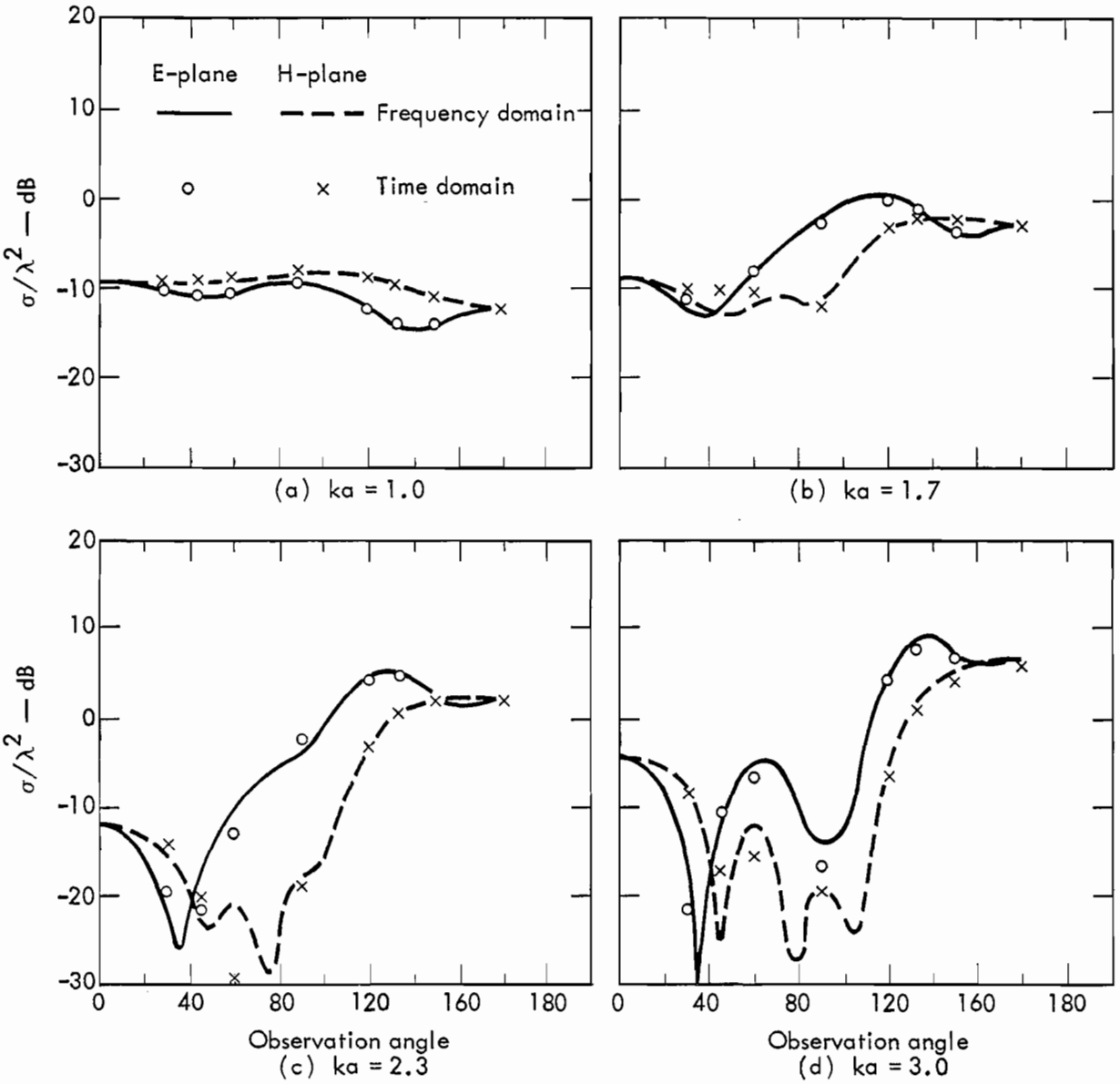

Fig. 37. Bistatic scattering pattern for tip incidence on a 15 degree half-angle cone sphere as computed using frequency-domain and Fourier transformed time-domain results (after Poggio and Miller[7]).

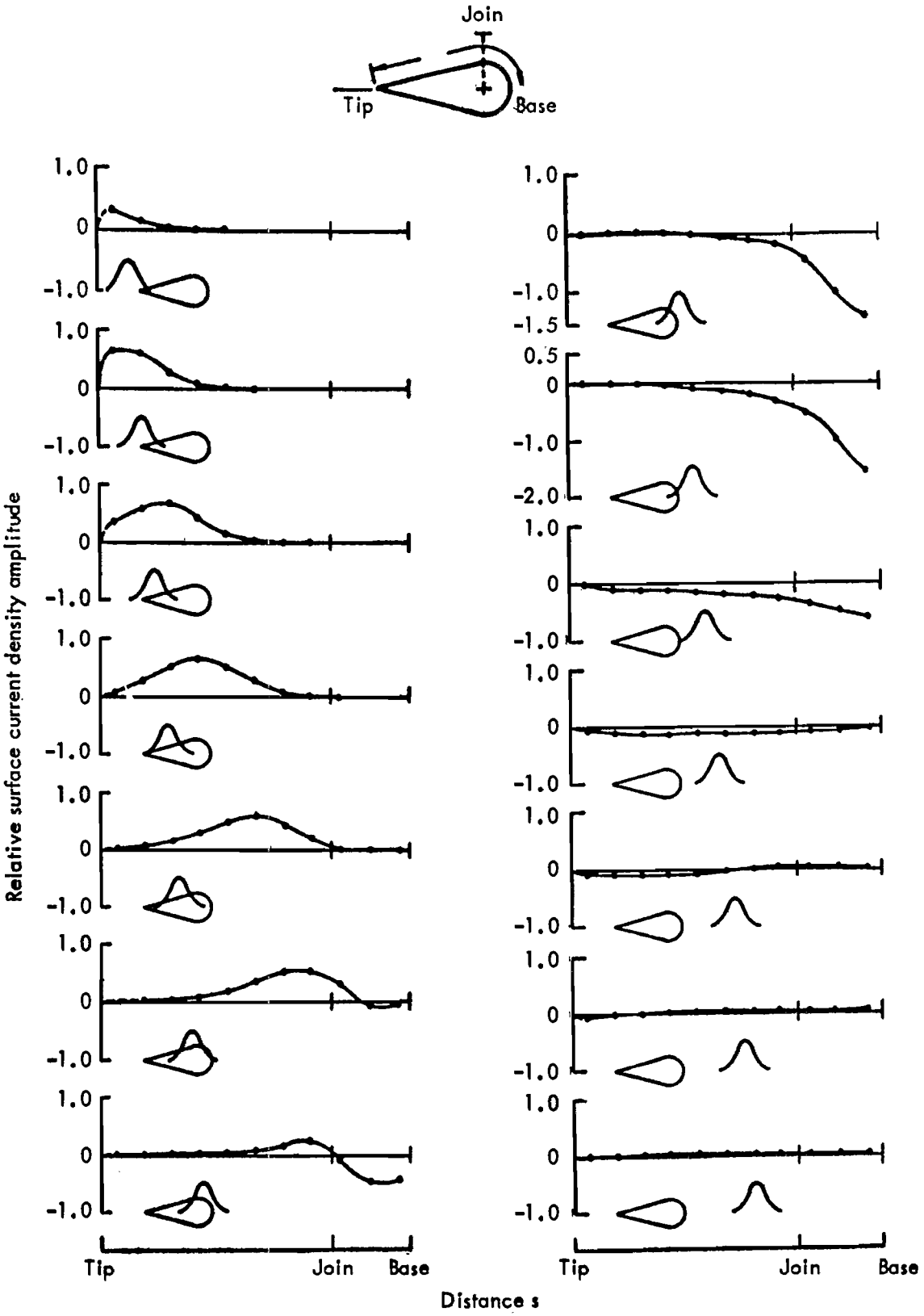

Fig. 38. H-plane component of the induced current on a 15 degree half-angle cone-sphere for cone-tip incidence (after Poggio and Miller[7]).

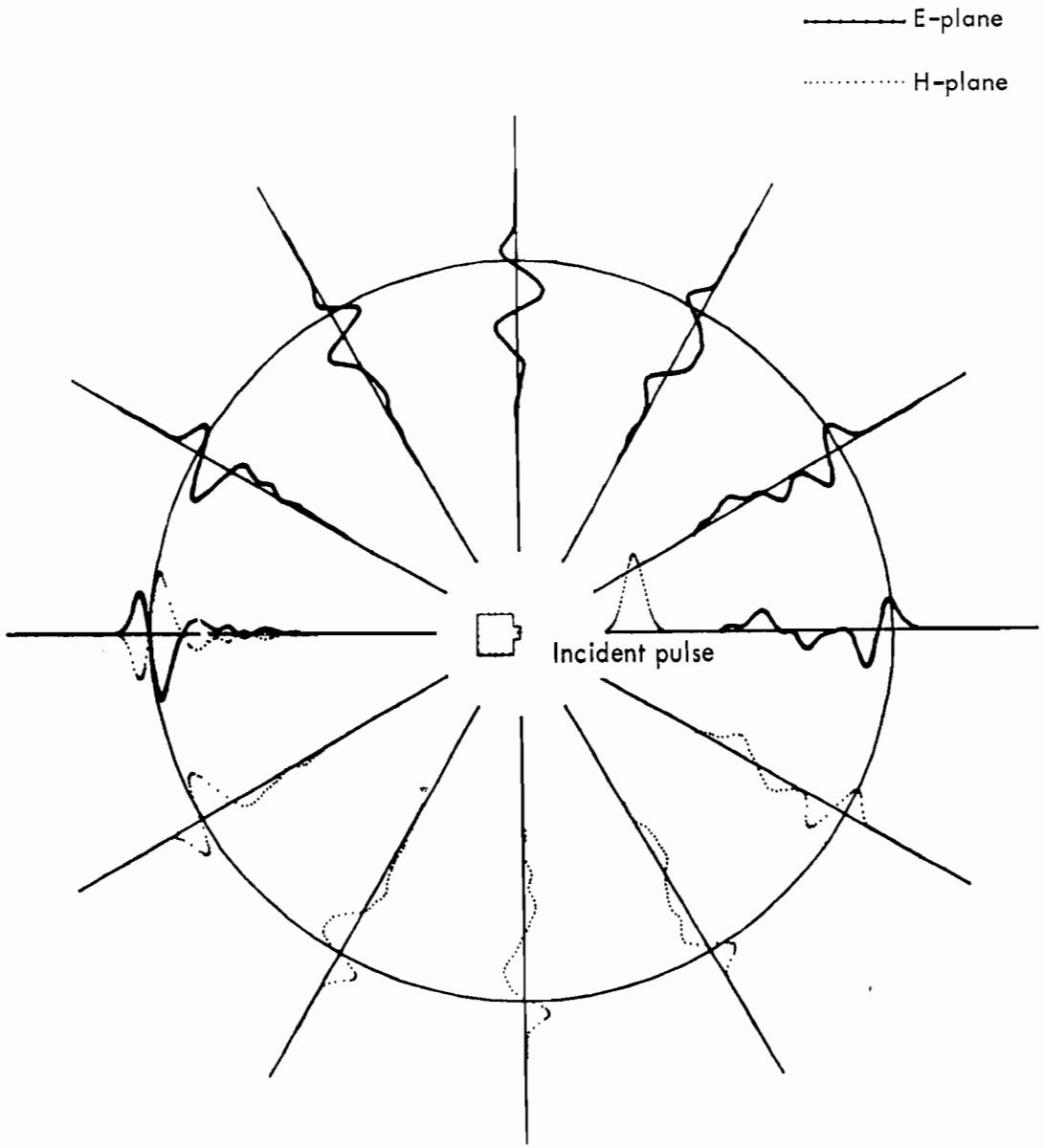

Fig. 39. Smoothed impulse response of ADC satellite model (after Bennett, DeLorenzo, and Auckenthaler[10]).

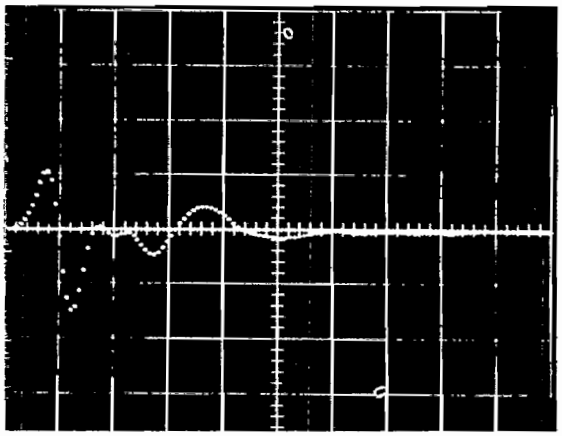

(a) Measured ADC response
(horizontal scale = 0.5 nsec/div)

(b) Calculated ADC response

Fig. 40. Comparison of calculated and measured ADC response in backscatter direction (after Bennett, DeLorenzo, and Auckenthaler[10]).

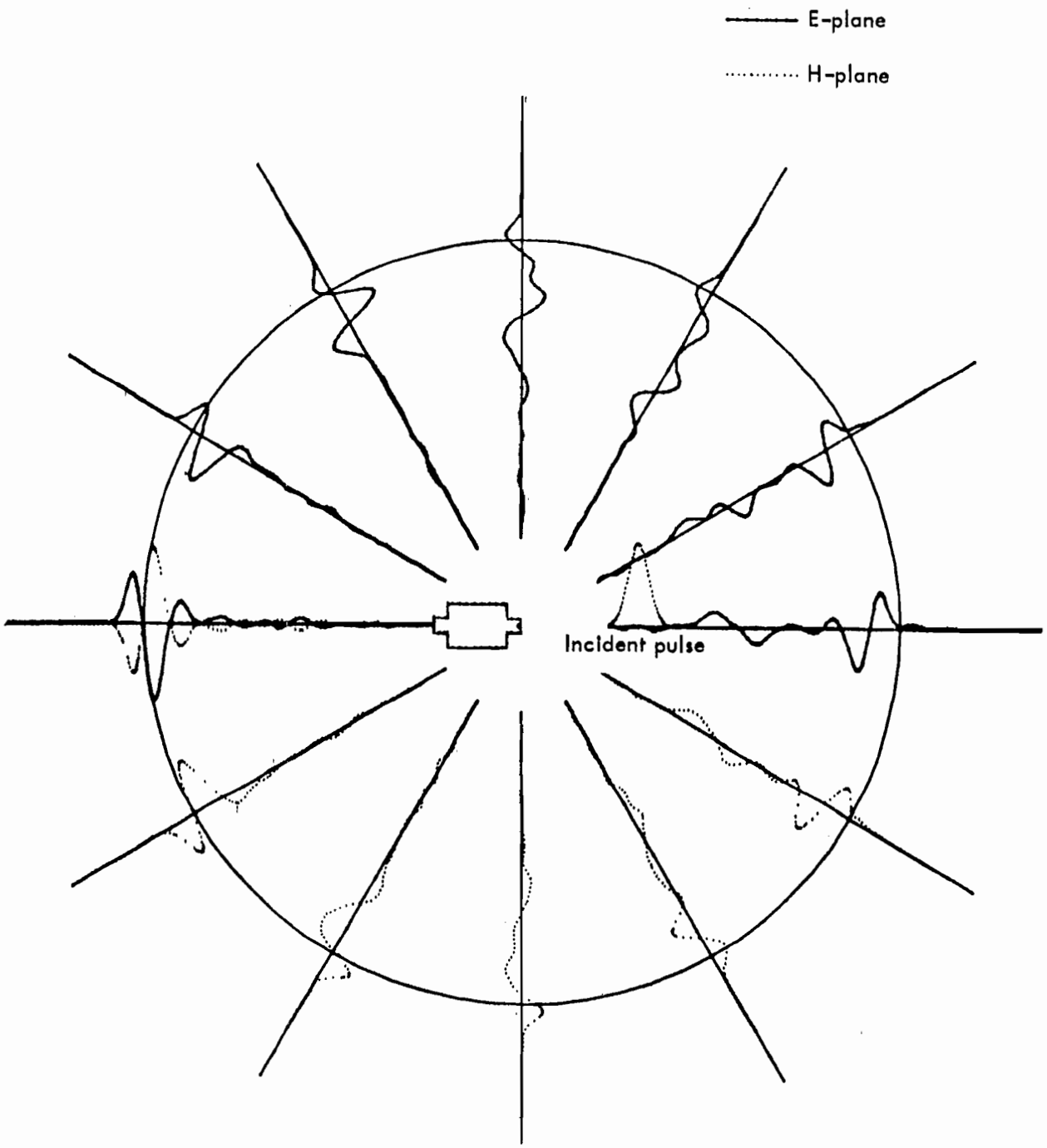

Fig. 41. Smoothed impulse response of UES satellite model (after Bennett, DeLorenzo, and Auckenthaler[10]).

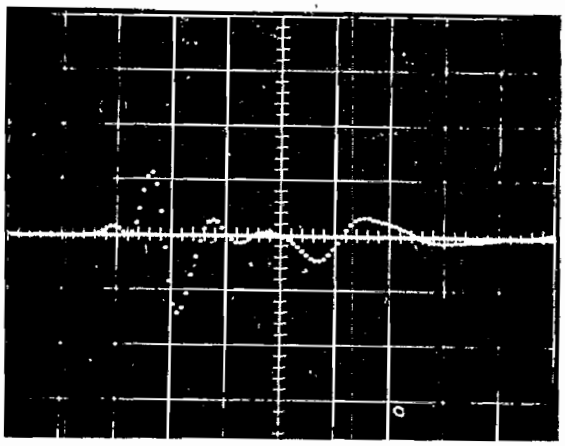

(a) Measured UES response
(horizontal scale = 0.5 nsec/div)

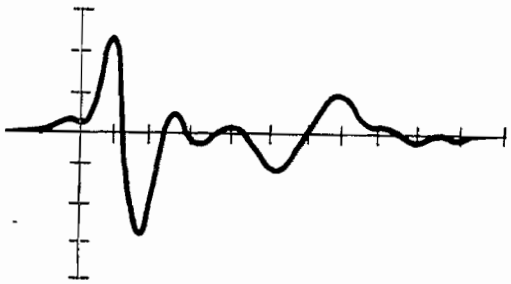

(b) Calculated UES response

Fig. 42. Comparison of calculated and measured UES response in backscatter direction (after Bennett, DeLorenzo, and Auckenthaler[10]).

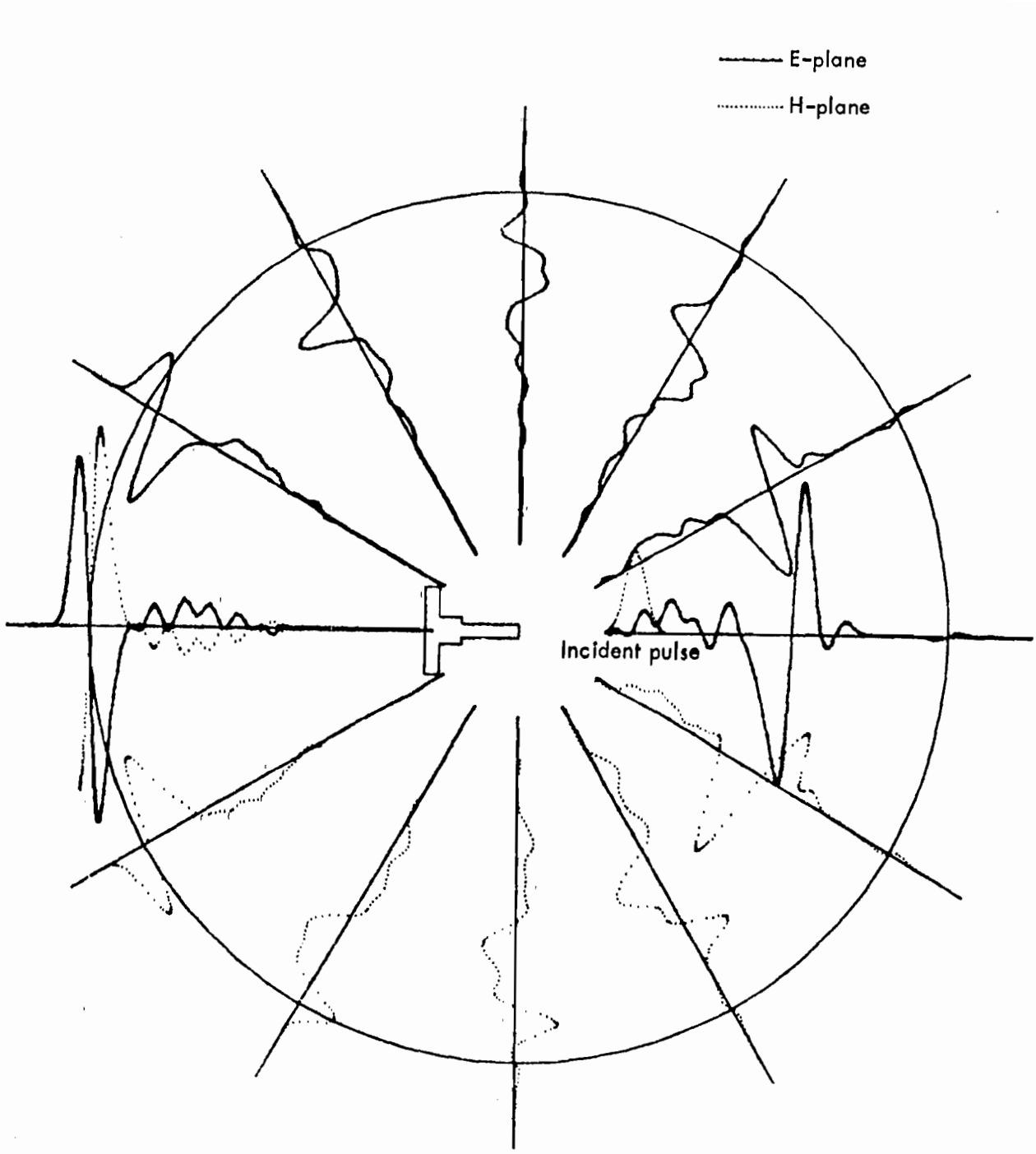

Fig. 43. Smoothed impulse response of GGTS-2 satellite model (after Bennett, DeLorenzo, and Auckenthaler[10]).

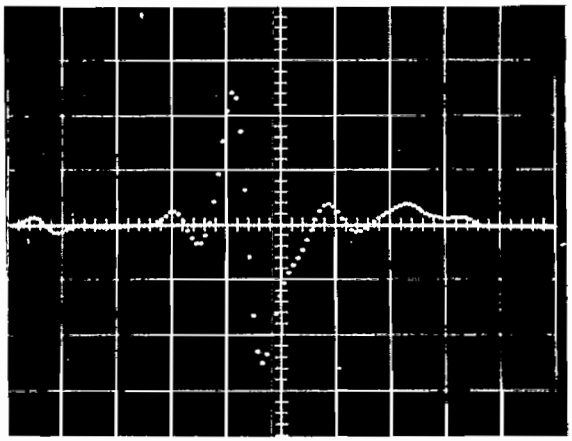

(a) Measured GGTS-2 response
(horizontal scale = 0.5 nsec/div)

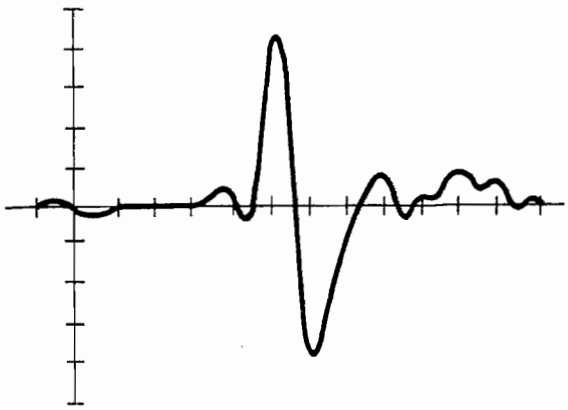

(b) Calculated GGTS-2 response

Fig. 44. Comparison of calculated and measured GGTS-2 response in backscatter direction (after Bennett, DeLorenzo, and Auckenthaler[10]).

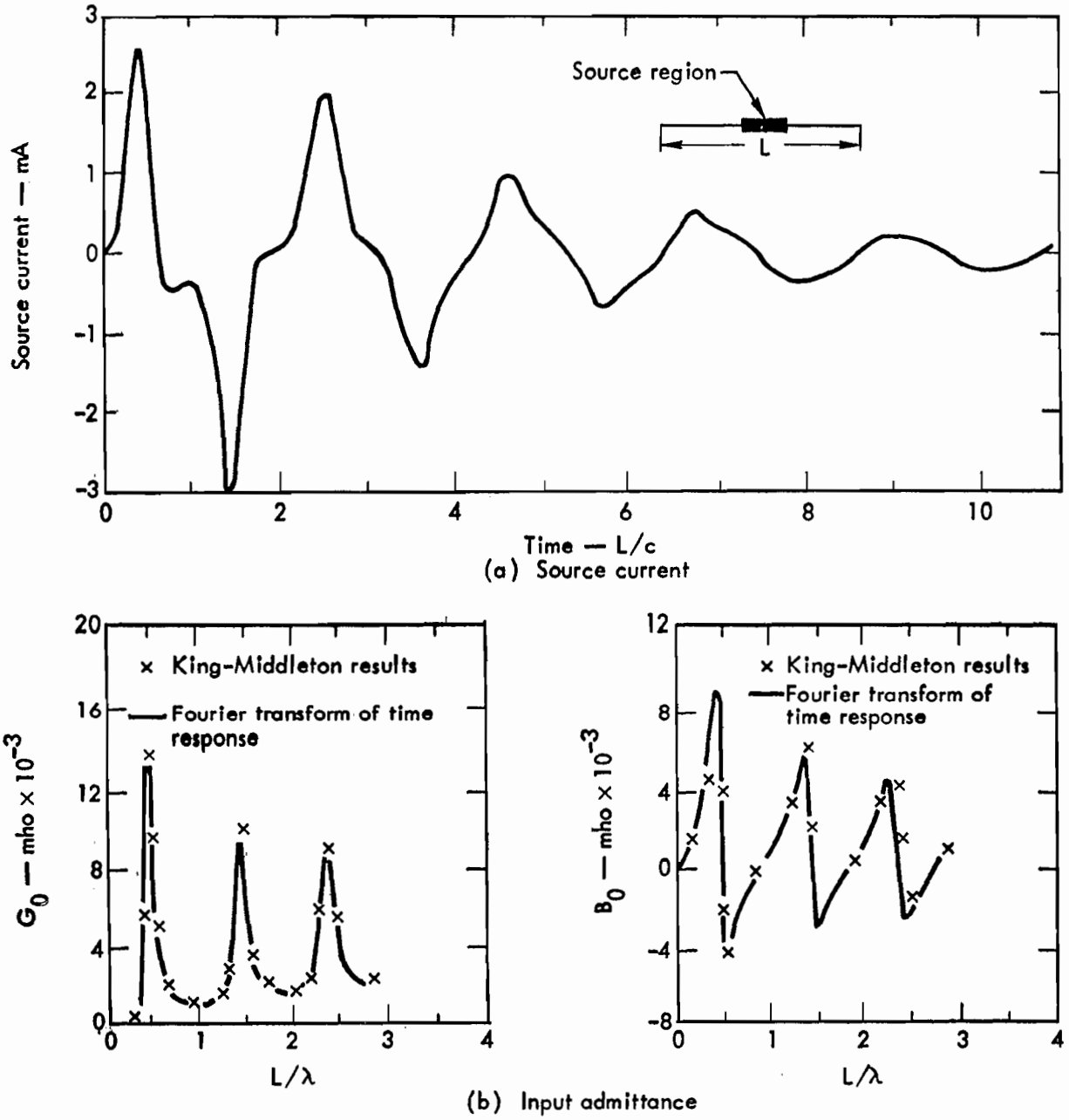

Fig. 45. Linear antenna with Gaussian source where the ratio of wire radius to length is 0.00674, the source width is L/11, and the number of spatial segments 22. $V_s = \exp[-A^2(t - t_{max})^2$ with $A = 1.5 \times 10^9$ and $t_{max} = 1.43 \times 10^{-9}$ sec. King-Middleton results are plotted for comparison (after Poggio, Miller and Burke[12]).

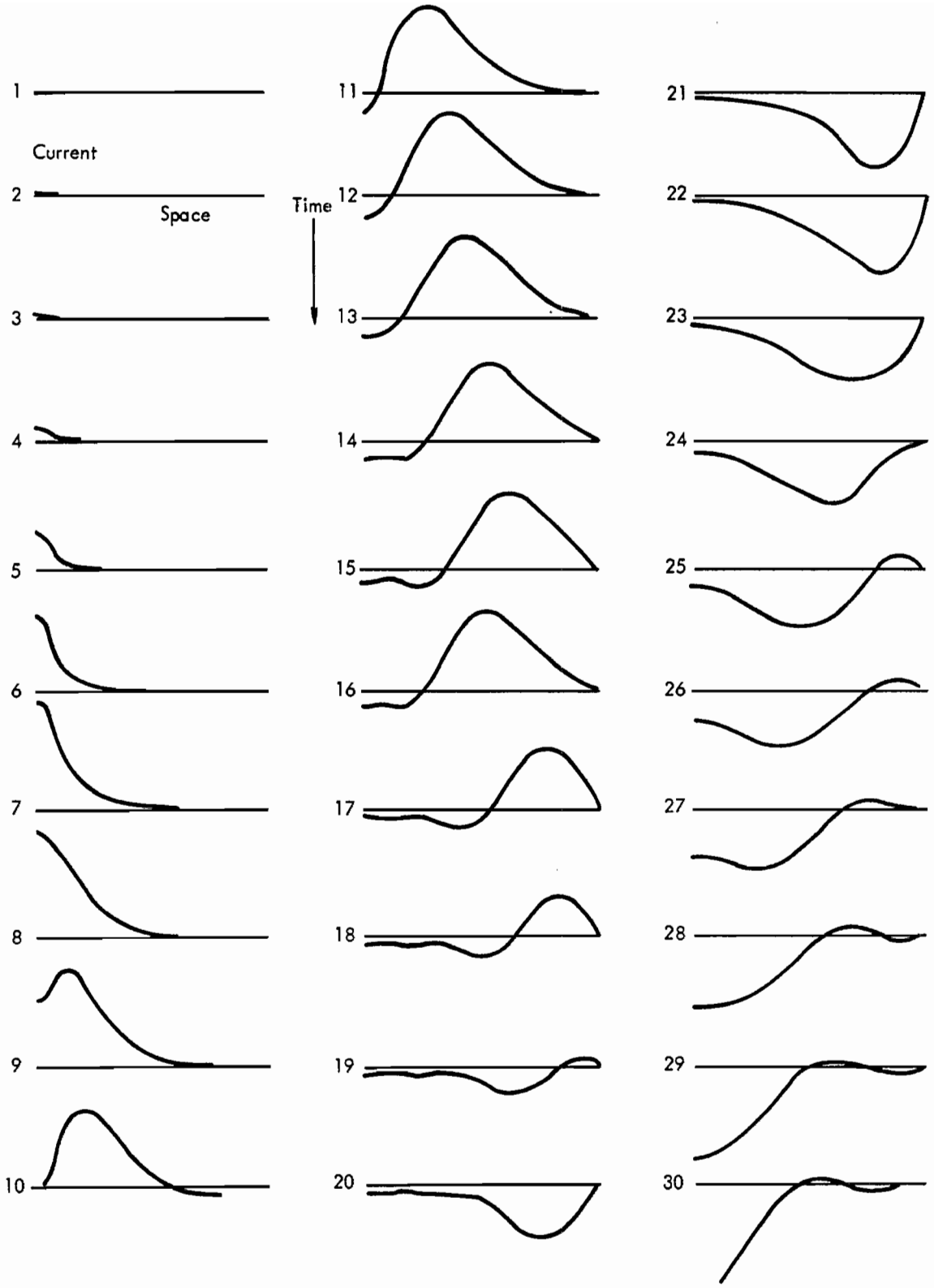

Fig. 46. Time history of dipole antenna current (after Poggio, Miller, and Burke[12]).

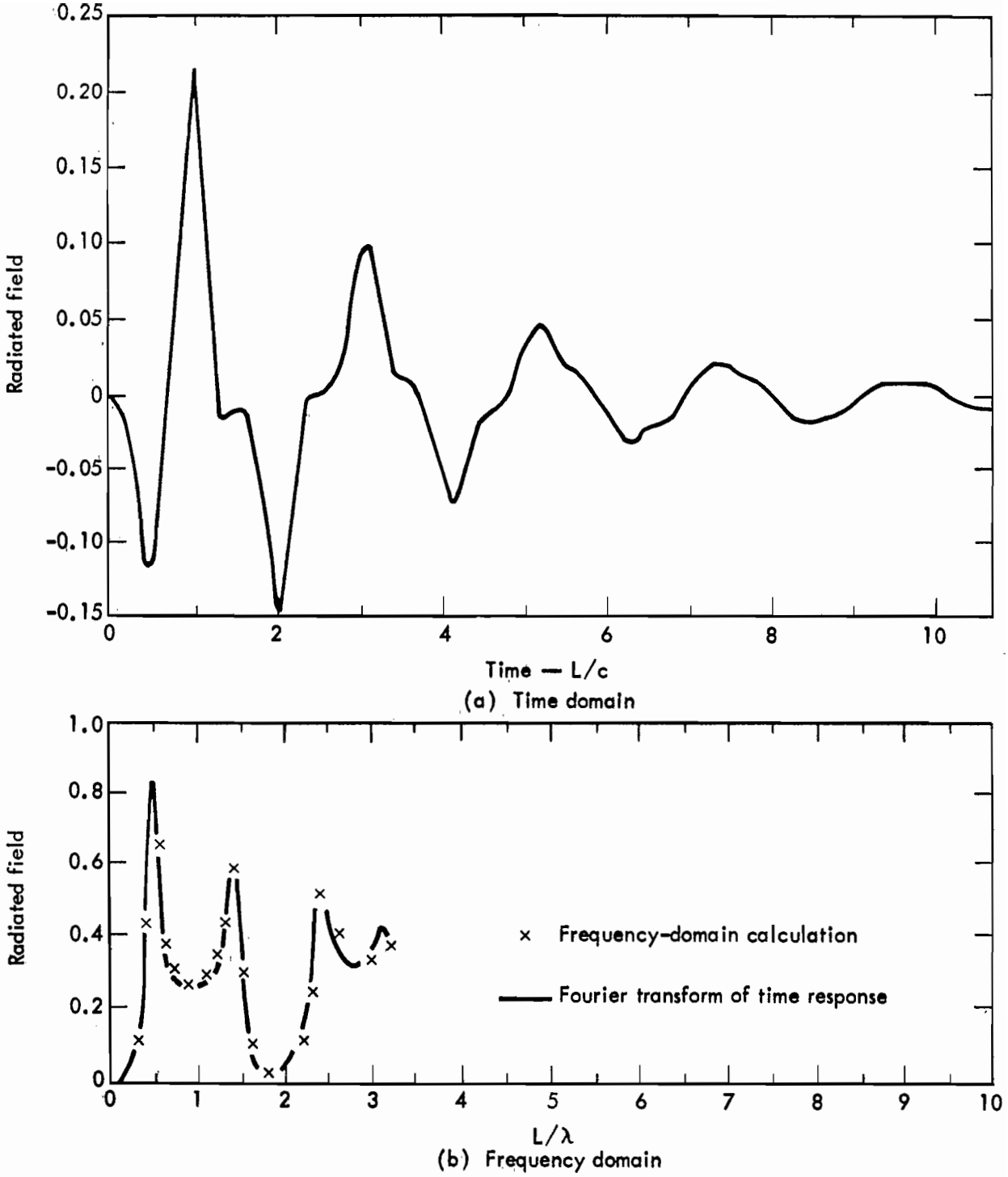

Fig. 47. Broadside radiated field of a linear antenna (after Poggio, Miller, and Burke[12]).

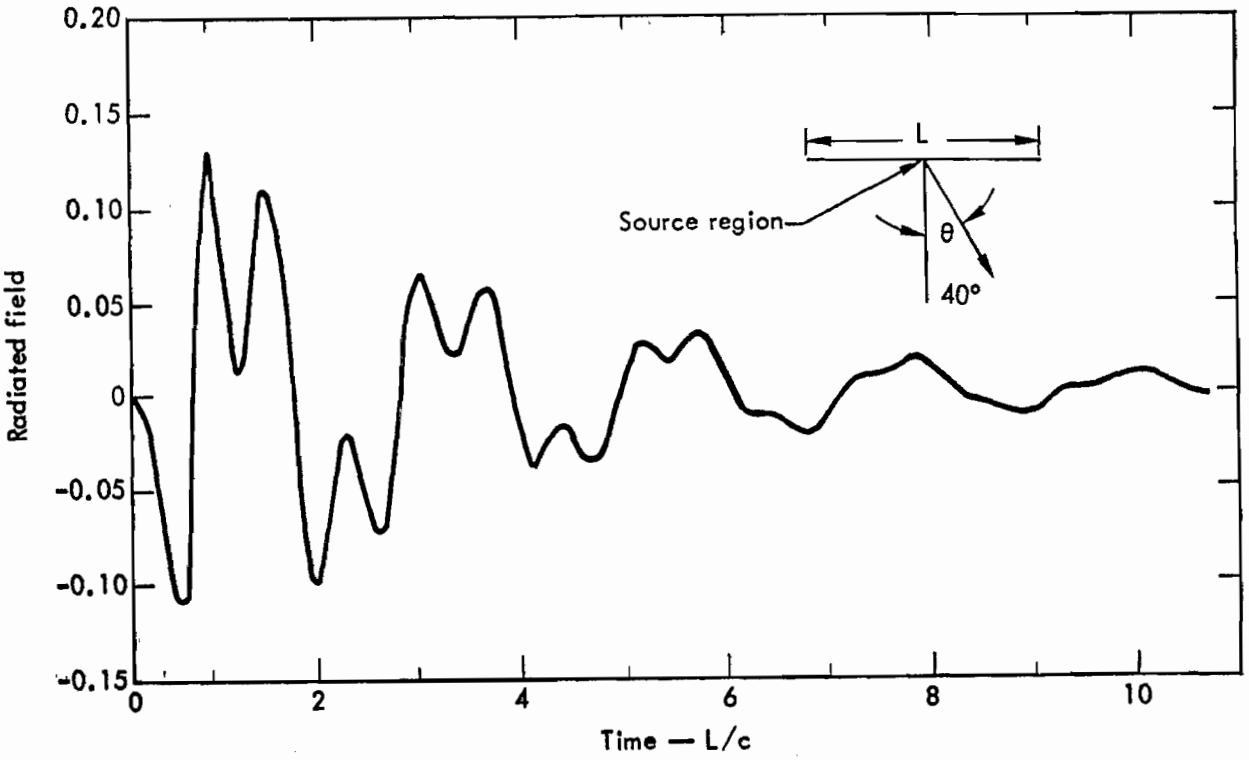

Fig. 48. Radiated field of linear antenna with Gaussian source time dependence. The radiated field is at an angle 40 degrees from broadside (after Poggio, Miller, and Burke[12]).

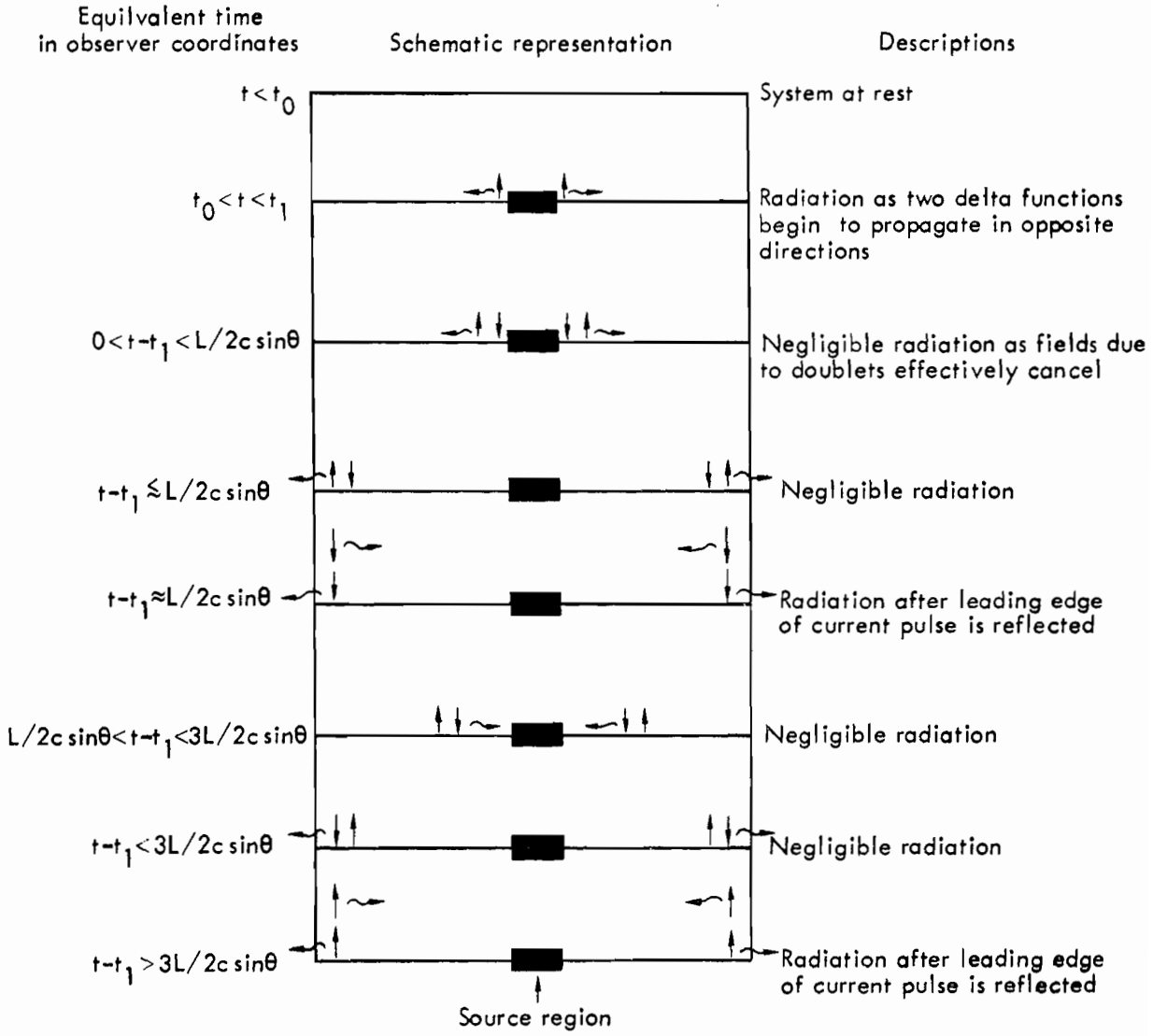

Fig. 49. Schematic representation of the radiation mechanism (after Poggio, Miller, and Burke[12]).

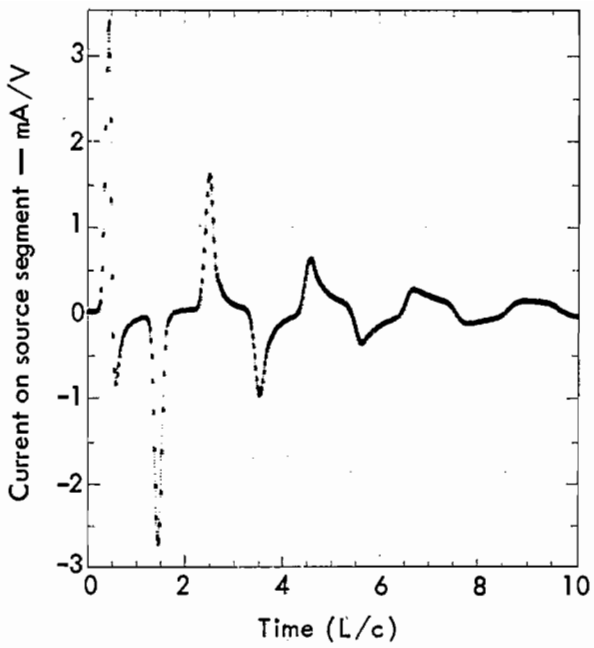

Fig. 50. Results computed from a time-domain solution for the current at the center of the two symmetric source segments of a straight wire antenna, having 48 segments, a length of 1 m, a radius of 0.00674 m, and $A = 3.25 \times 10^9$ (see Fig. 45 for comparison).

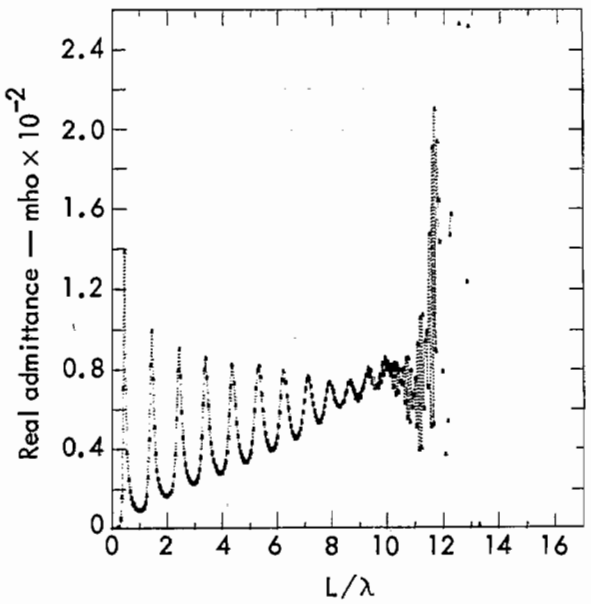

Fig. 51. The real part of the input admittance obtained from the Fourier transform of the results represented in Fig. 50.

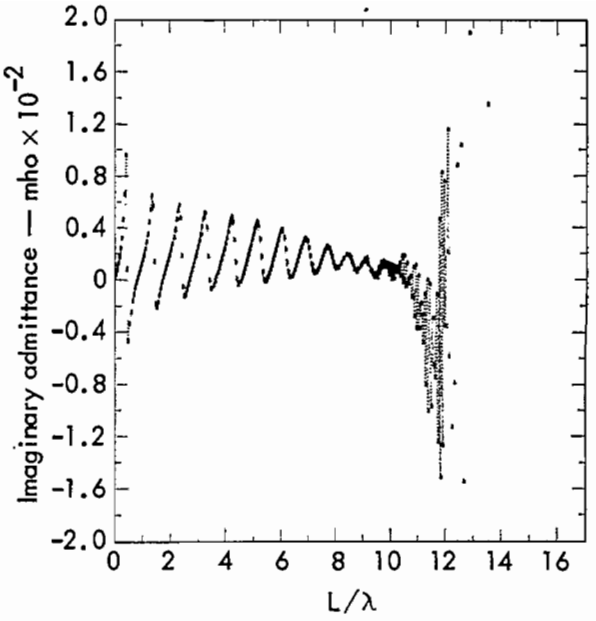

Fig. 52. The imaginary part of the input admittance obtained from the Fourier transform of the results represented in Fig. 50.

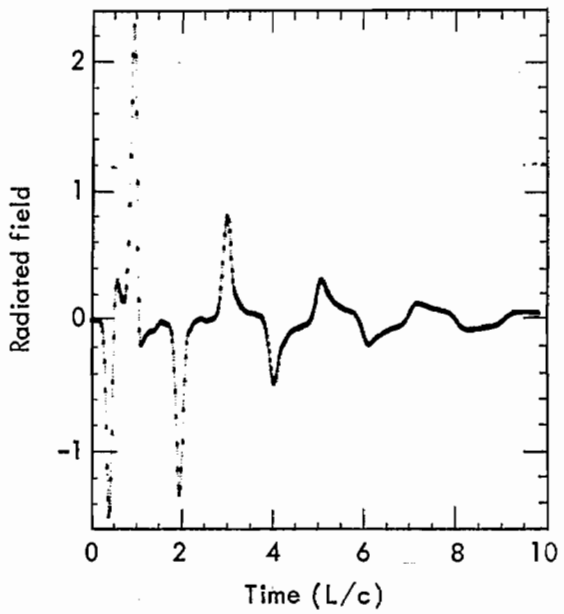

Fig. 53. The time-dependent broadside radiated field for the antenna of Fig. 50.

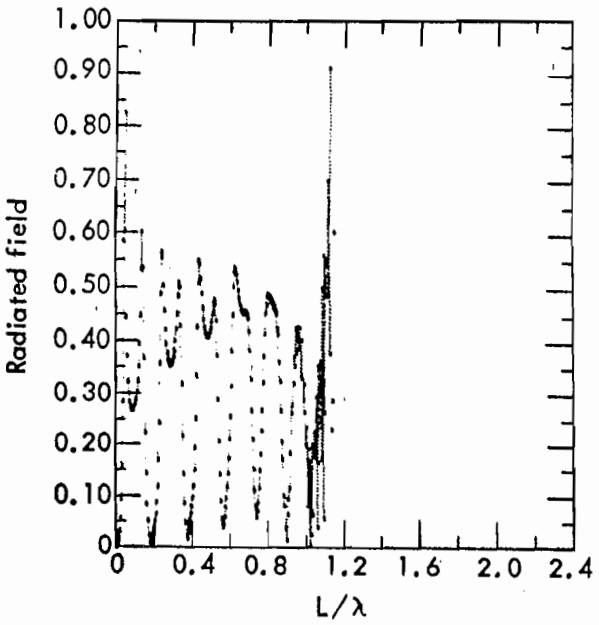

Fig. 54. The frequency dependence of the broadside radiated field for the antenna described in Fig. 50.

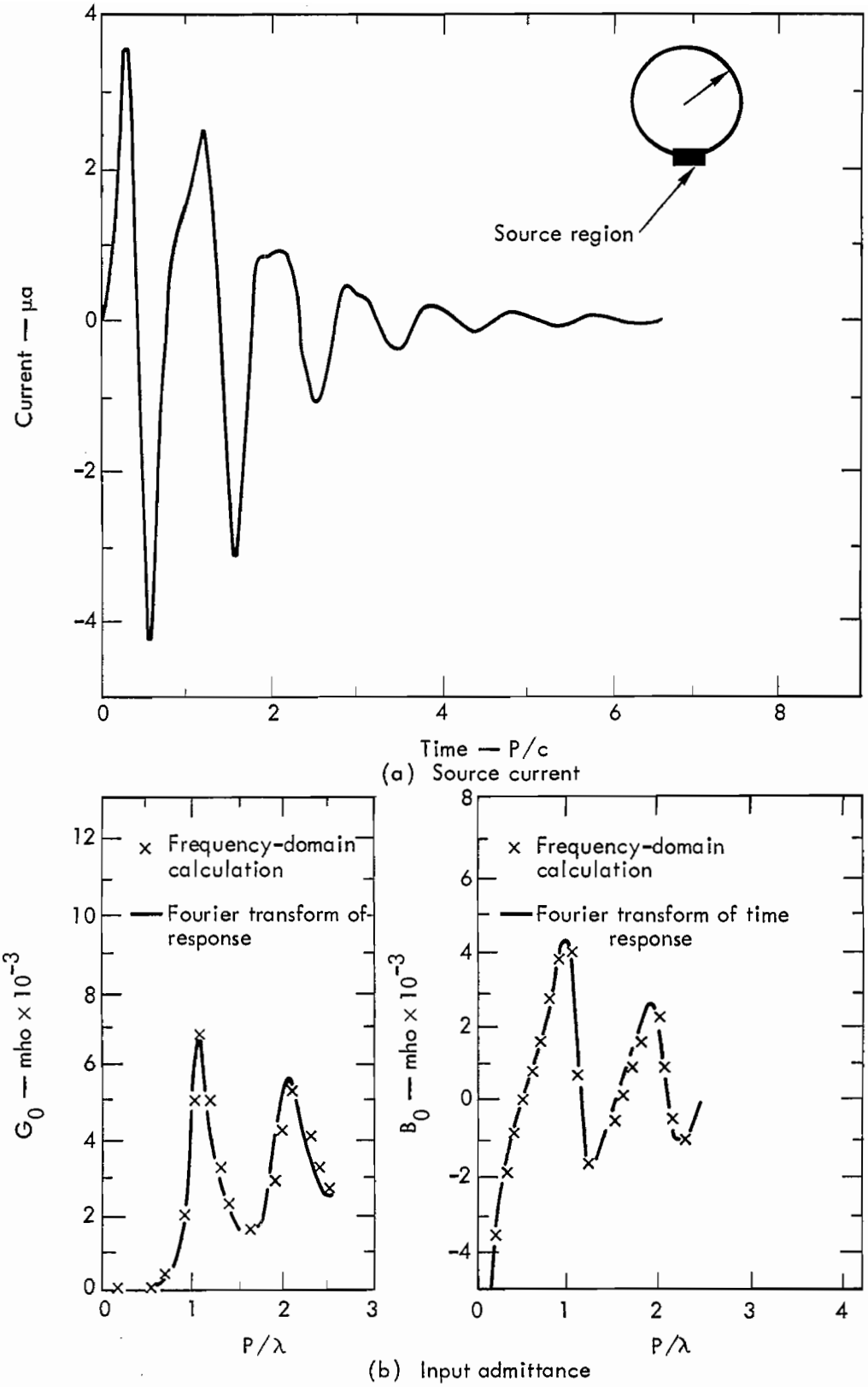

Fig. 55. Loop antenna with time derivative of Gaussian source where the circumference of the loop is 1 m, the source width is P/11, and the number of spatial segments 22. $V_s = 2A^2(t - t_{max})\exp[-A^2(t - t_{max})^2]$ with $A = 1.5 \times 10^9$ and $t_{max} = 1.43 \times 10^{-9}$ sec. Frequency-domain calculations are plotted for comparison (after Poggio, Miller, and Burke[12]).

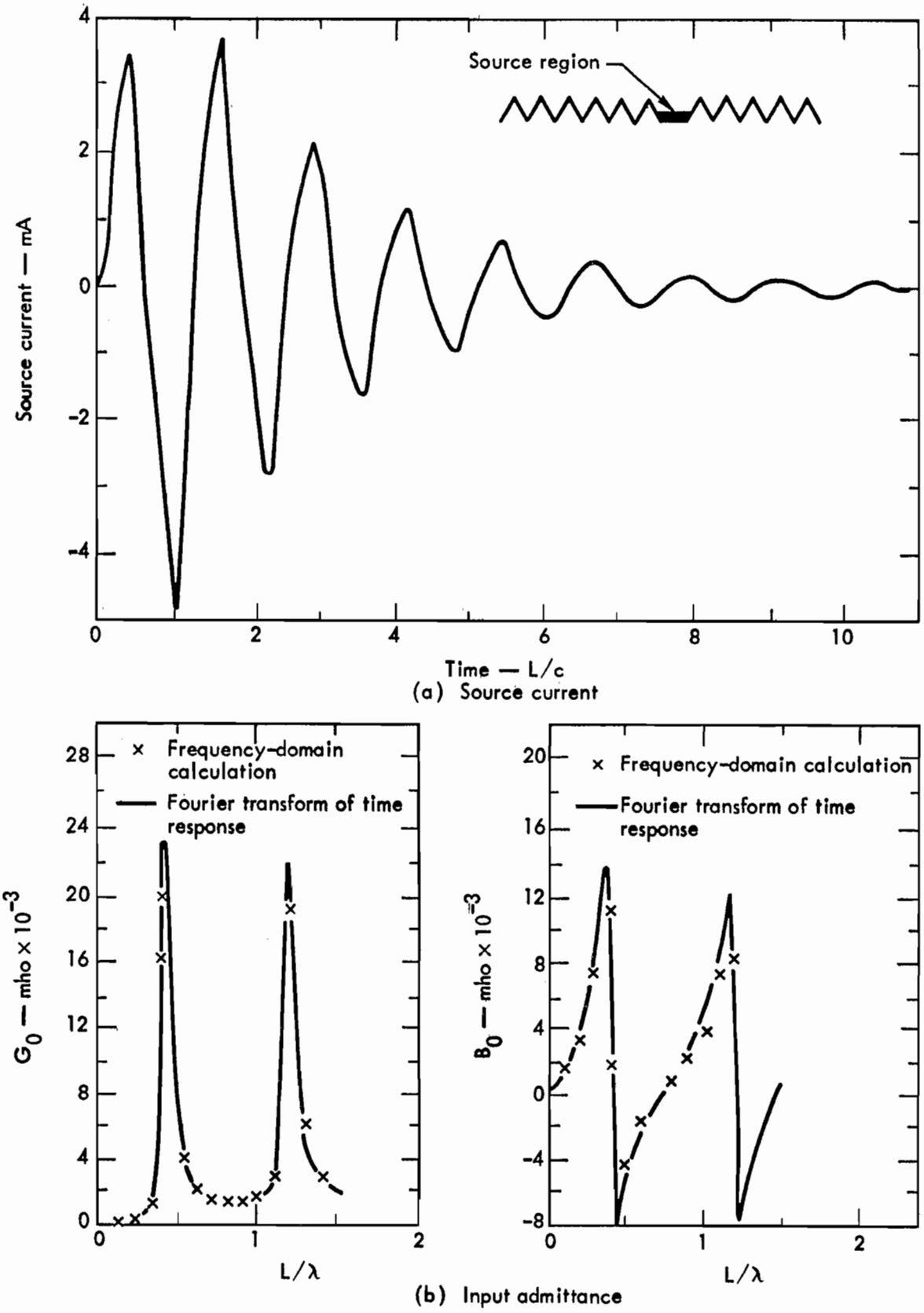

Fig. 56. Zig-zag antenna with Gaussian source time dependence; 22 spatial segments. The total wire length is 1 m and the dipole length 0.5 m. $V_s = \exp[-A^2(t - t_{max})^2]$ with $A = 1.5 \times 10^9$ sec. Frequency-domain calculations are plotted for comparison (after Poggio, Miller, and Burke[12]).

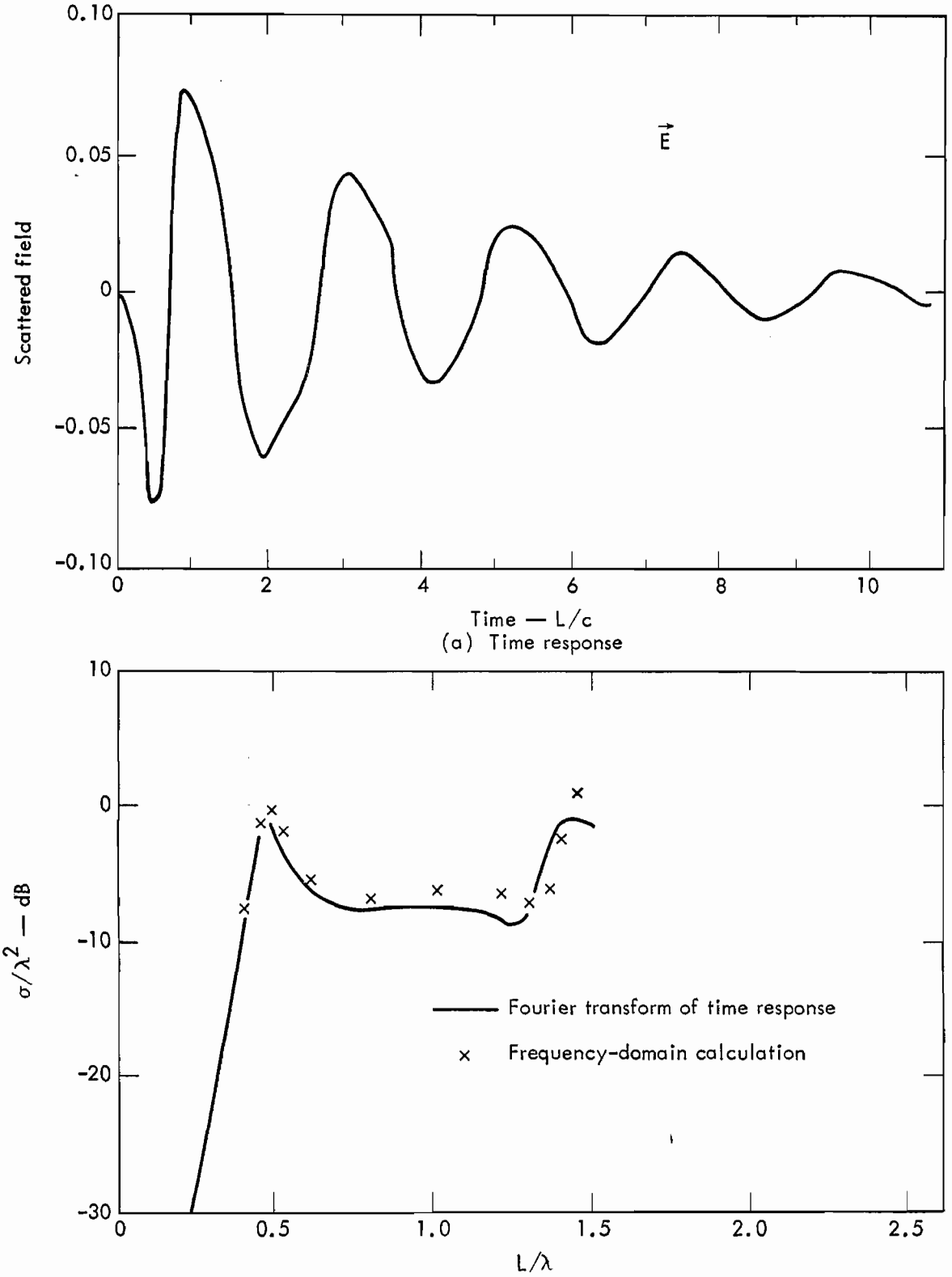

Fig. 57. Scattering of a Gaussian pulse by a dipole where the ratio of wire radius to length is 0.00667, the dipole length is 1 m, and the number of spatial segments 11. $\overline{E}^A = \exp\{-A^2[z/c - (t - t_{max})]^2\}$ with $A = 1.5 \times 10^9$ and $t_{max} = 1.43 \times 10^{-9}$ sec. Frequency-domain calculations are plotted for comparison (after Poggio, Miller, and Burke[12]).

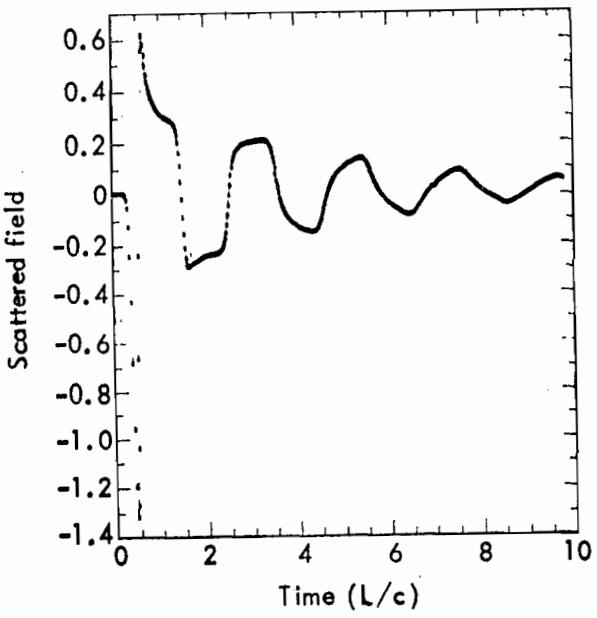

Fig. 58. Time-dependent backscattered field computed from a time-domain solution for a straight wire scatterer for broadside illumination using the wire model and the parameters of Fig. 50.

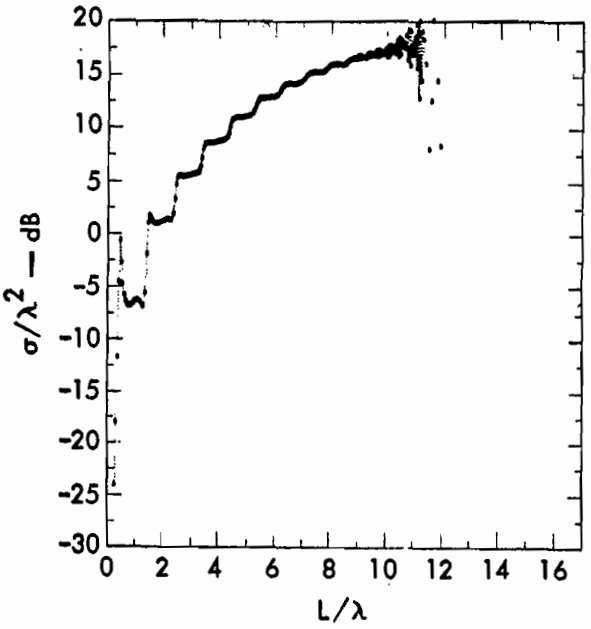

Fig. 59. The backscatter radar cross section, σ/λ^2, obtained from the Fourier transform of results shown in Fig. 58.

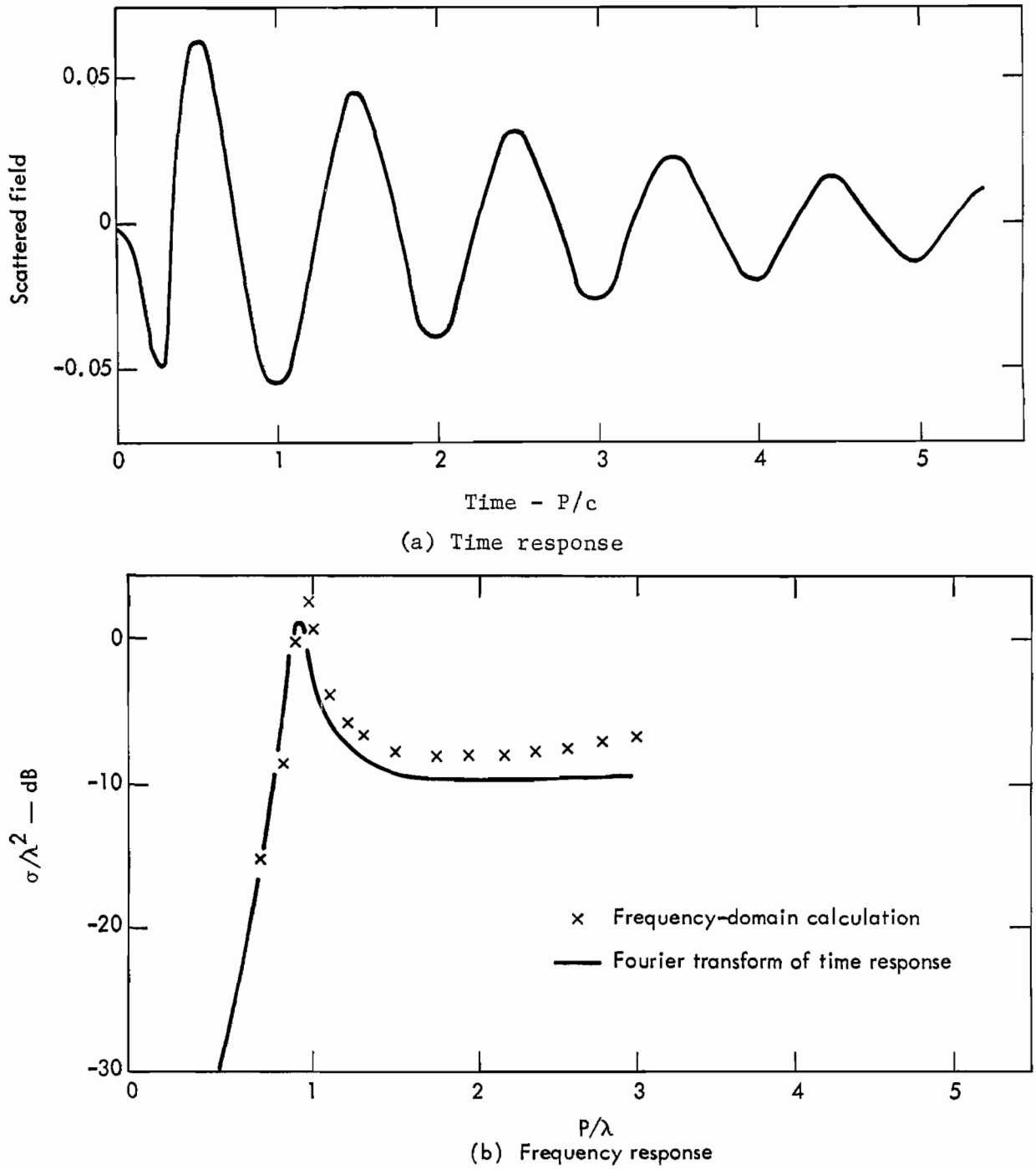

Fig. 60. Scattering of a Gaussian pulse axially incident on a ring whose circumference (P) is 2 m. The ratio of wire radius to ring radius is 10^{-3} and the number of spatial segments 12. In this case, $\Delta t = 3.03 \times 10^{-10}$ sec = $\Delta P/c$, and $\overline{E}^A = \exp\{-A^2[z/c - (t - t_{max})]^2\}$ with $A = 1.5 \times 10^9$ and $t_{max} = 1.43 \times 10^{-9}$ sec. Frequency-domain calculations are plotted for comparison (after Poggio, Miller, and Burke[12]).

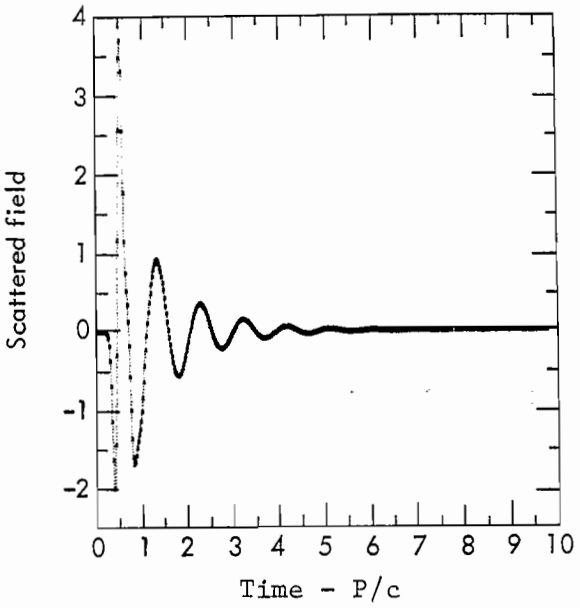

Fig. 61. Time-dependent scattered field of a 48-sided polygon having a wire radius of 0.00674 m, a circumference of 1 m, and A = 3.25 x 10^9 (see Fig. 60 for comparison).

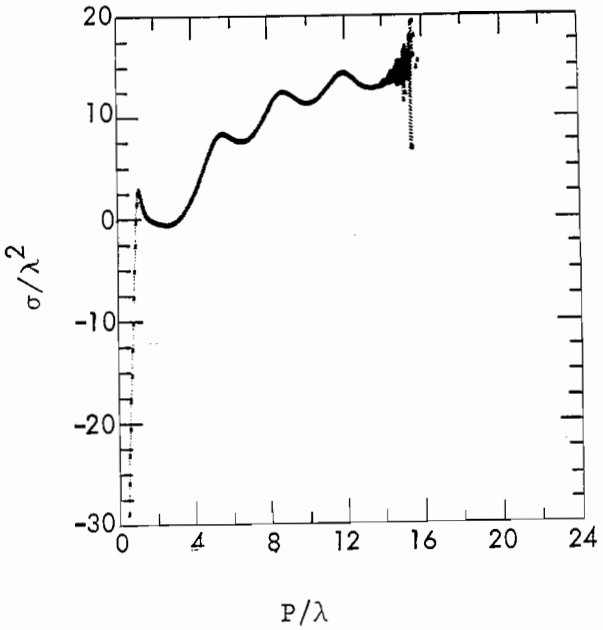

Fig. 62. The backscatter radar cross-section σ/λ^2, obtained from the Fourier transform of the results shown in Fig. 61.

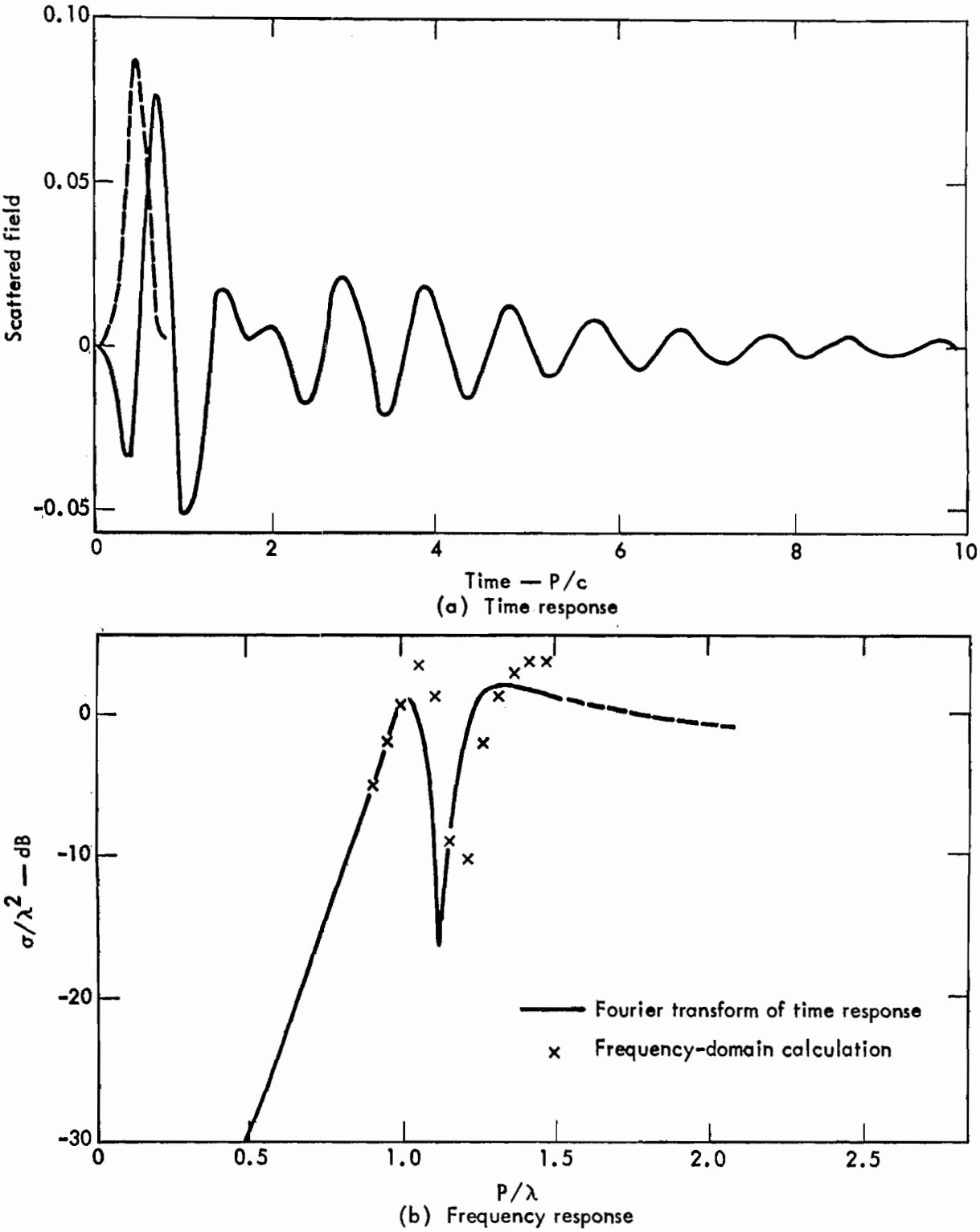

Fig. 63. Scattering of a Gaussian pulse by two concentric rings where the circumference of the large ring (P) is 1 m, the ratio of ring radii is 1.25, the ratio of wire radius to ring radius is 0.03, and the number of spatial segments (each ring) is 12. In this case $\Delta t = 2.777 \times 10^{-10}$ sec, and $\bar{E}A = \exp\{-A^2[z/c - (t - t_{max})]^2\}$ with $A = 1.5 \times 10^9$ and $t_{max} = 1.43 \times 10^{-9}$ sec. Frequency-domain calculations are plotted for comparison (after Poggio, Miller, and Burke[12]).

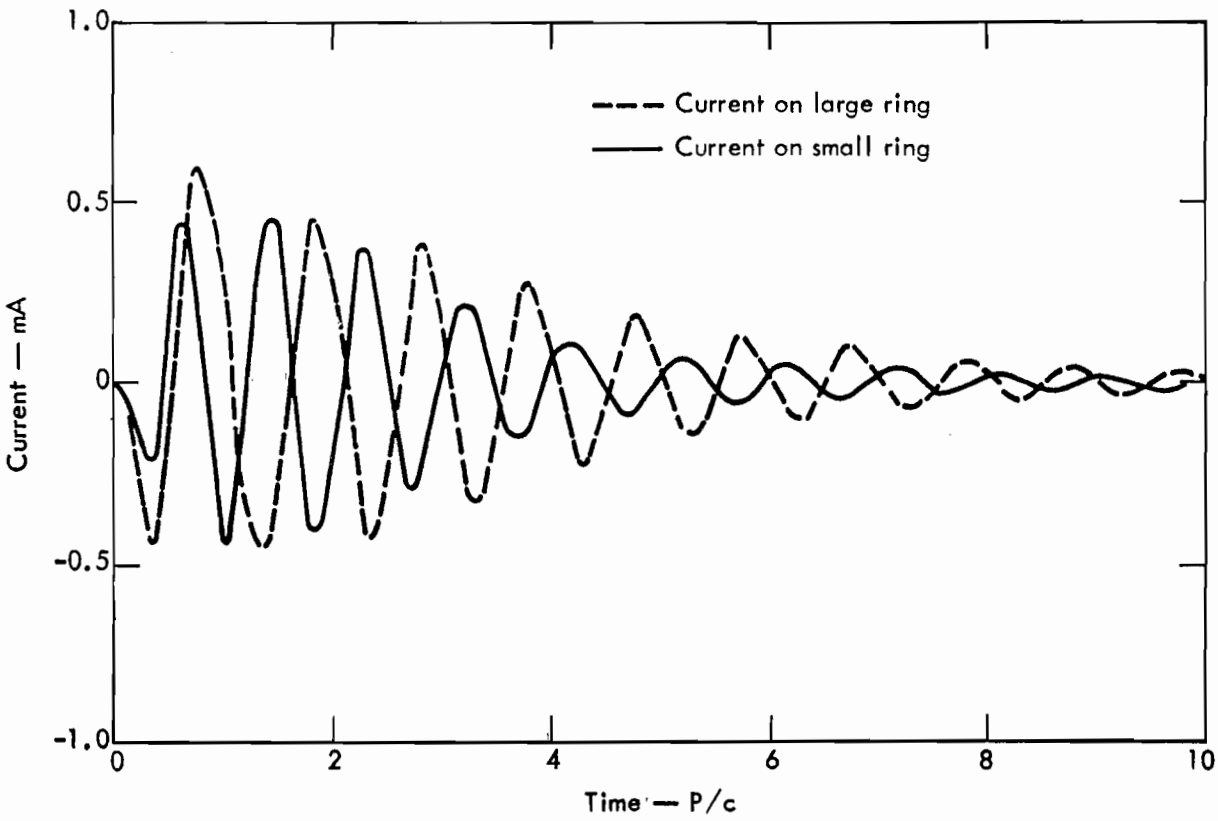

Fig. 64. Current on two concentric rings due to incident Gaussian pulse (after Poggio, Miller, and Burke[12]).

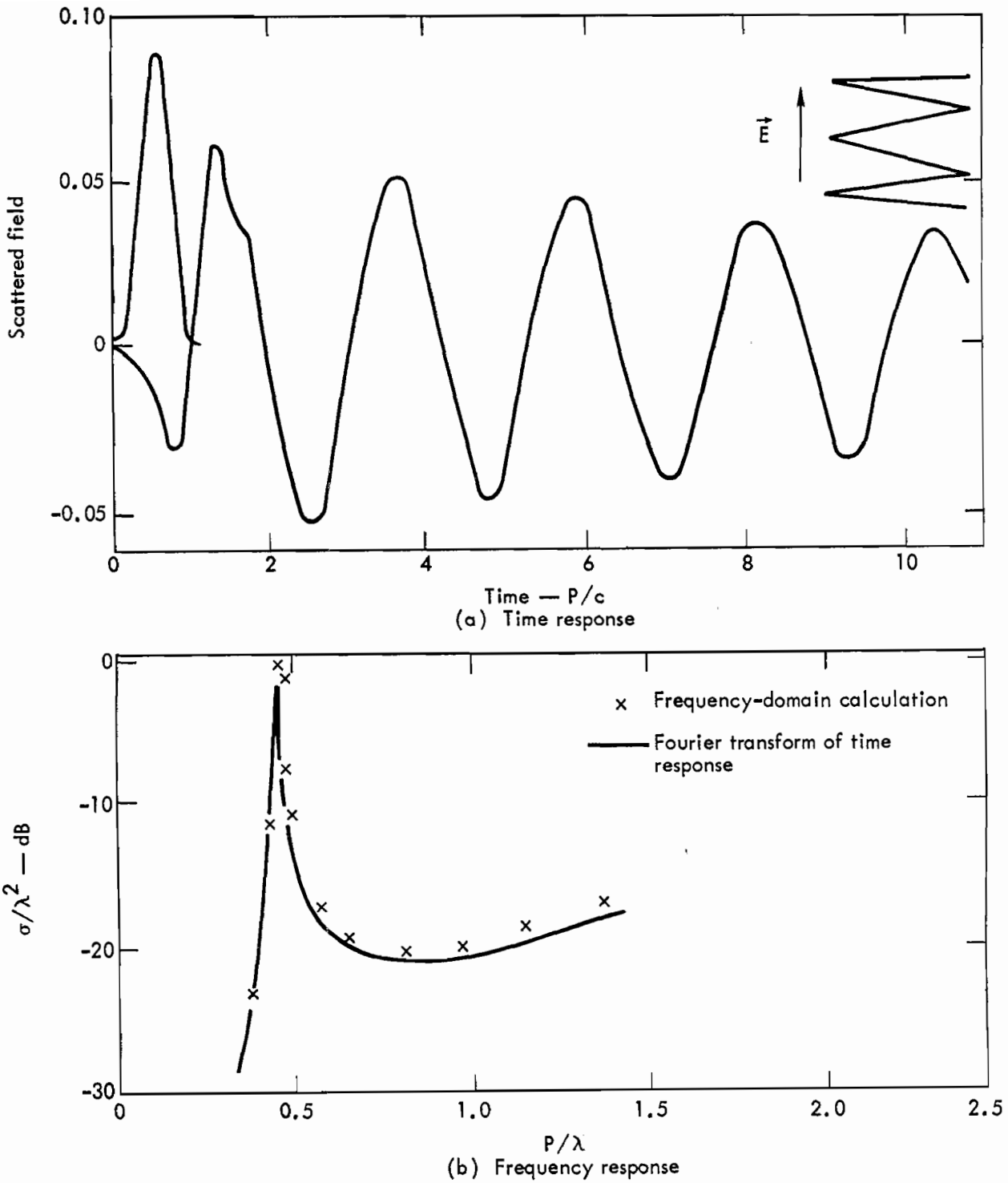

Fig. 65. Scattering of a Gaussian pulse by a six-point crown band 25.13 in. (P) in circumference; 24 spatial segments. The total wire length is 84 in. and wire radius 0.0625 in. Segment length $\Delta z = c\Delta t$. $\bar{E}^A = \exp\{-A^2[z/c - (t - t_{max})]^2\}$ with $A = 2.0 \times 10^9$ and $t_{max} = 1.06 \times 10^{-9}$ sec. Frequency-domain calculations are plotted for comparison (after Poggio, Miller, and Burke[12]).

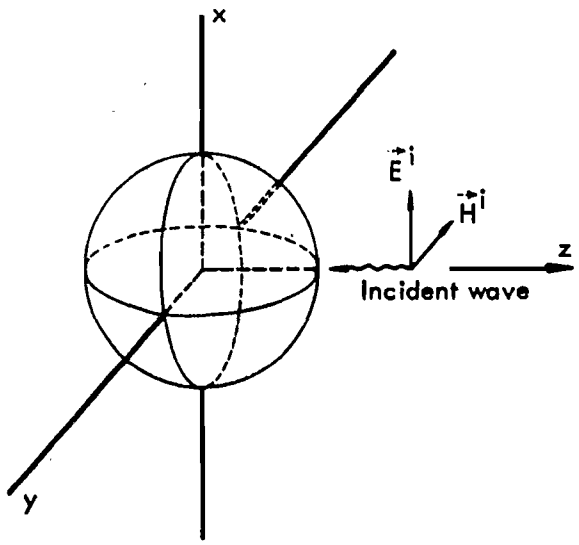

Fig. 66. Small scientific satellite model (length-to diameter ratio of each antenna is 50) (after Bennett, DeLorenzo, and Auckenthaler[10]).

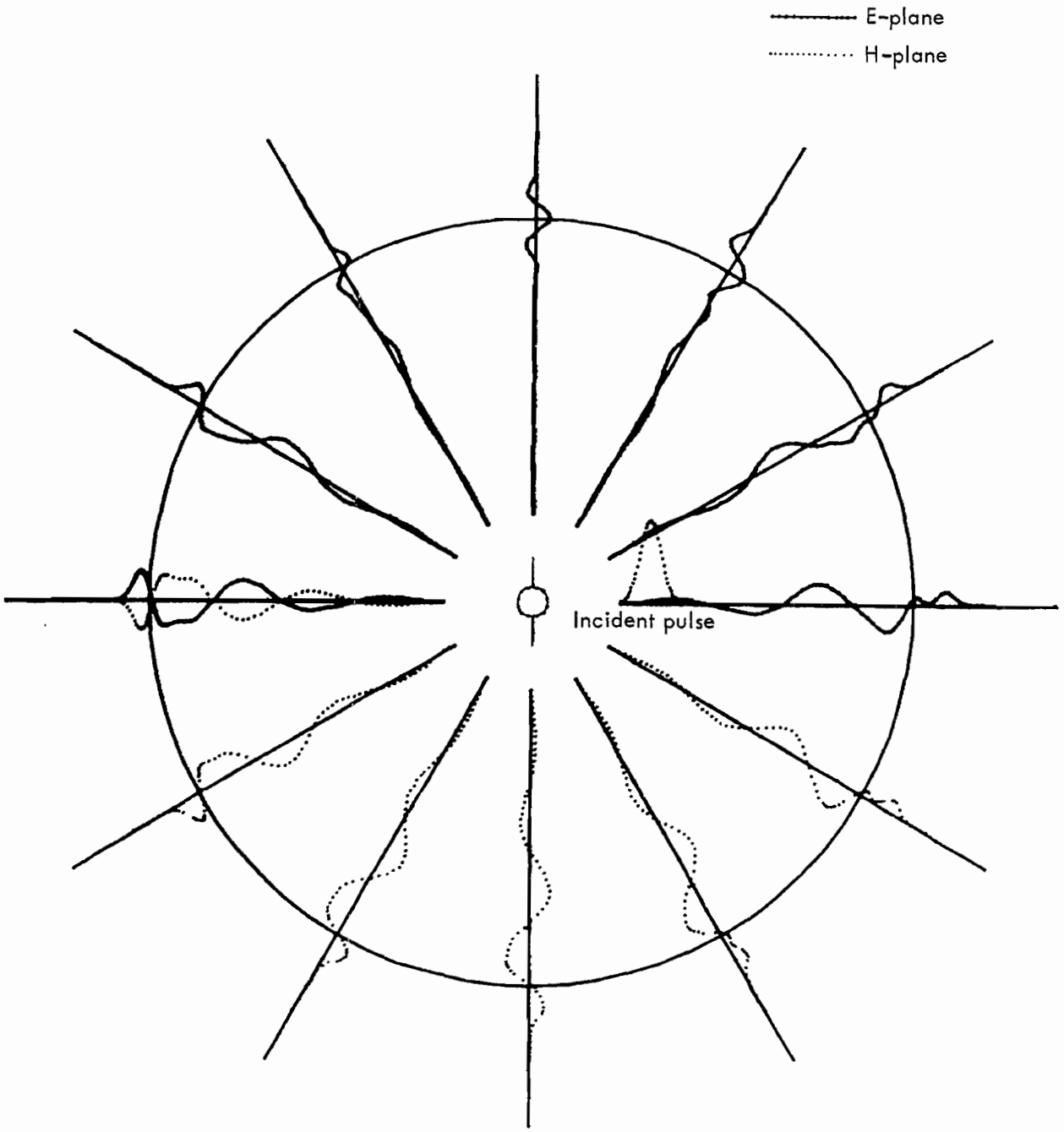

Fig. 67. Smoothed impulse response of SSS satellite model (after Bennett, DeLorenzo, and Auckenthaler[10]).

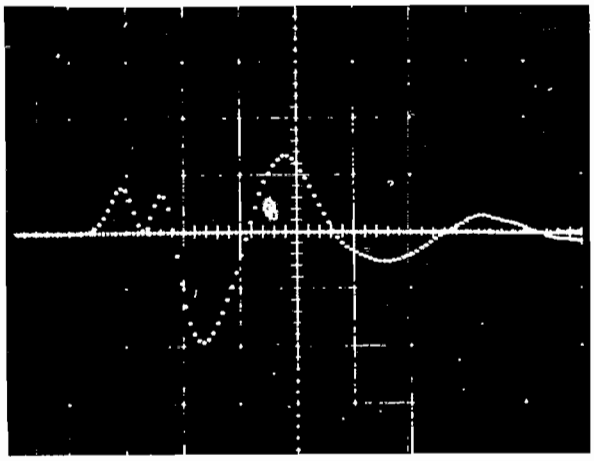

(a) Measured SSS response
(horizontal scale = 0.5 nsec/div)

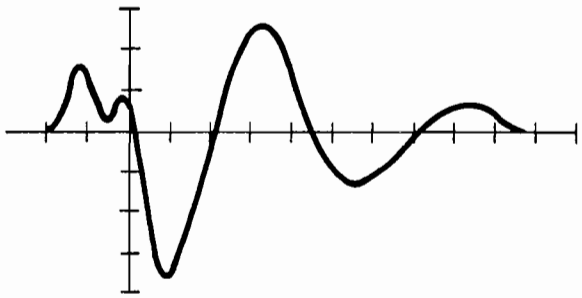

(b) Calculated SSS response

Fig. 68. Comparison of calculated and measured SSS response in backscatter direction (after Bennett, DeLorenzo, and Auckenthaler[10]).

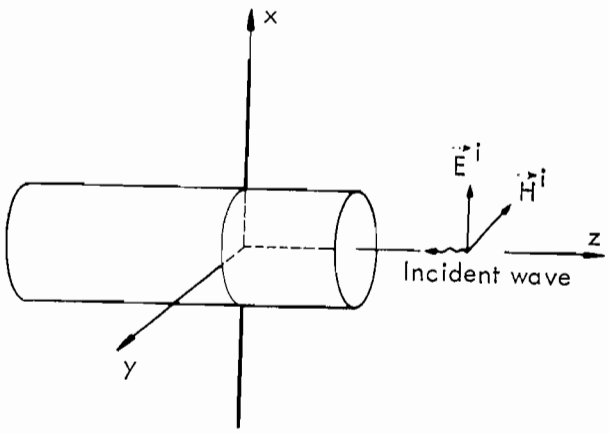

Fig. 69. Early warning reconnaissance satellite model (length-to-diameter ratio of each antenna is 50) (after Bennett, DeLorenzo, and Auckenthaler[10]).

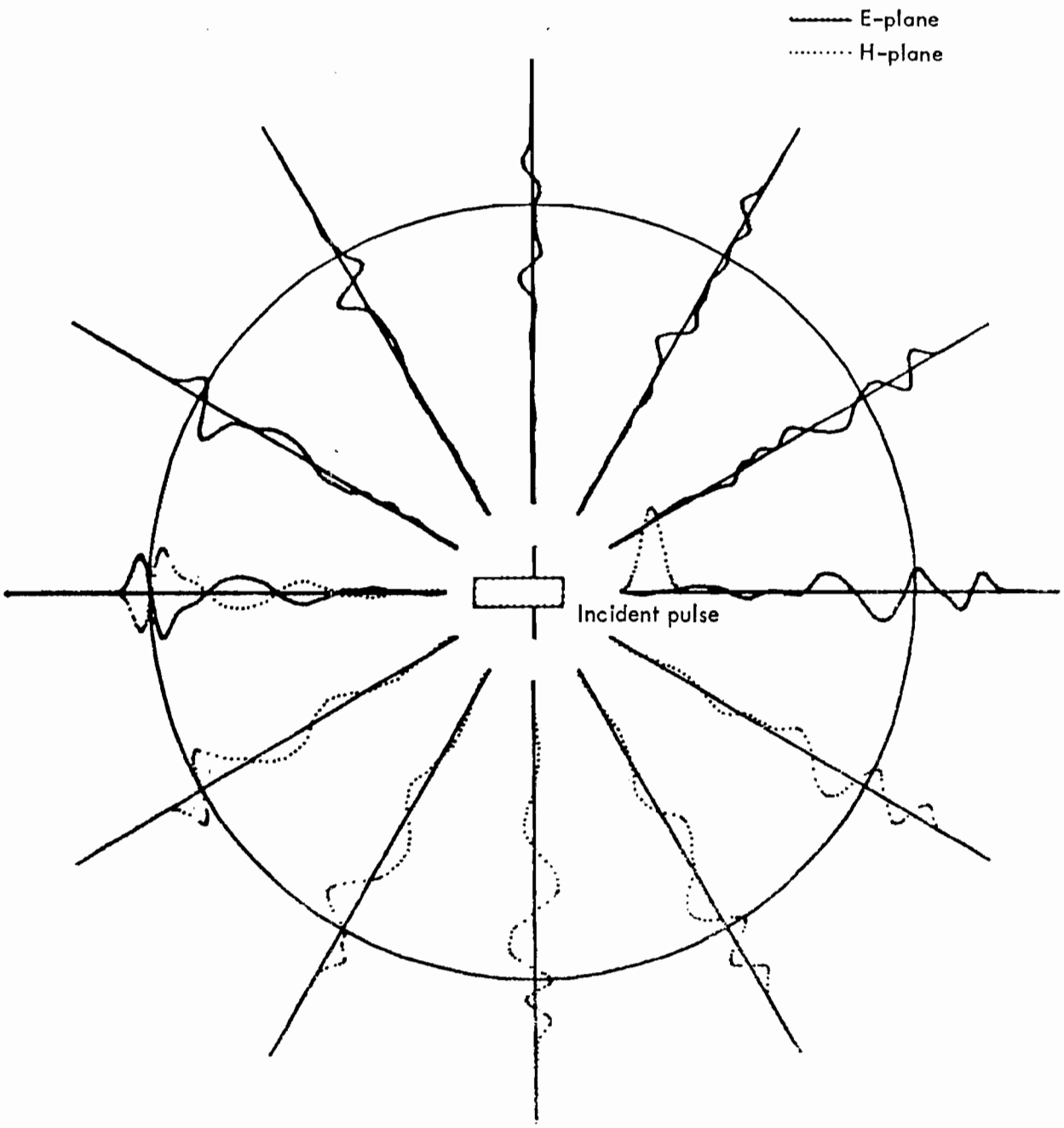

Fig. 70. Smoothed impulse response of EWRS satellite model computed with CSCAT (ater Bennett, DeLorenzo, and Auckenthaler[10]).

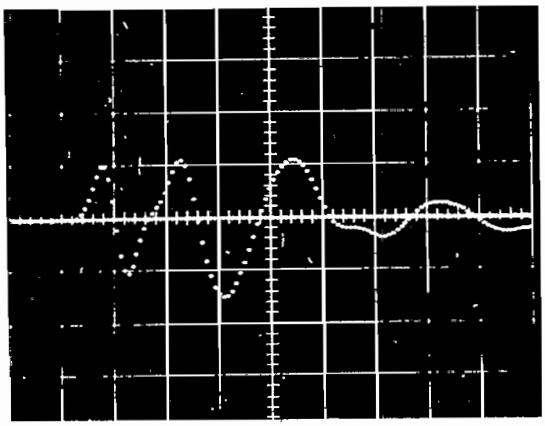

(a) Measured EWRS response
(horizontal scale = 0.5 nsec/div)

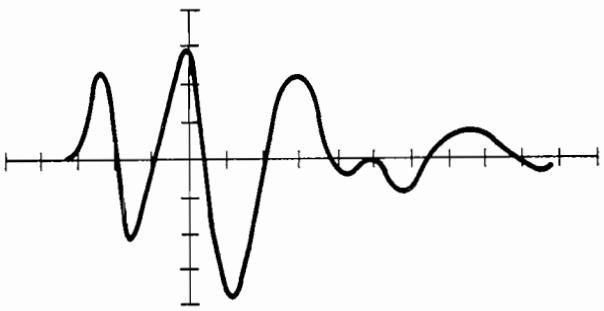

(b) Calculated EWRS response

Fig. 71. Comparison of calculated and measured EWRS response in backscatter direction (after Bennett, DeLorenzo, and Auckenthaler[10]).

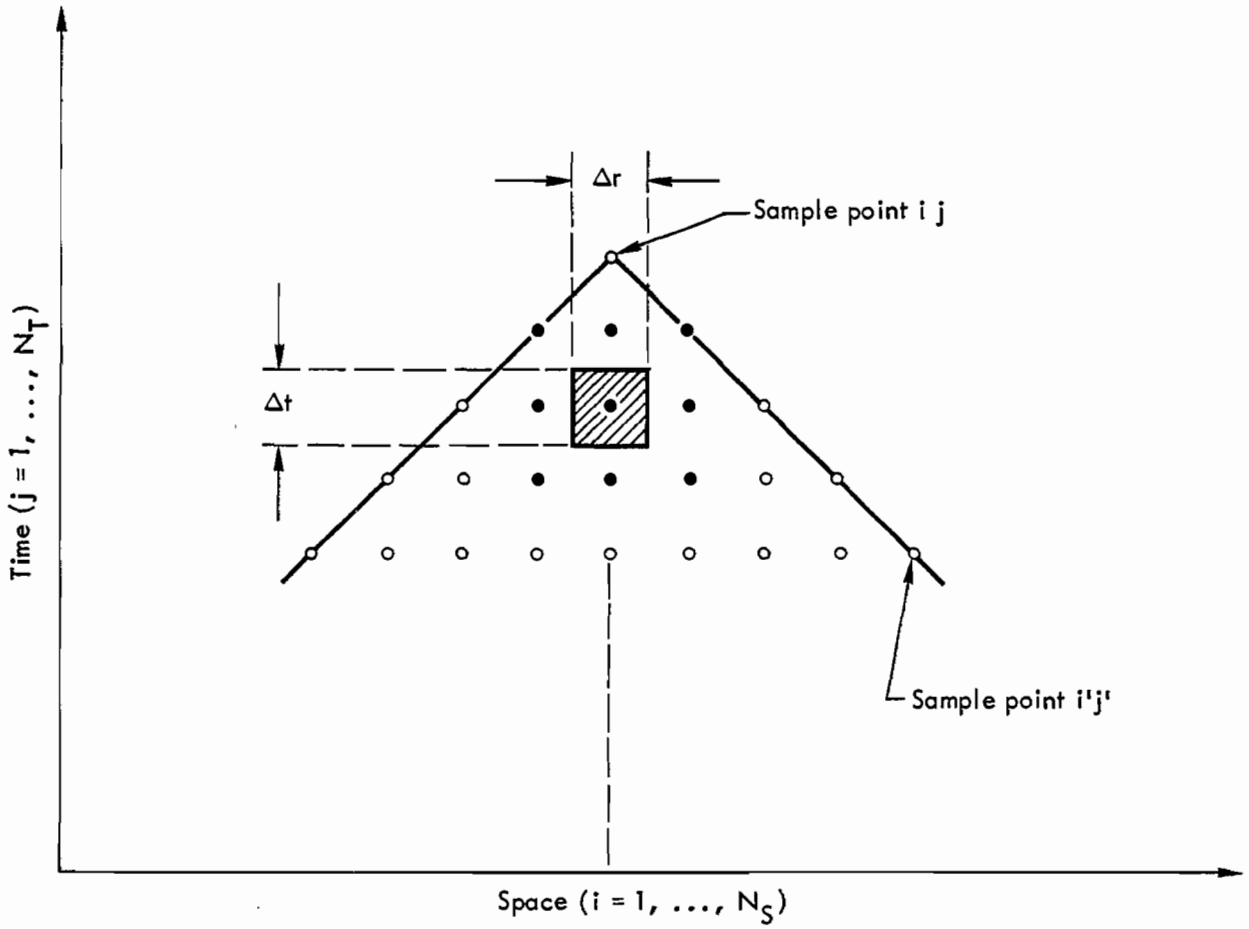

Fig. 72. Time-space sampling relationship.

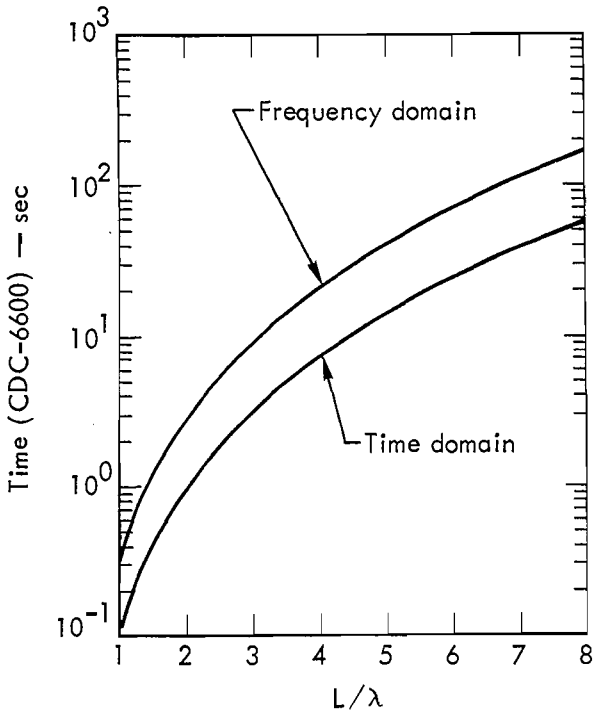

Fig. 73. Computer time requirements for the bistatic (single source) transient analysis of wire structures.

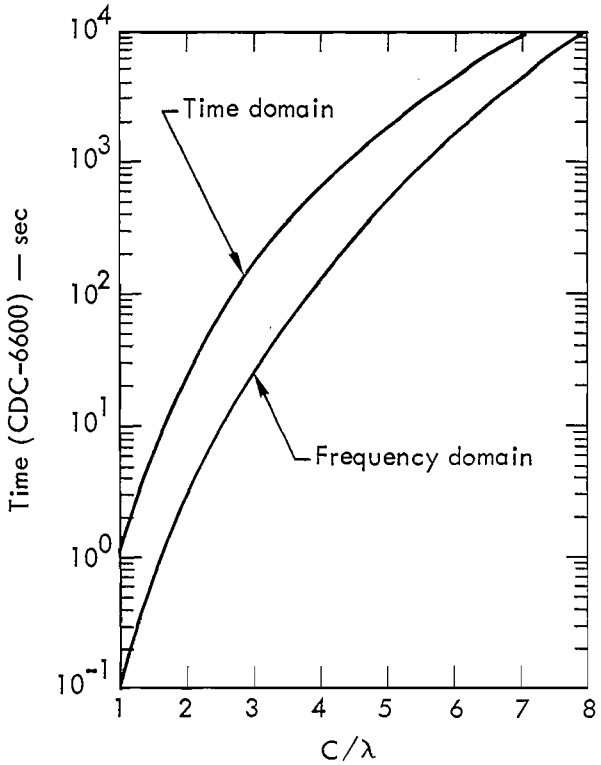

Fig. 74. Computer time requirements for the bistatic (single source) transient analysis of surface structures.

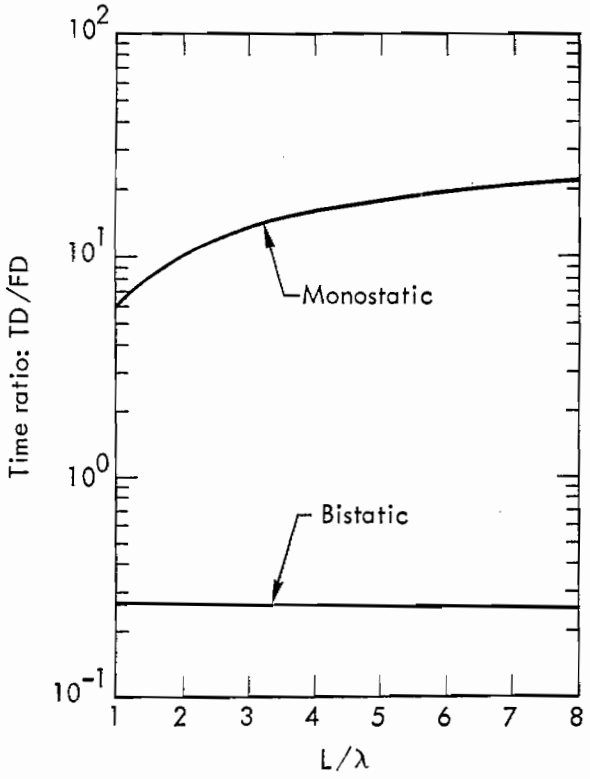

Fig. 75. Ratios of time- to frequency-domain calculation times for the transient response of wires.

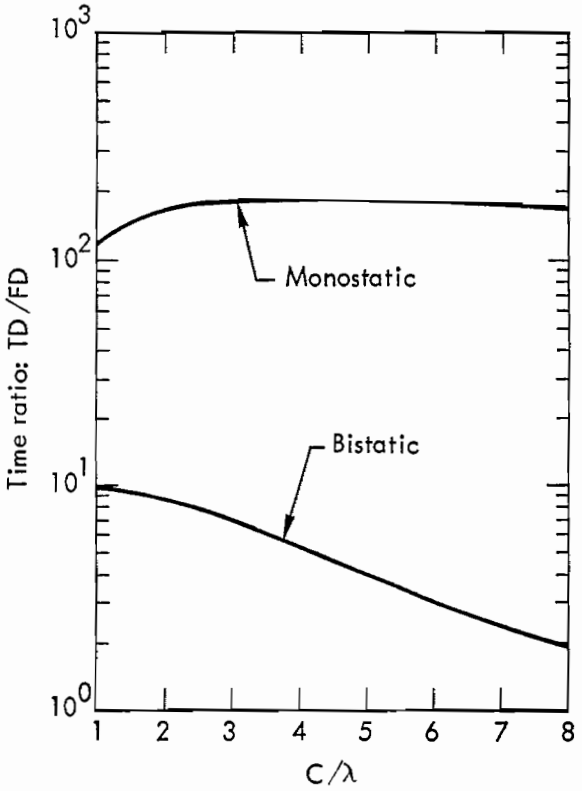

Fig. 76. Ratios of time- to frequency-domain calculation times for the transient response of surfaces.

REFERENCES

1. E. M. Kennaugh and R. L. Cosgriff, "The Use of Impulse Response in Electromagnetic Scattering Problems," in IRE Natl. Conv. Rec. 1958, pt. 1, p. 72.

2. E. M. Kennaugh and D. L. Moffatt, Proc. IEEE 53, 893 (1965).

3. J. Rheinstein, IEEE Trans. Ant. and Prop. AP-16, 89 (1968).

4. M. G. Andreason, IEEE Trans. Ant. and Prop. AP-13, 303 (1965).

5. F. K. Oshiro, "Source Distribution Techniques for the Solution of General Electromagnetic Scattering Problems," in Proc. First GISAT Symposium, Mitre Corp., 1965, vol. I, pt. I.

6. J. H. Richmond, Proc. IEEE 53, 796 (1965).

7. A. J. Poggio and E. K. Miller, "integral Equation Solutions of Three-Dimensional Scattering Problems," in course notes for Numerical Methods in Electromagnetics and Antennas, U. of Illinois, Sept. 1970, R. Mittra, Ed.; to be published by Pergamon Press.

8. C. L. Bennett and W. L. Weeks, "Electromagnetic Pulse Response of Cylindrical Scatterers," G-AP Symposium, Boston, Mass., 1968; also A Technique for Computing Approximate Electromagnetic Impulse Response of Conducting Bodies, Purdue University, W. Lafayette, Indiana, Rept. TR-EE68-11 (1968).

9. E. P. Sayre and R. F. Harrington, "Transient Response of Straight Wire Scatterers and Antennas," in Proc. 1968 Intl. Ant. Prop. Symposium, Boston, Mass., 1968, p. 160.

10. C. L. Bennett, J. D. De Lorenzo, and A. M. Auchenthaler, Integral Equation Approach to Wideband Inverse Sacttering, Rome Air Development Center, Rome, N. Y. Rept. RADC-TR-70-177, vol. I (1970).

11. E. K. Miller, A. J. Poggio, and G. J. Burke, An Integro-Differential Equation Technique for the Time-Domain Analysis of Thin Wire Structures; Part I, The Numerical Method, Lawrence Livermore Laboratory, Rept. UCRL-73346 (1971); to appear in J. Computat. Phys.

12. A. J. Poggio, E. K. Miller, and G. J. Burke, An Integro-Differential Equation Technique for the Time-Domain Analysis of Thin Wire Structures; Part II, The Numerical Results, Lawrence Livermore Laboratory, Rept. UCRL-73346 (1972); to appear in J. Computat. Phys.

13. D. E. Merewether, IEEE-Trans. Electromagnetic Compatibility EMC-13, No. 2, 41 (1971).

14. G. W. Bechtold and D. J. Kozakoff, IEEE-Trans. Electromagnetic Compatibility EMC-12, No. 1, 5 (1970).

15. G. W. Bechtold and D. J. Kozakoff, IEEE-Trans. Electromagnetic Compatibility EMC-12, No. 1, 9 (1970).

16. C. W. Harrison and R. W. P. King, IEEE-Trans. Ant. and Prop. AP-15, No. 2, 301 (1967).

17. J. F. A. Ormsby and M. R. Weiss, Canad. J. Physics 49, 1929 (1971).

18. W. H. Haynes and C. L. Wilkerson, IEEE-Trans. Electromagnetic Compatibility EMC-12, No. 3, 112 (1970).

19. D. C. Chang and C. W. Harrison, IEEE-Trans. Electromagnetic Compatibility EMC-13, No. 1, 14 (1971).

20. D. B. Hodge, IEEE-Trans. Ant. and Prop. AP-19, No. 4, 558 (1971).

21. C. P. Bates and G. T. Hawley, IEEE-Trans. Electromagnetic Compatibility EMC-13, No. 4, 18 (1971).

22. A. J. Poggio, IEEE-Trans. Ant. and Prop. AP-19, No. 5, 702 (1971).

23. J. A. Stratton, Electromagnetic Theory (McGraw-Hill, New York, 1941).

24. W. K. H. Panofsky and M. Phillips, Classical Electricity and Magnetism (Addison-Wesley Inc., Reading, Mass., 1956).

25. O. D. Kellog, Foundations of Potential Theory (Dover Publications, New York, 1953).

26. S. H. Lin and K. K. Mei, IEEE-Trans. Ant. and Prop. AP-16, No. 2, 235 (1968).

27. R. F. Harrington and J. R. Mautz, Radiation and Scattering from Bodies of Revolution, Syracuse University, Contract No. F-19628-67-C-0233 (1969).

28. C. L. Bennett and W. L. Weeks, IEEE-Trans. Antenna Propagation AP-18, No. 5, 627 (1970).

29. M. J. Gans, Proc. IEEE 53, 1081 (1965).

30. A. R. Neureuther, G. J. Burke, E. K. Miller, and G. M. Pjerrou, IEEE-Trans. Ant. and Prop. AP-19, No. 6, 789 (1971).

31. A. M. Nicolson, C. L. Bennett, D. Lamensdorf, and L. Susman, IEEE-Trans. Micro. Theory and Techniques MTT-20, No. 1, 3 (1972).

32. R. W. P. King, The Theory of Linear Antennas (Harvard University Press, Cambridge, Mass., 1956).

33. E. K. Miller, G. J. Burke, and E. S. Seldon, IEEE-Trans. Ant. and Prop. AP-19, No. 4, 534 (1971).

34. R. F. Harrington, Field Computations by Moment Methods (MacMillan, New York, 1968).

35. S. Gee, E. K. Miller, A. J. Poggio, E. S. Seldon, and G. J. Burke, "Computer Techniques for Electromagnetic Scattering and Radiation Analysis," presented at the Electromagnetic Compatibility Meeting, Philadelphia, 1971.

36. H. H. Chao and B. J. Strait, IEEE-Trans. Ant. and Prop. AP-19, No. 5, 701 (1971).

37. E. K. Miller and A. Olte, Radio Science 1, 1425 (1966).

38. E. K. Miller, J. Computational Phys. 5, 265 (1970).

39. L. Susman and D. Lamensdorf, Picosecond Pulse Antenna Techniques, Rome Air Development Center, Rome, N. Y., Rept. RADC-TR-71-64 (1971).

40. W. E. Blore, IEEE-Trans. Ant. and Prop. AP-12, 582 (1964).

41. D. L. Moffatt, Low Radar Cross Sections--The Cone Sphere, Ohio State University, Columbus, Ohio, Rept. 1223 (1962).